CHARACTERIZATION OF LIGHT WEIGHT COMPOSITE PROPPANTS

A Thesis

by

MANDAR CHAITANYA KULKARNI

Submitted to the Office of Graduate Studies of
Texas A&M University
in partial fulfillment of the requirements for the degree of

MASTER OF SCIENCE

December 2008

Major Subject: Mechanical Engineering

CHARACTERIZATION OF LIGHT WEIGHT COMPOSITE PROPPANTS

A Thesis

by

MANDAR CHAITANYA KULKARNI

Submitted to the Office of Graduate Studies of
Texas A&M University
in partial fulfillment of the requirements for the degree of

MASTER OF SCIENCE

Approved by:

Chair of Committee,	Ozden Ochoa
Committee Members,	Anastasia Muliana
	Ramesh Talreja
Head of Department,	Dennis O'Neal

December 2008

Major Subject: Mechanical Enigneering

ABSTRACT

Characterization of Light Weight Composite Proppants. (December 2008)
Mandar Chaitanya Kulkarni, B.E., Sardar Patel University, India
Chair of Advisory committee: Dr. Ozden Ochoa

The research objectives are to develop experimental and computational techniques to characterize and to study the influence of polymer coating on the mechanical response of walnut shell particles to be used as proppants.

E3-ESEM and Zeiss Axiophot LM are used to study the cellular microstructure and feasibility of polymer infiltration and uniform coating. Three main testing procedures; single particle compression, heating tests on coated and uncoated walnut shell particles and 3-point flexure tests are undertaken. In in-situ ESEM observations on both the coated and uncoated particles showed signs of charring at about 175 – 200 ºC. Single particle compression test are conducted with random geometry particles and subsequently with four distinct shape categories to minimize the statistical scatter; flat top, round top, cone top, and high aspect ratio. Single particle tests on uniformly cut cuboid particles from walnut shell flakes are used to capture the nonlinear material response. Furthermore cyclic compression loads are imposed on flat top particles which reveal that significant permanent deformation set in even at low load levels.

Computational models include Hertzian representation, 2D and 3D finite element models to simulate single coated and uncoated particles under compression. The elastic material with geometric nonlinear representation is not able to simulate the compression response observed during testing. The inelastic material representation is able to significantly improve the compression response and address the influence of geometric shape on particle response. A single uniform layer of polymer coat is introduced on the 3D models with nonlinear material definition. Coating provides a marginal improvement in load vs displacement response of the particles while increasing the ability of the particle to withstand higher loads.

ACKNOWLEDGMENTS

First of all I would like to thank Dr. Ozden Ochoa for giving me an opportunity to work on this project. It has been a privilege to work under her guidance. She has always been there to guide me with the research and has been very patient in her explanations and discussions. Working with her has been a great learning experience and she has continuously inspired and motivated me to work towards my academic goals.

I would also like to thank Dr. Ramesh Talreja and Dr.Anastasia Muliana for serving on my committee and providing me with valuable comments on my work.

I am also thankful to Rick Littleton and E. Ann Ellis at the Microscopy and Imaging centre, Texas A&M University for their valuable guidance and help in working on the microstructure and imaging aspect of the project.

I would also take this opportunity to thank my lab mates, Melanie, Douglas, Min and Nori, for being a constant source of inspiration and help, especially Melanie and Douglas for their help and guidance during my first few months as a graduate student.

I cannot forget my friends, Nikhil and Sneha, who have been constant companions and I don't have enough words to describe their influence on my research.

I dedicate this work to my parents who have ensured that I reach this position. Their encouragement and support right through my academic career has enabled me to reach where I am. I bow to them with all the respect and dedicate this work to them.

I also gratefully appreciate the research guidance and financial support provided by BJ Services Inc., Tomball, TX through the TEES project # 32525 – 38900.

TABLE OF CONTENTS

Page

Page

LIST OF FIGURES

FIGURE Page

FIGURE Page

FIGURE Page

FIGURE Page

FIGURE Page

FIGURE Page

LIST OF TABLES

TABLE Page

1 INTRODUCTION

1.1 Overview

Proppants are small particles which are mixed with the fracturing fluid in the hydraulic fracturing treatments during oil well drilling. Hydraulic fracturing is a process where a highly pressurized fluid is pumped in a well at a sufficiently high rate to create fractures. These fractures provide high conductive flow paths for oil and orient radially away from the well bores (Figure 1) [1]. Proppants are delivered to these fractures to ensure that the flow paths remain open while resisting the rock pressure. The proppants settle in the rock fissures either as a closed pack arrangement or as a single layer and prop the fissures open while ensuring sufficient permeability to enable continued oil production. A schematic of proppant supporting a fracture is shown in Figure 2 [2].

Historically sand is the most commonly used proppant material. However as the well depth increases, the stresses exerted by the rock faces, known as closure stresses increase and crush the sand particles generating free fines (fragmented pieces of sand particles) which reduce permeability. Resin coated sand and ceramic particles are capable of withstanding high closure stresses up to 20000 psi, but their high density hinders the proppant transport and placement. On the other hand light weight proppants remove this constraint [3]. Two recently proposed light weight materials are hollow ceramic particles and resin coated and infiltrated walnut shell particles.

Walnut shell is widely used in the industry as an abrasive due to its high toughness and elastic modulus and its ability to clean surfaces of metals, alloys or plastics without leaving scratches [4]. Its other uses include as a means for extracting active carbon through chemical activation [5] this extracted carbon obtained through carbonization can be used as a carbon molecular sieve for air separation [6].

This thesis follows the style and format of *Journal of Composite Materials*.

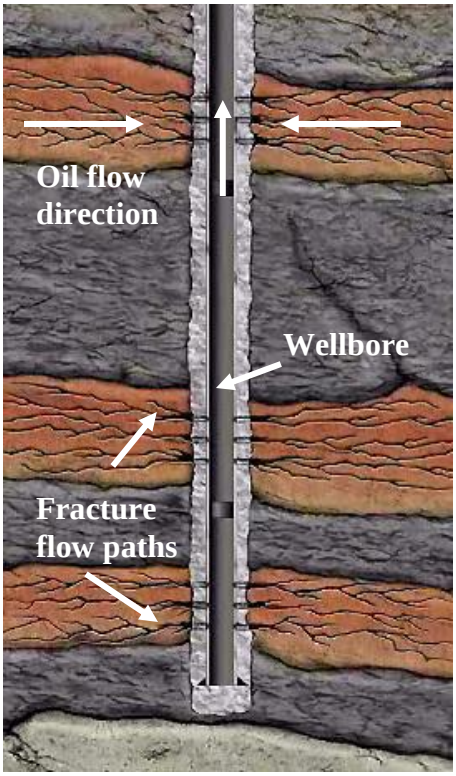

Figure 1. Schematic of a hydraulic fracture showing the fracture flow paths radially oriented away from the wellbore [1]

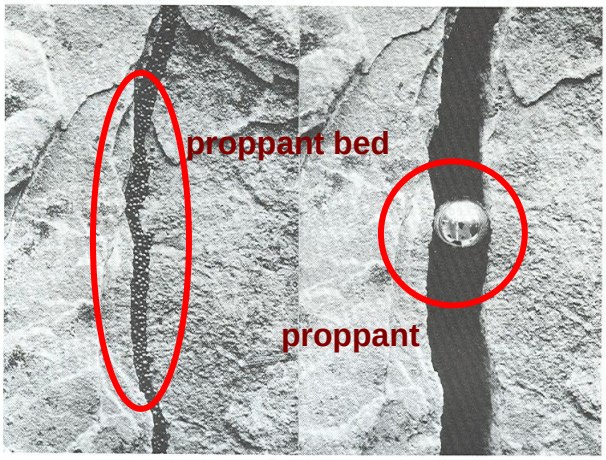

Figure 2. Spherical proppants supporting an open hydraulically induced fracture [2]

Use of uncoated walnut shells as proppants have yielded failure in the past but the newly developed resin coated and infiltrated walnut shell particles have been reported to resist increased closure stresses [3].

In this study experimental and computational techniques are employed to characterize the mechanical response of the *resin coated walnut shell proppants*. Figure 3a shows the larger flakes from which the walnut shell proppants shown in Figure 3b are obtained by grinding and later coating with polymer. Microscopy techniques are used to study the microstructure (Figure 4) and estimate the degree of polymer deposition and infiltration into the particles. Single particle compression tests under an optical microscope are carried out and subsequently FEA models are developed to numerically simulate these compression tests enabling virtual parametric test bed capability.

(a) (b)

Figure 3. (a)Image of walnut shell flakes and (b) Image of coated walnut shell proppants

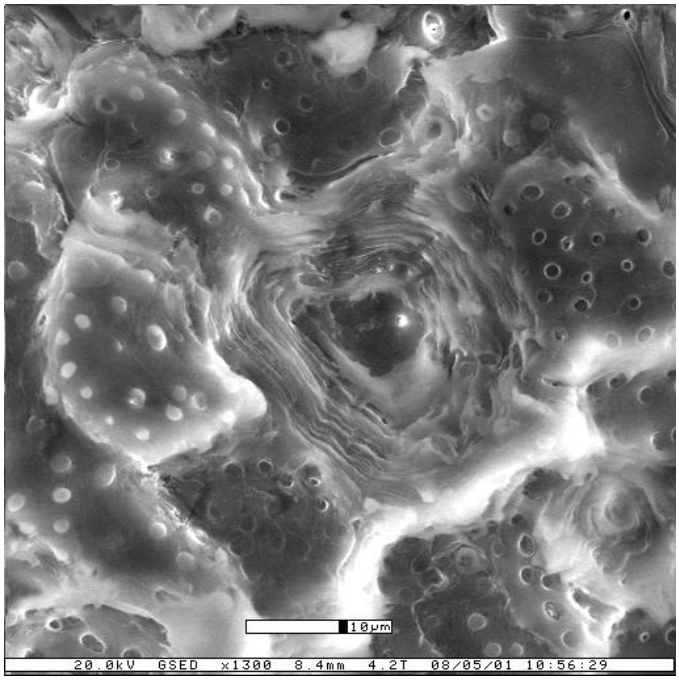

Figure 4. Microstructure of a walnut shell

1.2 Literature Review

As stated by Mader [2], the "purpose of proppants is to support the hydraulic fractures and keep them open against the application of closure stresses to ensure conduction of oil and gas to the borehole". An extensive list of proppant types, significance of material choices, and the effect of shape and size on fracture conductivity are also discussed. It is also noted that sand at greater depths fractures and generates fines, inhibiting the flow. Sinclair presented results [7] according to which resin coated sands sustained closure stresses at a depth 16000 ft. The advantages of a coating are reported as crush resistance, flow back prevention, embedment minimization and reduction in the formation of free fines. Cutler and Swanson [8] studied the crush

resistance of ceramic proppants, and concluded that they provided sufficient crush resistance even at closure stresses of 20,000 psi (140 MPa).

A full proppant monolayer is created when a propped fracture has a width equal to one particle diameter without any space for additional particles. Darin and Huitt [9] theoretically demonstrated that a higher conductivity can be achieved with a proppant concentration below that of a full monolayer. A partial monolayer fracture utilizes less proppants since it allows vacant areas in between particles leading to increase in conductivity. However initial efforts to attain partial monolayer in the field resulted in failure. Veatch [10] stated that in vertical fractures, proppants tend to fall to lower parts of the fracture and hence creating a partial monolayer may be extremely difficult. Brannon et al [11] showed that when ultra light weight (ULW) proppants were placed as a partial monolayer in propped fractures an order of magnitude increase in production was realized in comparison with similarly sized sand particles at the same concentration. Resin coated and infiltrated ground walnut shells and hollow ceramic spheres were two examples of ULW proppants.

Rickards et al [3] reported that the specific gravity for walnut shells at 1.25 is the lowest when compared to Ottawa sand (2.65) and Bauxite (3.65). The lower density directly affects the settling velocity which is (4.3 ft/min) for coated walnut shell proppants against 16.6 ft/min for Ottawa sand and 23.2 ft/min for Bauxite. The lower specific gravity and low settling velocities result in near neutral buoyancy during proppant transport and provide high propped fracture volume and higher fracture conductivity as well as significant increase in resistance to closure stresses.

The classical relationships of cellular solids are presented by Gibson and Ashby [12]. In their approach the effective modulus of wood along axial, radial and tangential directions is a function of the density ratio of wood to the cell wall and the modulus of the cell wall, which is furthermore dependent on the modulus of its constituents as well as the fraction of each individual constituent. Demirbas [13] estimated the structural composition of wood and non-wood biomass samples and reported that the composition of walnut shells are 22.20 wt% Hemicellulose, 25.50 wt% of Cellulose and 52.30 wt%

of Lignin. Bodig and Jane [14] describe in detail the different layers of a wood cell wall and their properties. Bergander and Salmen [15] calculated the cell wall properties based on the properties and orientation of cellulose fibers by using two analytical models noting that along the axial direction properties are dependent on cellulose orientation from 0º to 50º. Huang et al [16] reported similar variation in properties and developed a method to obtain the wood properties based on acoustics. W. Gindl et al [17] determined the cellulose microfibril angle by small-angle X-ray scattering (SAXS) and used nanoindentation to understand the effect of microfibril orientation on the effective property of the spruce wood cell walls. They reported an elastic modulus of 17.1 GPa at 0º orientation compared to the values of 80 GPa calculated by Bergander and Salmen in [15], this was attributed to the fact that the nanoindentation elastic modulus for an anisotropic body is a mixture of moduli along all axes leading to a prediction of lower modulus. The degree of anisotropy and angle enclosed between the faces of the nanoindenter and the load direction significantly impacts the results.

C.H.Wang in [18, 19] carried out C ring compression tests to estimate the elastic modulus of Macadamia nut, hazel nut, walnut and coconut shells. He reported the elastic modulus of walnut shells as 4.9 GPa. Kulkarni et al [20] assessed the mechanical properties of pecan shells using the ring compression tests and estimated the elastic modulus to be 3.7 GPa. The simulations carried out supported the assumption of pecan shells to be isotropic. Esau [21] described the cells of nutshells as sclereids which are relatively short and isodiametric. Their secondary walls vary in thickness and are lignified. The lumina are almost filled with wall deposits and secondary cell wall shows pits. An example of a sclereid cell from podocarpus leaf is shown in Figure 5 [22]. The secondary wall appears concentrically lamellated in ordinary and polarized light which may be due to an alternation of isotropic layers with those composed of cellulose.

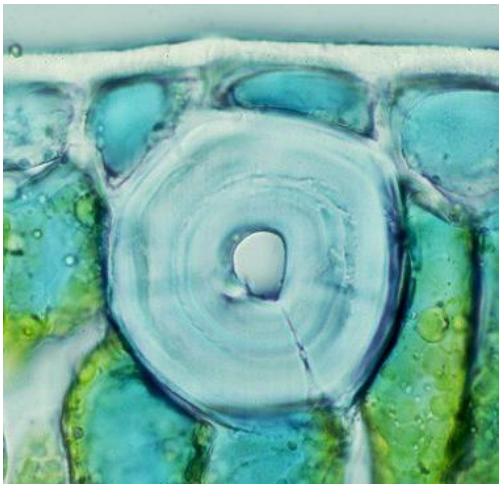

Figure 5. An image of a sclereid from podocarpus leaf under light microscopy with polarized filters [22]

Beekman et al [23] determined the failure mechanism for industrial enzyme granules using repeated compression tests; presented the advantages and disadvantages of constant strain rate tests, controlled force tests and double spring compression fixture. These granules are composed of e.g. ethoxylated c18 fatty acid some others are layered with salt or sugar cores having inhomogeneous structure and differing composition Granules were tested and based on the study of the fracture surface and force-displacement curve their failure mechanism was studied. Cheong et al [24] estimated the mechanical properties of dry binderless polystyrene granules by diametric compression at a constant platen velocity using the power law relation described by Hertz contact expression between a rigid platen and a sphere. The plastic material properties were determined using the relationship for load and total crosshead displacement as described in Johnson [25]. Antonyuk et al [26] described the deformation and breaking behavior of industrial granules like synthetic zeolite, sodium benzoate etc under single particle compression tests. They also developed an elastic plastic contact model to describe the deformation of granules. The response of the

granules was classified into categories like elastic, elastic-plastic and plastic. Effects of granule size, loading rate and contact stiffness were studied.

Spatz H.-CH et al [27] studied the strengthening tissue of young axes of *Aristolochia macrophylla* and distinguished the elastic, viscoelastic and plastic deformations by carrying out load-unload cycles under tensile loading. The changes in microstructure notably the change in cellulose fibril orientations due to loading were considered as the main reasons for plasticity. Cell wall structure and its relation to the mechanical characteristics in different plant tissues were studied by Lothar Kohler and Hanns-Christof Spatz [28]. Mainly the region beyond the linear elastic range was studied. A model was proposed which explained the phenomenon of the biphasic stress-strain curves and demonstrated the micromechanical processes which occur during viscoelastic and plastic yield in plant tissues.

1.3 Research Objectives

The principal objective of the research is to explore the mechanical response of coated and/or infiltrated ground walnut shell particles under compression. Study the single particle compression response and develop computational models to simulate the experimental response to enable the development of virtual parametric test bed capability.

2 BIO-CELLULAR MATERIAL COMPOSITION AND MICROSCOPY OBSERVATIONS

In order to estimate material properties of walnut particles, microscopy studies of the bio-cellular microstructure are undertaken. The cell walls of the ground shells are considered to be composite where the cellulose is considered a fiber and the matrix is composed of hemicellulose and lignin. A schematic of the constituents are displayed in Figure 6. The cell wall of wood has multiple layers with varying properties; these layers include the primary cell wall and the secondary cell wall. The secondary cell wall is further divided into layers differing in composition and cellulose microfibril orientation [16]. The effective property calculation of this composite gives us the cell wall property. A walnut shell has also been defined as equivalent to a wood structure [18].

Herein, the details of cellular microstructure of walnut shell are presented. The relationships of the effective elastic properties of the walnut shell as a whole and of its cell walls are discussed. Polymer coated particles are studied to determine the coat thickness and/ or the depth of polymer infiltration into the particles.

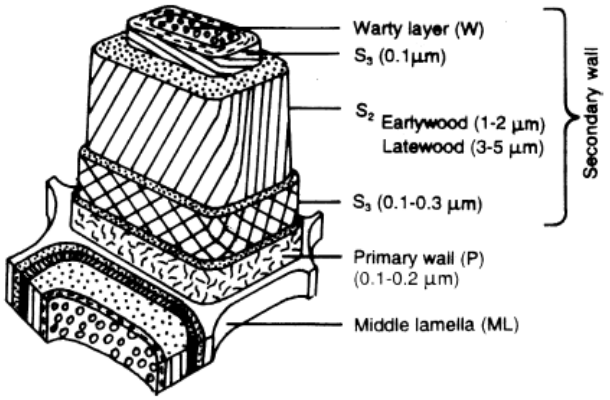

Figure 6. Schematic diagram to illustrate general structure of a wood cell wall [16]

2.1 Walnut Shell Microstructure

The study of the walnut shell microstructure is carried out to estimate a) the material properties based on its cellular structure and b) detect the polymer coat on the coated particles and determine the presence or absence of infiltration. Two different microscopes were used to study the microstructure a) E3 - ESEM and b) Zeiss Axiophot Light microscope.

2.1.1 E3- ESEM Images of Walnut Shell Fracture Surfaces

Three different walnut shell particle sizes were used for microscopy studies; large uncoated flakes (4X6 mesh), 20X30 mesh coated particles and 20X30 mesh uncoated particles. The mesh numbers indicate the number of openings over a distance of one inch on a screen [29]. Accordingly for a 4X6 mesh the size of an opening in a screen is (4.76 – 3.76 mm) and for 20X30 meshes (0.841 – 0.595 mm). The specimens were observed under the E-3 ESEM (environmental scanning electron microscope) at the Microscopy and Imaging Centre, Texas A&M University. Specimens for microscopy observation were prepared by fracturing under a sharp blade. ESEM images were acquired on the fracture surface of the flakes from the external edge to the internal edge along the shell thickness to capture the variation in cellular structure. The advantage with flakes is that before we capture the images we exactly know the surface which we want to study hence the images which we capture can be related to a specific region and any variation in the cell structure in the walnut shell can be studied. The ground particles aid in addressing the presence of isotropy since the grinding procedure may have resulted in random orientation of cell walls.

A schematic of the flake defining the surfaces for ESEM image capture is shown in Figure 7. The ESEM images Figure 8-9 are captured along the thickness of the shell on the fracture surface from the external edge towards the internal edge to display any variation in cell structure. ESEM image on the external surface is shown in Figure 10. A high magnification image of the fracture surface to study the cell structure in detail is

depicted in Figure 11. The images on the fracture surfaces of coated particle and uncoated particle are shown in Figures 12 and 13.

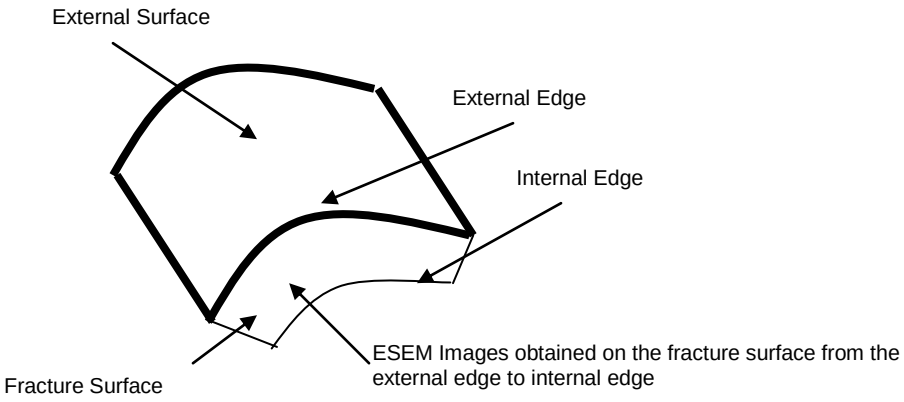

Figure 7. Schematic of an uncoated walnut shell flake

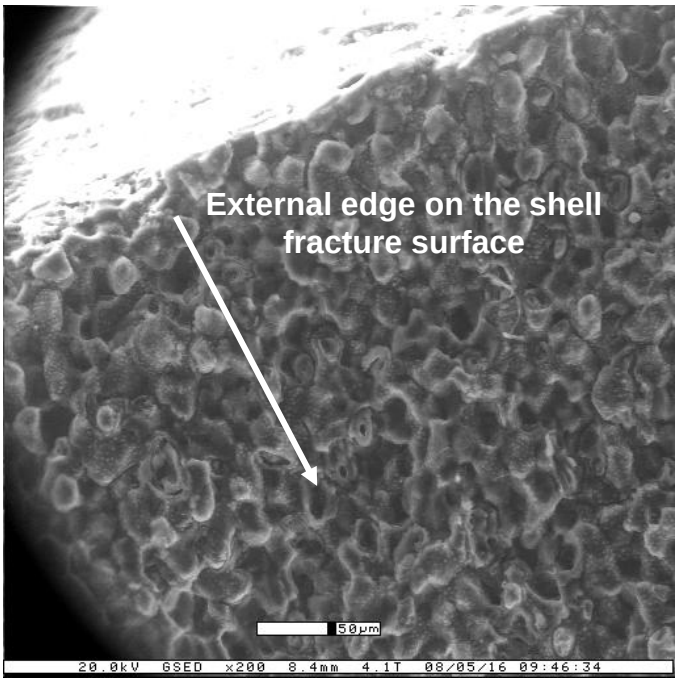

Figure 8. ESEM image on fracture surface near the external edge

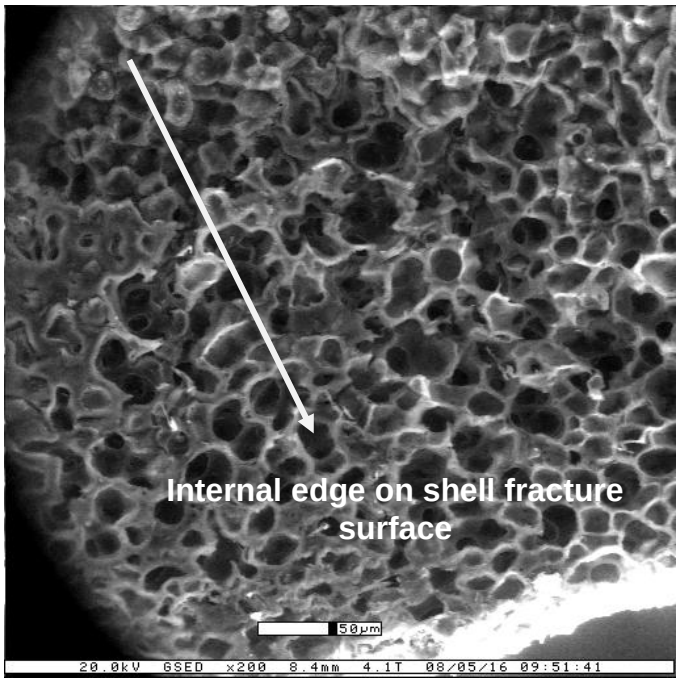

Figure 9. ESEM image on fracture surface near the internal edge

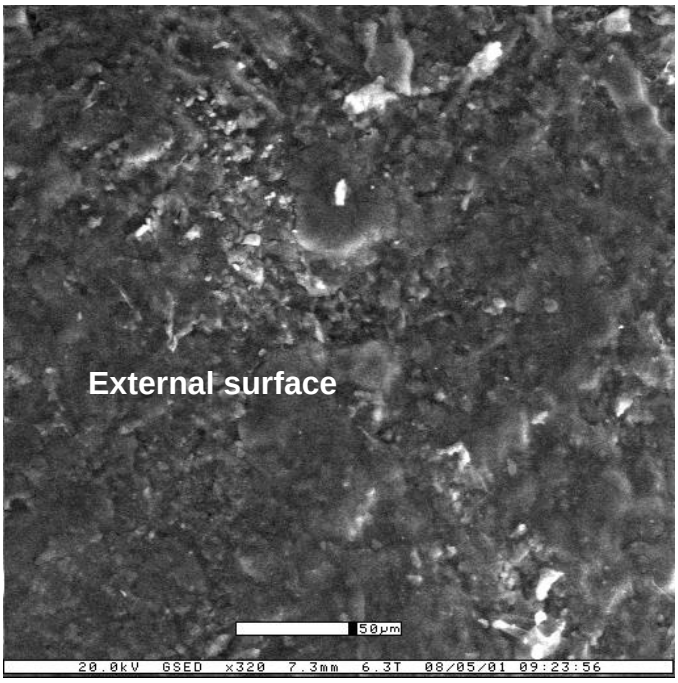

Figure 10. ESEM image on the external surface of the walnut shell flake

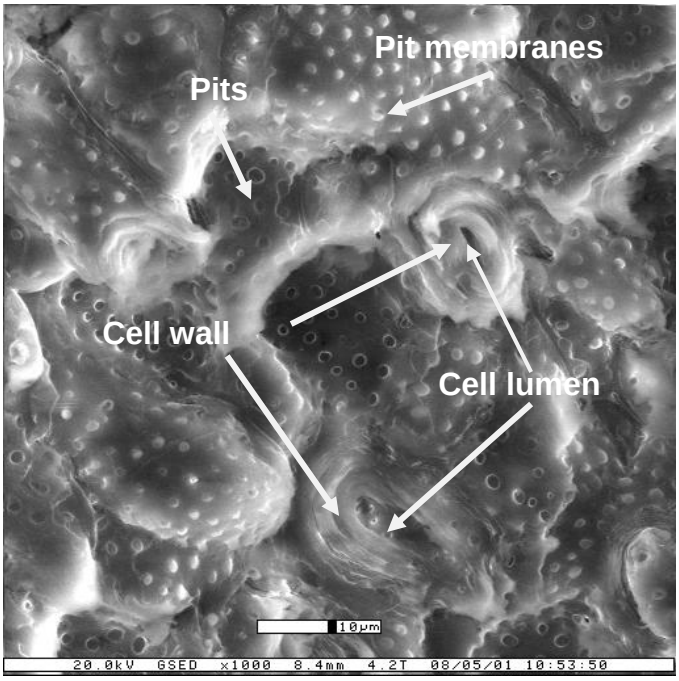

Figure 11. A high magnification ESEM image on a fracture surface

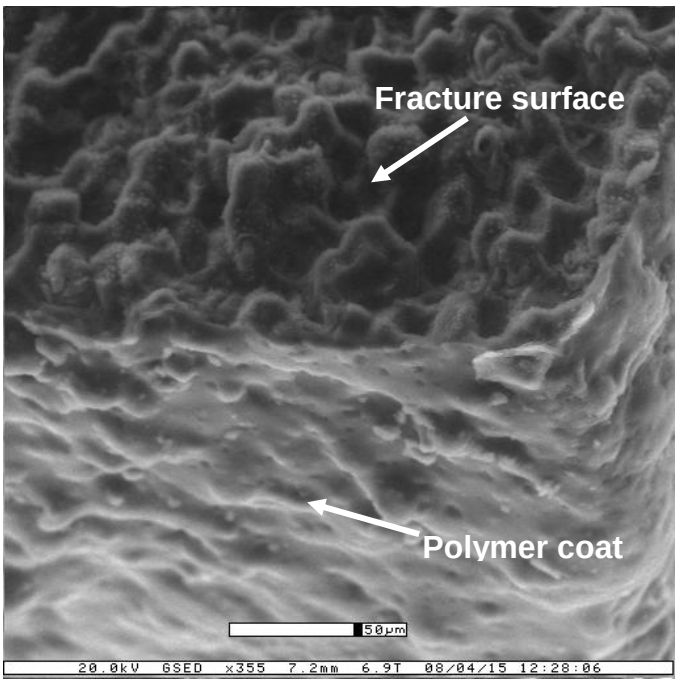

Figure 12. Image of a fracture surface of coated particle

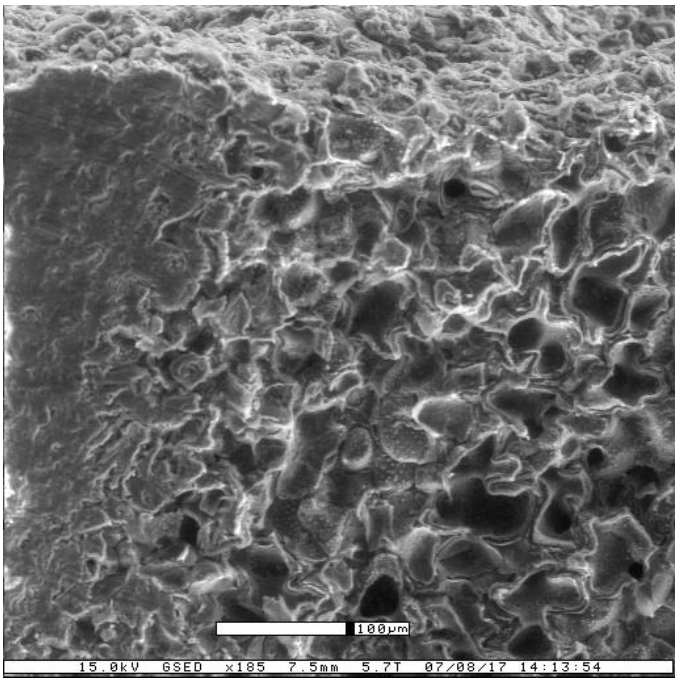

Figure 13. Image of a fracture surface of uncoated particle

The walnut shell has a porous soft layer near its inner edge. This layer can be considered to be as a foamy layer and equivalent to the foam on the interior of a crash helmet. Its outer surface is a layer of suberin with little porosity. This layer provides a barrier for moisture and other chemical attacks and protects the nut. Figure 11 is a high magnification image of the fracture surface near the outer edge and describes the cell structure of the walnut shell in detail. The cells in this region display a small lumen with a thick cell wall. These cells are sclereids [21]. Almost 90% of cell volume is attributed to the cell walls with high strength and stiffness. The small visible holes of about 1 μm are referred to as pits which connect cells through the cell wall providing a passage for water and nutrients. The fracture surfaces in these images consist of troughs and crests which are attributed to peeling of cell walls. Figure 12 and 13 show the fracture surfaces of coated and uncoated particles. The images show a similarity in the presence of troughs and crests and cell orientation which appears to be random indicating an isotropic structure of the shells. Also sclereid cells are isodiametric and don't possess an

anisotropic property attribute like fibers in case of woods. The polymer is clearly embedded onto the fracture surface of the coated particle in figure 12. However, it is our conjecture that due to the high polymer viscosity it has not penetrated into the pits.

2.1.2 Thick Section Images from Zeiss Axiophot Light Microscope

In addition to the ESEM images of the fracture surfaces of walnut shell flakes and coated and uncoated particles, images were also captured from the Zeiss Axiophot light microscope at the Microscopy and Imaging Centre, Texas A&M University. The basic objectives of this exercise were to study the cell structure and identify the presence of polymer coat on the particles. Only the coated walnut shell particles were studied.

Briefly the sample preparation procedure is discussed.

- Particles were placed in 5% Acrolein for 24 hours. Acrolin is a fixative – fixation is carried out to preserve the cell structure.
- Acrolein is replaced with the HEPES buffer.
- Replace HEPES with Osmium tetroxide (OsO_4) to enhance contrast during image acquisition. Particles are stored for 24 hours in refrigerator at 4 °C.
- Dehydration of the samples is carried out to remove all traces of moisture from the samples.
- Prepare resin for particle embedment. In the present case Quetal 651 – 11.58% wt, ERL 4221 – 10.94% wt and Araldite 502 – 11.87% wt are combined to form the resin, curing agent NSA – 65% wt is added to this blend.
- Particles are placed in moulds and resin blend is poured into the mould and then allowed to cure.
- Thick sections ~ 2 μm are cut from the embedded particles on the ultramicrotome.
- The sections are placed on slides, allowed to dry and then lightly stained with toluidine blue for 30 seconds for contrast.
- The sections are covered with cover slips and then observed under inverted light on the Zeiss Axiophot light microscope.

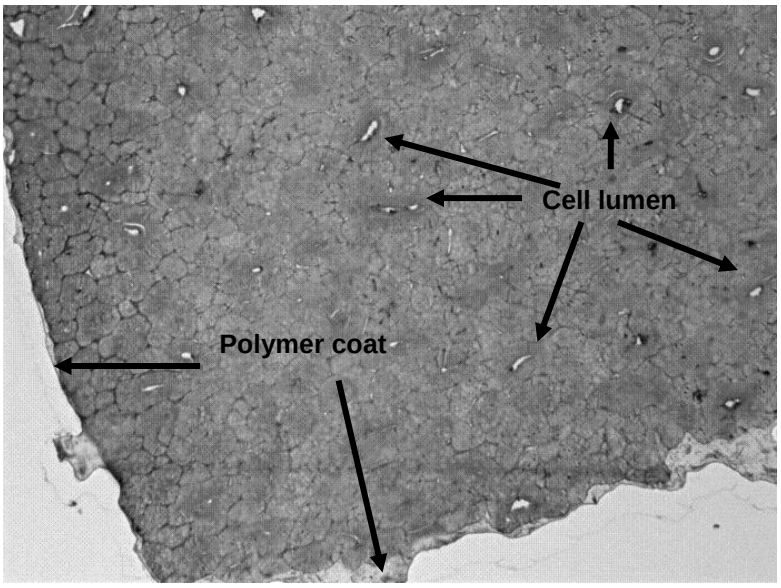

Figure 14. Image of coated walnut particle section at 10X magnification

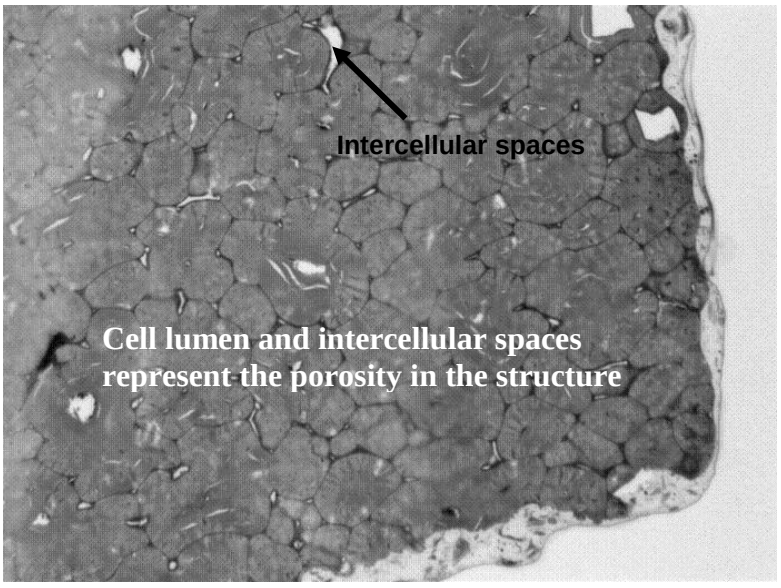

Figure 15. Image of coated walnut particle section at 20X magnification

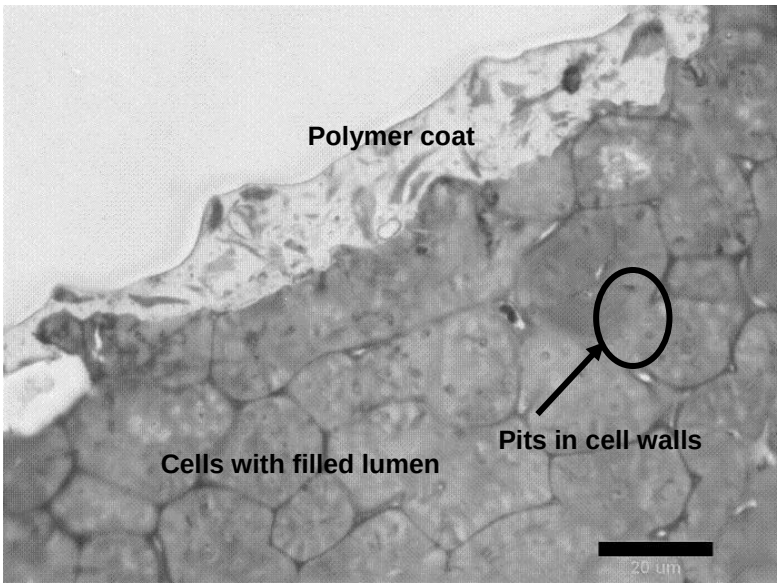

Figure 16. Image of coated walnut particle 2 μm sections at 40X magnification

The images of these sections at a magnification of 10X, 20X and 40X are presented in Figures 14-16 capturing relevant details from a single cell ~ 20 μm to the entire shell section ~ 500 μm in size.

The image in Figure 10 displays that the porosities which are scattered in the section occupy about ~ 10% of surface area. If we consider that this section is representative of a particle, then it may be stated that the porosity of a particle is ~ 10%. Porosities are located at the cell lumina though in some cases these are also the intercellular spaces. Also note that a thin layer is detected on the external edge of the particle section, it is assumed that this layer is the polymer coat. The images at 20X and 40X (Figures 15-16) provide greater insight into the cell structure and the polymer coat. From the 20X images it can be stated that the cells are rounded in shape and show a scatter in their dimensions, assuming the cells to be circular the diameters range from ~ 20 μm to 60 μm. Majority of the cells show the lumen completely covered by the cell wall growth. At 40X the polymer coat is clearly visible. Measurements of this outer layer indicate thickness ranging from ~ 5 μm to 15 μm. Resin impregnation through the thickness has not been detected.

The ESEM and the LM image study observations lead to the conclusion that the walnut shell cells are sclereids with ~ 10% porosity. From the images it appears that the cells have a random orientation and hence isotropic material property description is acceptable. It is assumed that due to the small diameter of the pits and high polymer viscosity infiltration is not possible.

2.2 Effective Elastic Modulus Estimate

The elastic modulus of walnut shells depend on primarily the ratio of walnut shell density and the density of its cell wall. The density of the cell wall for different wood species is specified as 1500 kg/m^3 [12]. From the experimental data the density of raw (uncoated) walnut shell particle is 1290 kg/m^3 [30], leading to a density ratio of about 0.86. This is also corroborated by the ESEM and LM images of the microstructure and cell type of walnut shells as sclereids which indicate a very low porosity ~ 10% in the structure.

The cell wall of the ground walnut shells can be treated as a laminated composite where cellulose is the reinforcing fiber and hemicelluloses and lignin form the matrix as idealized in Figure 1 [16]. Demirbas [13] stated that the composition of walnut shells is 22.2 % by weight hemicellulose, 25.5 % by weight cellulose and 52.30 % by weight lignin. The elastic modulus of cellulose as presented by Bergander and Salmen [15] is 135 GPa while that for lignin is 2 GPa and hemicellulose is 7 GPa. Based on the density ratio and the effective properties of the cell wall, the axial and transverse elastic modulus for walnut shell is then estimated from expressions (1a, 1b) [12]. The details of the derivations are presented in Appendix A.

$$E_{axial} = E_{wall}\left(\frac{\rho_{material}}{\rho_{wall}}\right) \tag{1}$$

$$E_{transverse} = 0.54 E_{wall} \left(\frac{\rho_{material}}{\rho_{wall}} \right)^3 \quad (2)$$

The values obtained are observed to be in the range of 8.6 – 30.1 GPa for axial modulus and 3.5 – 10 GPa for transverse modulus.

We further assume that due to random grinding to produce small mesh particles and from the ESEM and LM image study of the microstructure the elastic modulus will be isotropic.

2.3 Coated Walnut Shells

The mechanical properties of a polymer coated particle depends on two factors a) the polymer properties and b) the level of polymer infiltration/ deposition on the surface of the particle. For any particle belonging to a specific batch the polymer remains constant and hence the properties of the coated particle depend on the level of polymer infiltration and/ or polymer deposition on the particle. Two approaches can be adopted in estimating the level of polymer presence on the particle. The first approach is based on analytical expression of surface roughness of a ground particle while the second is direct experimental approach where the particle section images are used to measure the polymer coat thickness and/ or level of polymer impregnation into the particle.

Analytical Approach – Integrating Surface Porosity:

The previous discussion on walnut shell particle microstructure has established the porosity to be ~ 10%. It has been assumed that the polymer is not able to infiltrate into the shell but settles on the outside surface which is generated by the shell fracture due to grinding. The amount of polymer on this surface can be obtained by assuming that it covers all the trough regions on the surface which we define as the (surface porosity). The volume fraction of the trough region can be calculated by estimating the

depth of the troughs. The preferred mode of fracture for wood structures is through cell wall peeling [12] and hence the depth of troughs can be assumed as equal to the radius of the cell. Knowing the surface porosity we can calculate the amount of polymer on the surface and hence based on the calculations of the 3-phase model for micromechanical modeling of spherical inclusions in a matrix (Appendix B) we can obtain the effective property of the surface region of the shell. It is to be noted here that all the particle faces have been assumed to possess the same characteristics. The study of walnut shell section under ESEM concluded that differences in the structure exist as we move from the inner surface which contacts the fruit to the outside surface, Figures 8 and 9 displayed the two regions. The outside surface exposed to the environment has a suberine coat which has a smoother surface and possesses barrier properties. Thus it can be assumed that when the polymer is applied on this surface it only encounters a very small surface porosity and most of polymer will be placed as a layer of neat epoxy on the surface. In our calculations we neglect the presence of a suberin layer and consider all the surfaces to be formed from the fracture of shell as is observed in Figures 8, 12 and 13.

The primary challenge then is in determining the surface porosity from the ESEM images. We use image processing techniques for this effort.

The ESEM image was processed using GIMP software [31]. The procedure for the same is discussed below through the images in Figure 17 (a, b and c). The original image in Figure 17(a) is cropped to concentrate only on the trough surface Figure 17(b). The histogram threshold which modifies the contrast of the image is modified such that the dark spots on the image representing the cavities are differentiated from the troughs which appear brighter. The final modified image is shown in Figure 17(c).

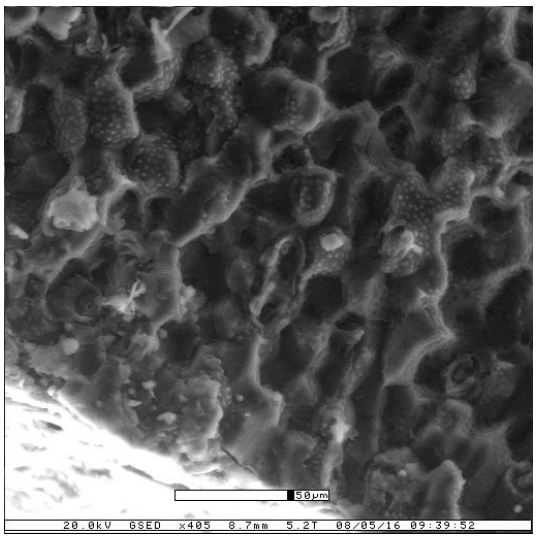

(a) Original image

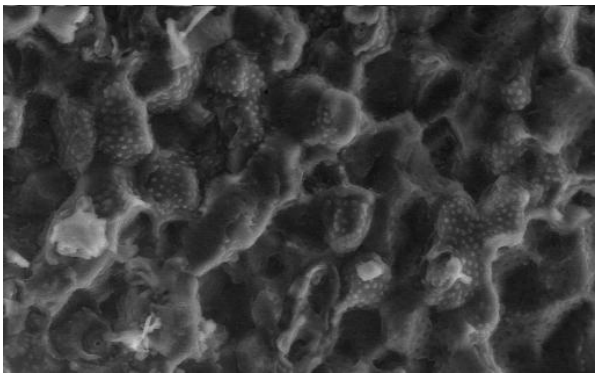

(b) Cropped image

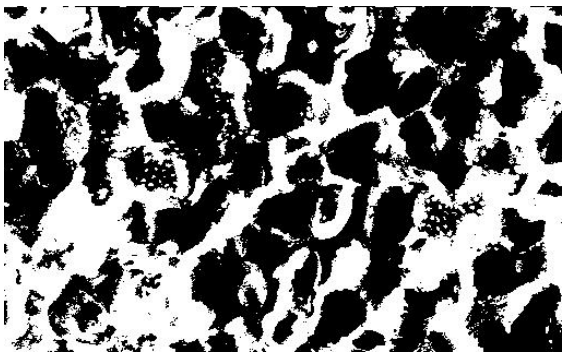

(c) Final modified image

Figure 17. ESEM image processing procedure

Black colored pixels in the processed image define the surface porosity which is about 56.6% for this image.

Based on the surface porosity and cell dimensions, the volume of polymer deposited on the particle that occupied the troughs can be calculated. This representation can be described as a 3 layered particle, the inner core of walnut shell properties; the middle layer as a composite which is formed with the crests of cell walls

acting as matrix and the polymer deposited into the troughs as inclusions. The external layer of neat polymer which extends over the crests forms the third layer. A representation is displayed by a schematic in Figure 18. The mechanical properties of the walnut shell have been estimated in section 2.2, the properties of the neat polymer can be determined from experimental study or through literature, the properties of the middle layer composite can be determined from micromechanical calculations based on the volume fraction and the properties of the crests (cell wall properties) and polymer inclusions (neat polymer properties).

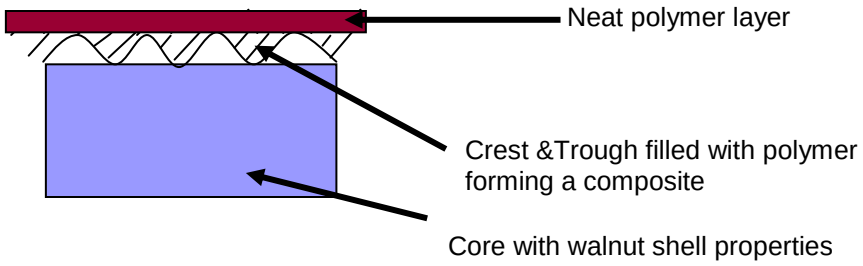

Figure 18. Schematic of composite coated particle system

Experimental Approach

The level of polymer deposition on the particle can be determined through study of thick sections ~ 2 μm of the particles. The LM image study of such particles indicates polymer presence on the surface. The thickness of polymer coat is estimated to range from ~ 5 μm to 15 μm. But no direct evidence of polymer infiltration is noted. Thus the model selected for the coated particles is a two layer system with the inner core of walnut shell properties and outer polymer coat with thickness as determined from the images.

It has been confirmed from the polymer manufacturer that the polymer contains sulfur as a catalyst [32]. It is known that walnut shell being an organic material has carbon as a majority element. As the atomic number of sulfur is 16 and carbon is 6, backscatter electron imaging on the JEOL 6400 SEM at the Microscopy and Imaging centre, Texas A&M University is used to detect sulfur and hence the polymer on the section of the coated particle.

Backscatter is capable of distinguishing between elements with atomic number difference of 3. This is represented by a contrast in the image with the higher atomic number element appearing as a bright field [33].

The coated particle of walnut shell is embedded into a resin (procedure same as discussed previously for specimen preparation for LM observations), thick sections ~ 2 μm are cut on ultra microtome. These sections are placed in the SEM chamber and observed through the backscatter mode. Bright fields are detected on the external edge of this sample as noted in Figure 19. The image shows a thin layer of ~ 5 μm over most of the edge and a thicker segment of ~ 15 μm.

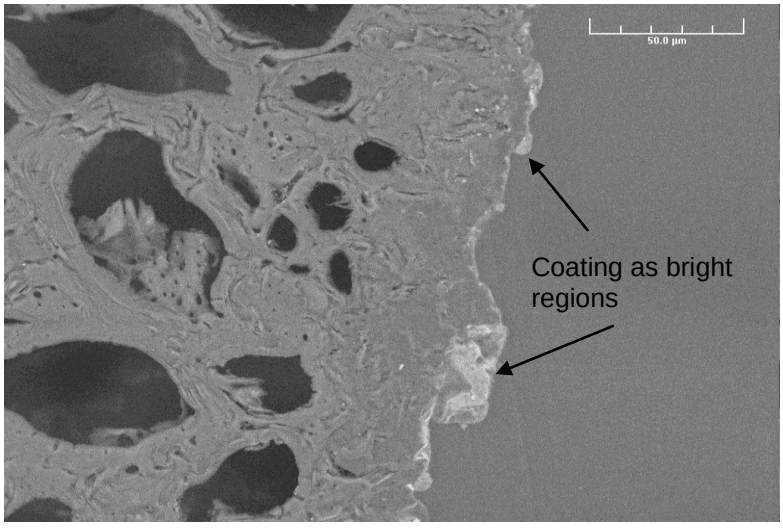

Figure 19. Backscatter image of a section of coated walnut shell

In summary, walnut shell sections are studied using different microscopy tools like ESEM, Light microscopy and the SEM with back scatter. The cells of walnut shell are defined as sclereids and ~ 10% of a particle displays porosity. Micromechanics and cellular solid concepts are used to estimate the elastic properties of an uncoated walnut shell particle. The particle is assumed to possess isotropic material properties.

Attempts are made to identify the presence of a polymer coat on the particle surface using LM and SEM backscatter imaging techniques. Preliminary studies indicate no polymer infiltration while the coating thickness is estimated to range from ~ 5 μm to15 μm.

3 EXPERIMENTAL APPROACH

Experiments are conducted to study the mechanical response of the particles to compressive and thermal loads as well as to develop screening techniques to assess polymers for coatings. Thus three main tests, single particle compression, particle heating and 3-point flexure tests on coated and uncoated walnut shells are undertaken. The single particle compression tests are selected to study the mechanical response under compressive loading to identify the effect of particle shape and coating. To understand the influence of temperature on the particles and to identify the coating resistance the particles are placed in the heating chamber of E-3 ESEM. The 3-point bend test is studied as a screening test for the qualitative analysis of different polymer coats and their impact on the overall stiffness of a multiple particle interaction application.

3.1 Single Particle Compression Testing

Single particle compression tests are carried out utilizing the horizontal test bed (No. 18246 tensile testing substage by Fullam Inc.) equipped with a 1000 lb load cell (Figure 20). This is coupled with software **MTESTWindows^{TM}** (ADMET, Inc.) which interfaces with the user and regulates the test. Loading is controlled through servo control. Direction of loading is controlled through a toggle switch on the control box. For compressive loading the toggle switch is set to C. The primary output requested is the load vs displacement data. Test is conducted by mounting the test stage onto an optical microscope (Olympus SZX 16) (Figure 21) to observe particles during loading. A general description for compressive loading is described below.

Set the toggle switch on the controller to C for compressive loading. Move the loading crosshead to contact the specimen. From the test setup window, define the geometry of the specimen by inputting the values of the specimen dimensions (L, W and

t), Required output to be calculated - we only request for the peak load for single particle compression tests, select appropriate load cell (1000 lb Tensile), select the control for loading (displacement control/ Force control), appropriate loading rate – 0.01 mm/sec with displacement control in our case. Start the test. Based on the above mentioned inputs the controller provides the drive to the loading crosshead. A transducer measures the displacement of the crosshead. The primary output is the force-displacement curve.

Figure 20 also shows the compression fixtures and the mounted test particle. The fixture consists of two anvils, one acting as a specimen mount and other for load application. The length of the protruding sections is 8 mm. The dimensions of the square section of the mount are 3.20 mm X 3.20 mm. These dimensions are sufficient to support the specimen while ensuring that it does not interfere with the view from optical microscope. The specimen/ particles are mounted on the fixture face by gluing with silicon grease.

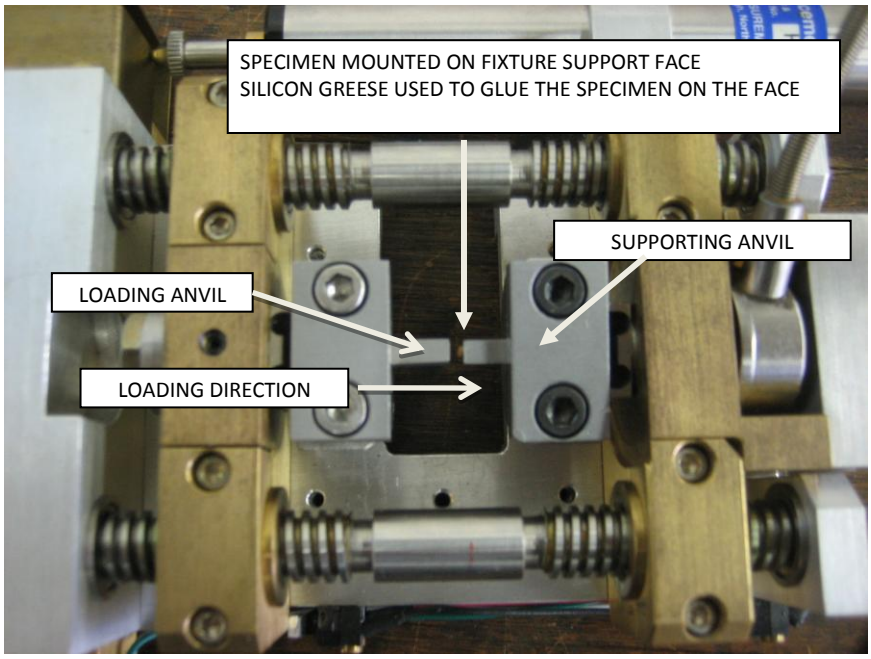

Figure 20. Compression fixture and mounted specimen

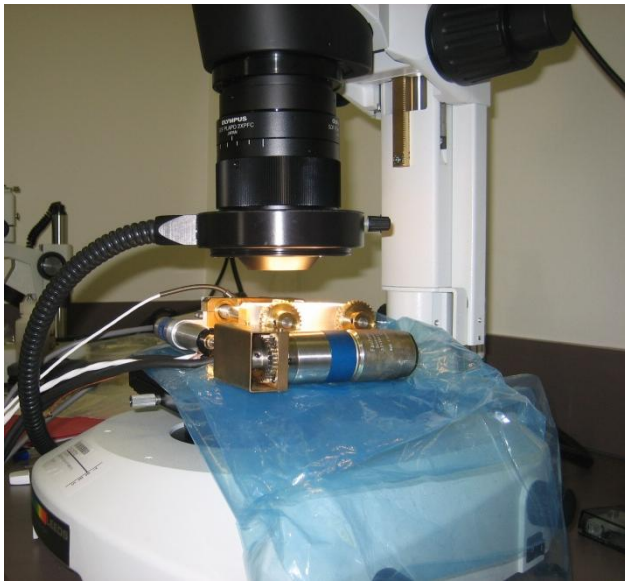

Figure 21. Testing under optical microscope (Olympus SZX 16)

3.1.1 Randomly Selected Coated and Uncoated Particles

Tests are carried out on 6 randomly selected particles each of coated and uncoated particles. The load is applied till the load vs displacement curve shows a steep rising profile indicating almost complete crushing of the particles. The images of the uncoated and coated particles respectively are presented in Figures 22 and 23; the images give an indication of the geometric variation of the test particles.

The test procedure followed is briefly stated below

- 6 samples of each (raw (uncoated) shells and coated shells) tested. Particles selected randomly from their lot.
- Displacement controlled loading

- Loading rate – 0.01 mm/sec

Experiments dealing with compression testing of spherical industrial granules like solidified droplets of ethoxylated C18 fatty acids, dry binderless polystyrene granules, synthetic zeolite etc are described in [23, 24, and 26]; these experimental procedures are taken as reference for the test procedure described above. The load vs displacement response for the uncoated and coated particles is presented respectively in Figures 24 and 25.

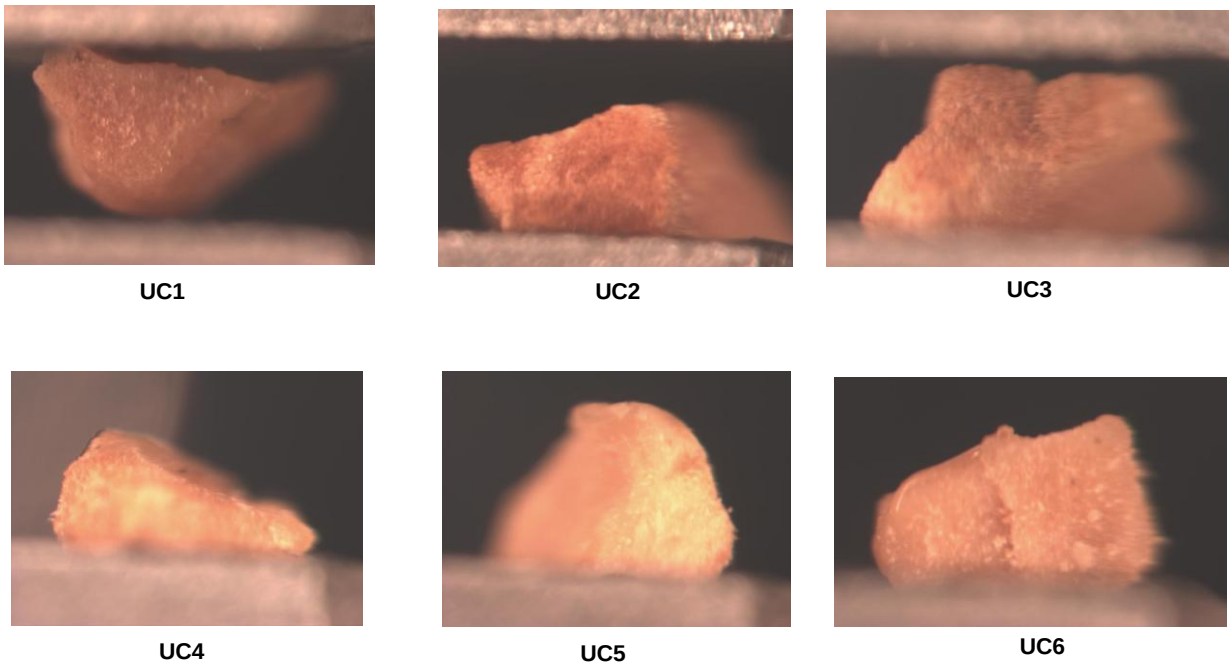

Figure 22. Images UC (1-6) are the uncoated randomly selected particles for compression tests

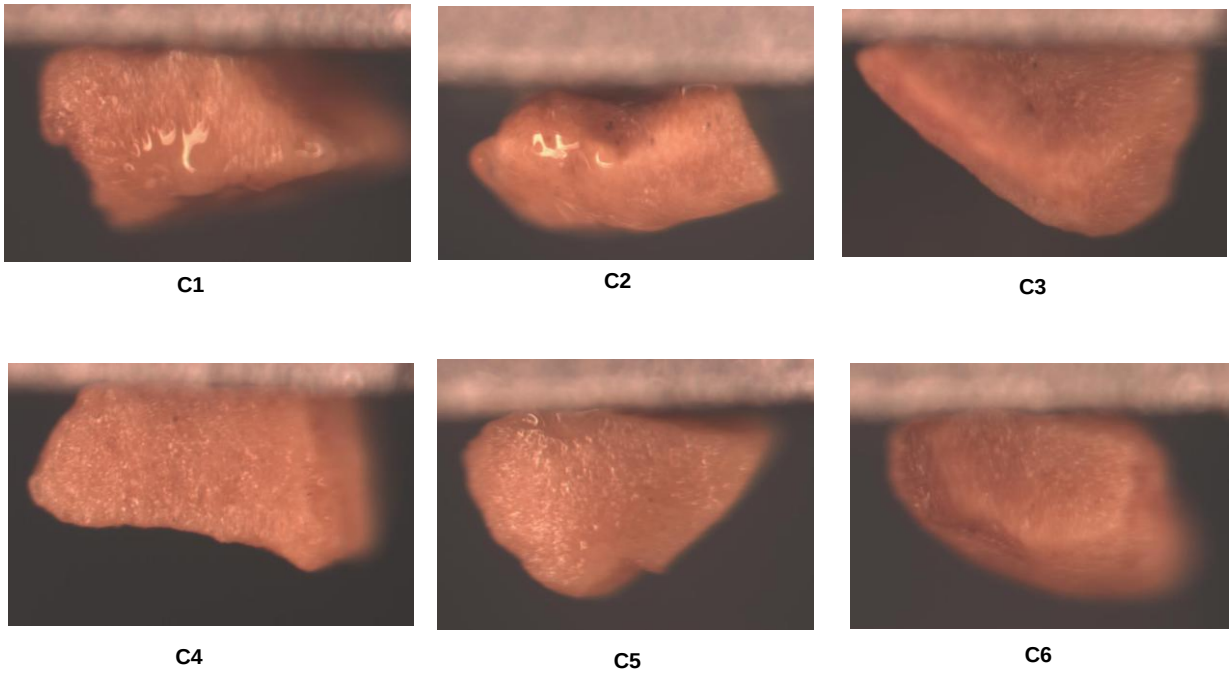

Figure 23. Images C (1-6) are the randomly selected coated particles for testing

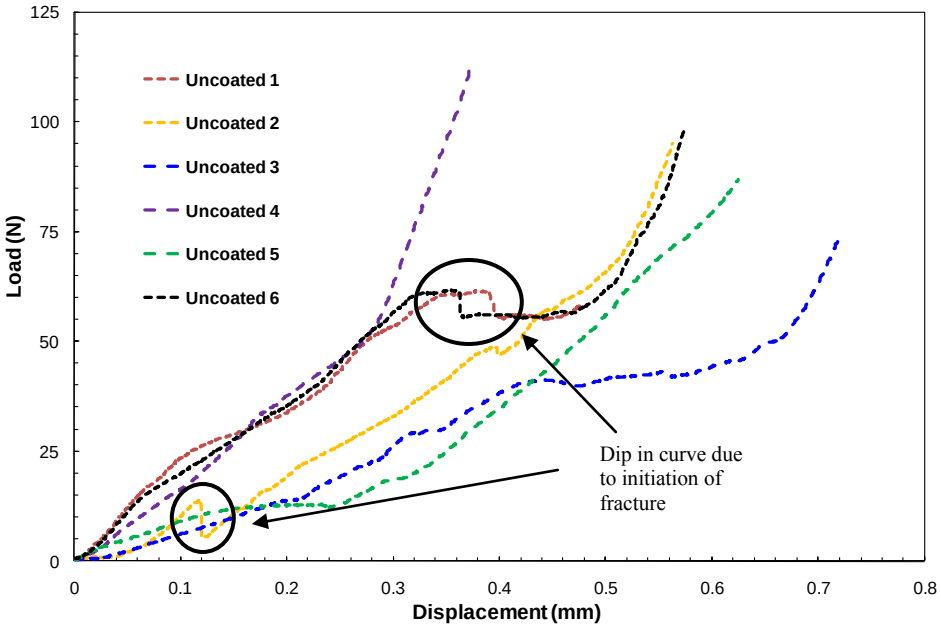

Figure 24. Load vs displacement curve for uncoated particles

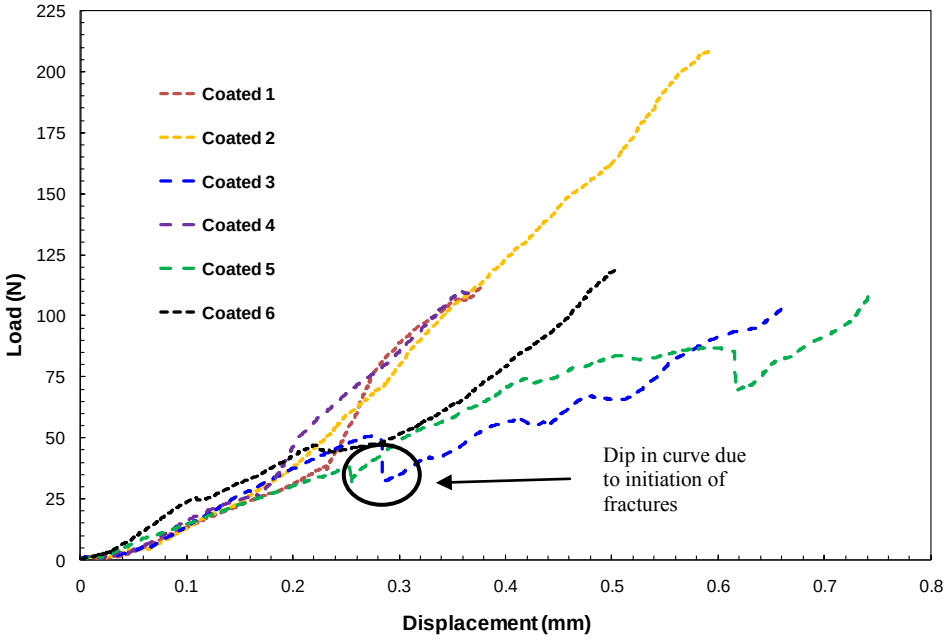

Figure 25. Load vs displacement curve for coated particles

As can be noted in Figures 24 and 25 there is a considerable scatter in the data which can be attributed to the geometry variation of each particle. The curves show a rising profile with increasing stiffness, which is due to increase in contact area with loading. The sudden change in slopes with sharp drop in loads is due to a sudden failure in the particle, these slope changes are highlighted in the figures. It is observed that for the coated particles the response is fairly clustered up to a load of ~ 30 N, followed by a wide scatter depending on the initiation of failures in the particles. There is a much higher scatter in the uncoated particles even at low loads. A comparison of coated and uncoated particles response is shown in Figure 26. It is observed that there is an overlap in the load vs displacement response of the coated and uncoated particles, at the same time coated particles dominate the space with stiffer response (highlighted) while the uncoated particles have a higher presence at the lower end of the stiffness response. It can be noted that some of the particles undergo a cross-head displacement of ~ 0.7 mm under an action of ~ 100 N load, hence large straining of particles take place at this load.

The final stages of the curve show an upwards rising trend thus indicating to complete particle crush with the final response being from the steel anvil.

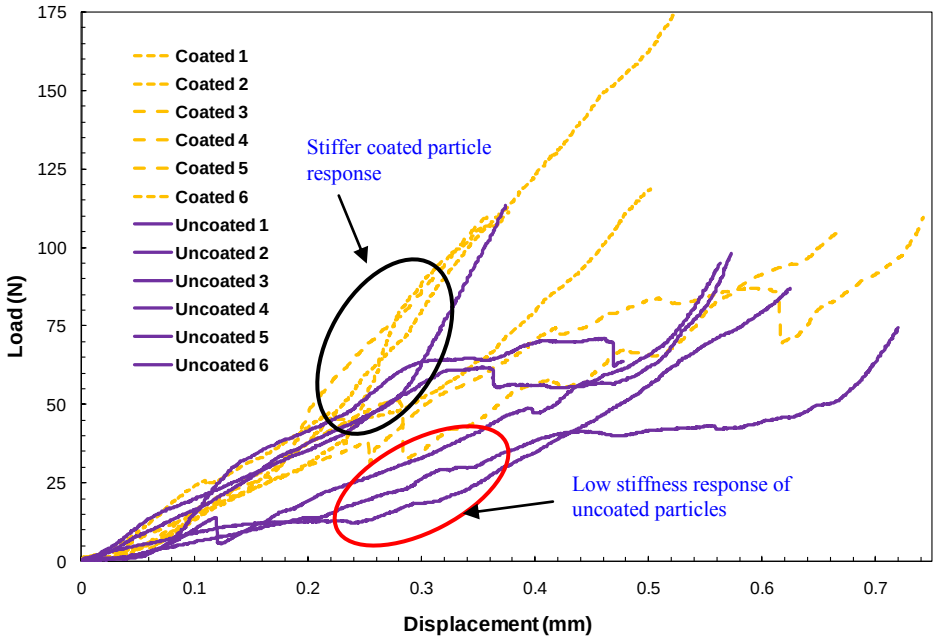

Figure 26. Comparison of coated and uncoated particle load vs displacement response

3.1.2 Geometric Classification of Particles

In order to reduce and/or eliminate scatter the particles are classified into four broad geometric groups. Herein, they will be referred to as flat-top, round-top, cone-top and large aspect ratio particles as displayed in Figure 27(a-d). Initial classification was carried out for the coated particles. Note that the round-top particles have a fairly curved profile; the cone-top has a seemingly sharp profile angle and the flat-top particles resemble cuboids. The large aspect ratio particles have one dimension significantly larger than the other two. In Figure 27(c) large aspect ratio, the cross section bounded by the two smaller dimensions is displayed. These particles are loaded normal to their largest dimension.

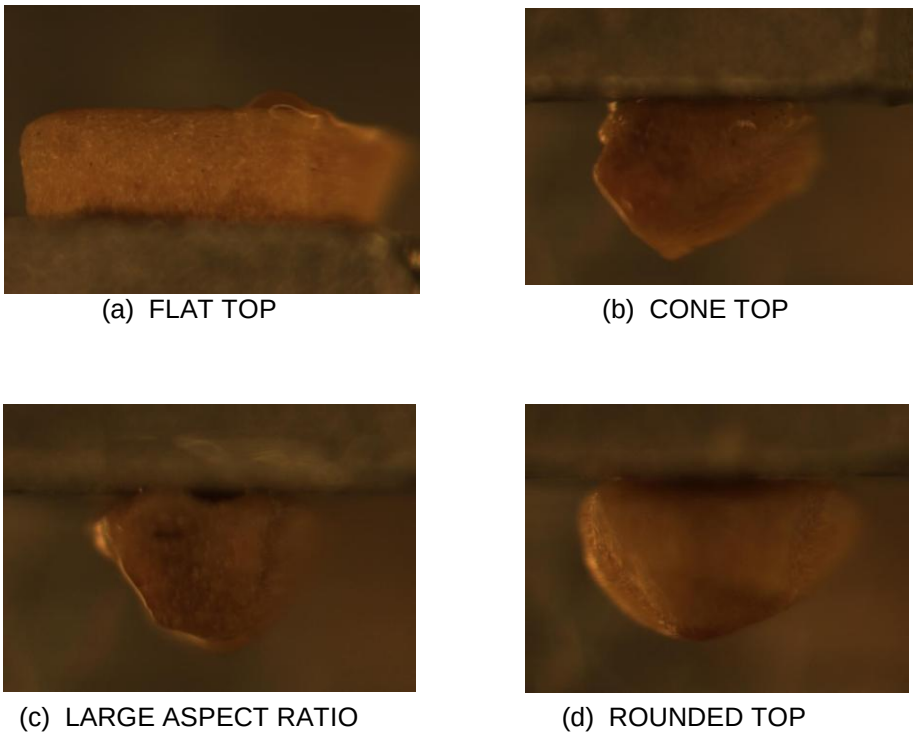

Figure 27. Segregation of particles in groups (coated particles)

5 Particles per class were tested under the displacement controlled loading at the rate of 0.01 mm/sec as in case with the previously tested randomly selected uncoated and coated particles. Initial preload was applied and held constant at 10 N and tests were terminated at a peak load of 150 N.

The results from force vs displacement responses are summarized in Figures 28(a-d), note that the flat top particles tend to give the stiffest response with the least scatter in the data. The significant variation in the response of the particles subjected to compression can be attributed to the shape effect since the shell structure for these small grounded particulates is assumed to be independent of material orientation as discussed in the section on cellular microstructure of walnut shells.

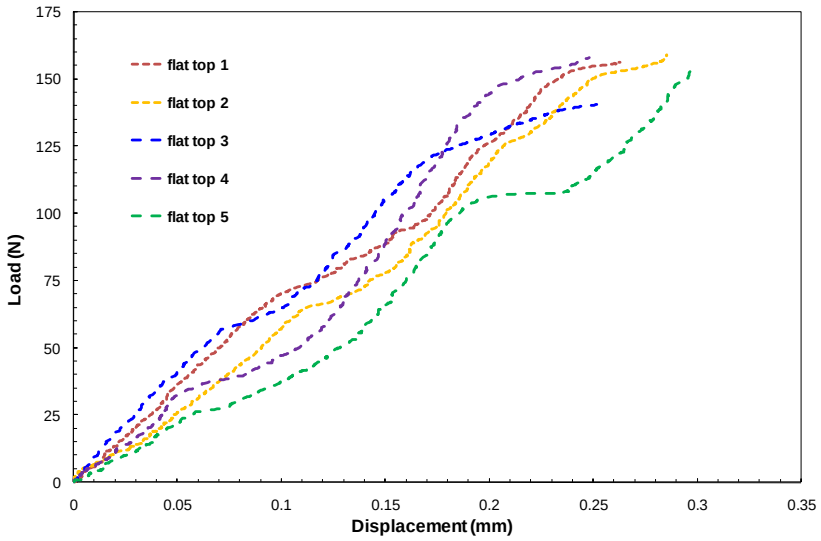

Figure 28(a). Force vs displacement for flat top particle group

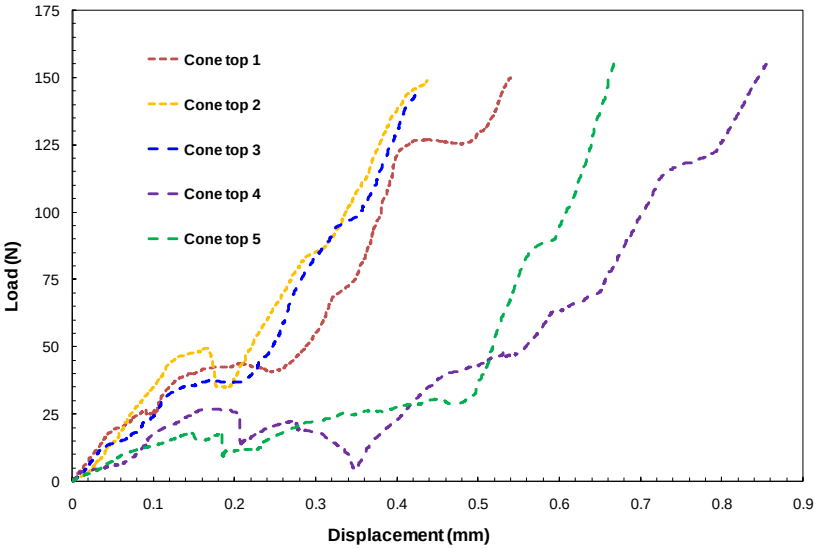

Figure 28(b). Force vs displacement for cone top particle group

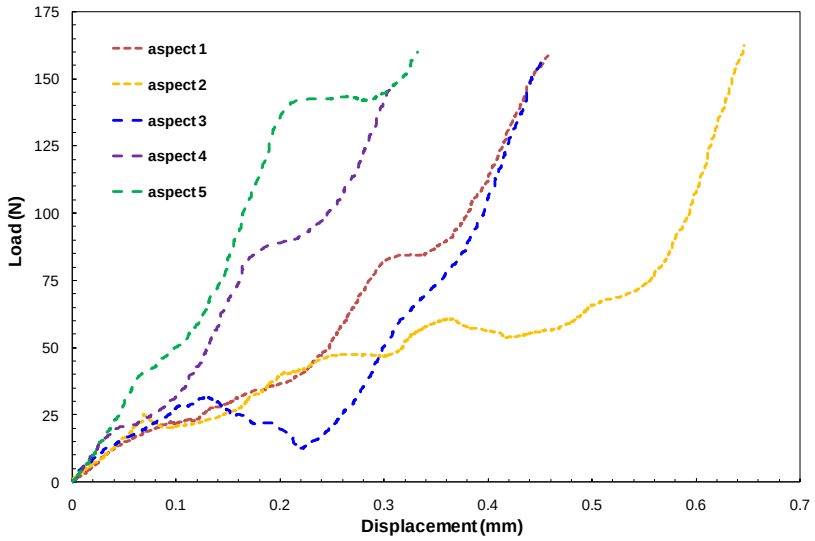

Figure 28(c). Force vs displacement for large aspect ratio particle group

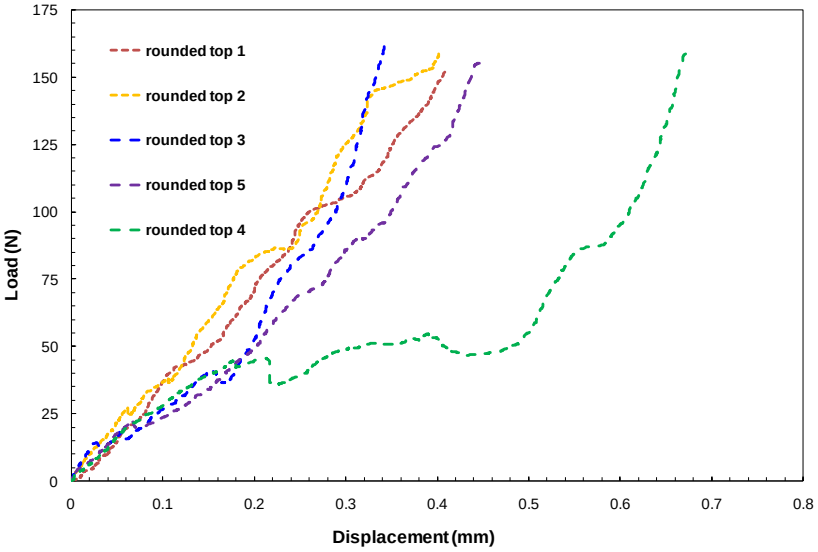

Figure 28(d). Force vs displacement for rounded top particle group

Tests on the flat top class of uncoated particles follow the same procedure as discussed for the classified coated particles earlier. Figure 29 compares the force vs displacement response of the coated and the uncoated flat top particles. It is revealed that even though, the coated particles display a higher stiffness the difference is minor. It also appears that a closer banding is observed in the coated particles compared to uncoated particles.

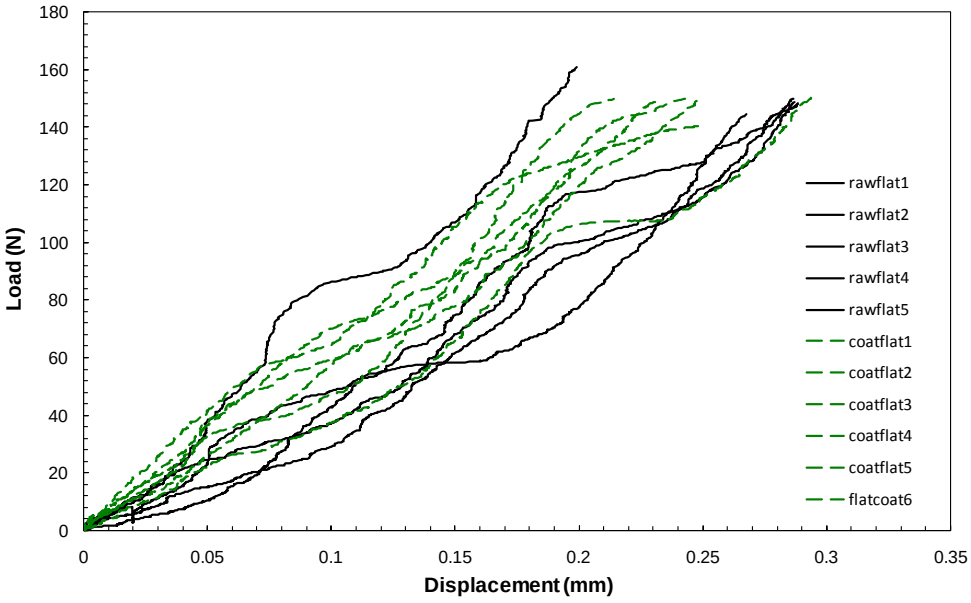

Figure 29. Comparison between coated and uncoated flat top particles

3.1.3 Loading and Unloading Cycles on Coated Particles

In addition to tests when the particle is loaded until crushing load is revealed, loading and unloading cycles are used to point out the onset of permanent deformation.. Two randomly selected coated particles are subjected to a single loading and unloading cycle. Both the cycles are displacement controlled and limited to 0.1 mm maximum displacement. The images of one of the particles before and after the cycle are presented in Figure 30. The results from these two particles are presented with three other curves obtained from BJ Services Inc in Figure 31. It is observed that the initial curve of the unloading cycle is almost vertical highlighted by the bubble in Figure 31 indicating a low strain and hence a corresponding low stress at the initiation of plastic deformation. The tests at BJ Services Inc. and by us at TAMU both show similar behavior with a low plastic strain initiation point.

In an unloading cycle the initial response would be the elastic or the recoverable displacement of the deformed particle. The almost vertical response of this curve indicates to a very little recoverable deformation in the particles and hence an early initiation of non-linear behavior. The curves obtained at BJ Services Inc, show a number of cycles with incremental loads and a non-recoverable deformation is observed at a displacement of ~ 0.02 mm and a load of ~ 5 N loads this is corroborated by the almost vertical response from the unloading curves obtained by experiments at TAMU.

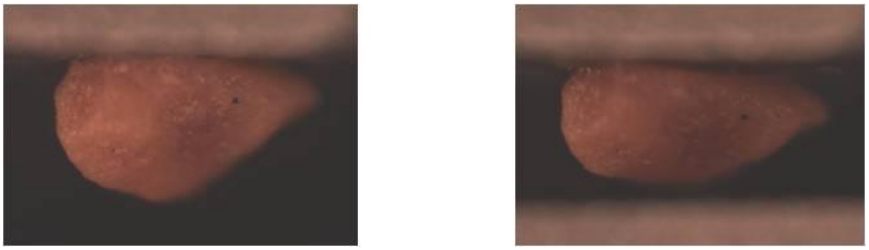

(a) Particle before loading (b) Particle after unloading cycle

Figure 30. Particle before and after the loading and unloading cycle

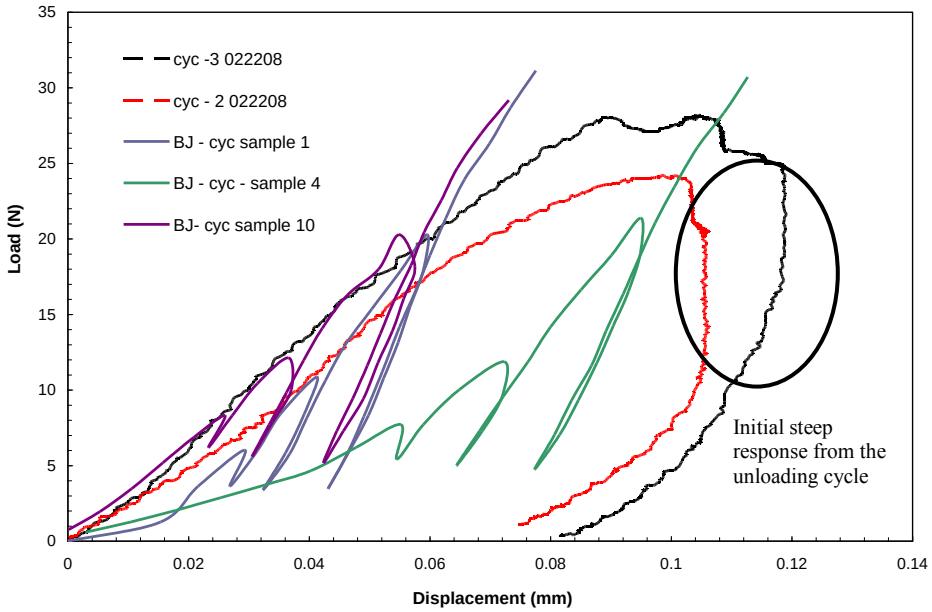

Figure 31. Load vs displacement for load unloading cycle TAMU and BJ data

3.1.4 Determination of Inelastic Material Properties

Single particle compression tests are designed to estimate the inelastic material response. The data generated from these tests is used as an input for the finite element models generated to simulate the single particle compression response. Uniformly shaped cuboids with dimensions ~ 2 mm X 2 mm X 1 mm are obtained from the 4X6 mesh size flakes of walnut shells supplied by BJ services. A jeweler's knife was used to cut the cuboids. An image of one such cuboid is presented in Figure 32. Uniformly shaped cuboids ensure a uniform compressive stress distribution thus enabling the conversion of load vs displacement response into a stress vs strain response. Cuboids also ensure consistency in test samples thus avoiding the scatter as observed in single particle tests on randomly selected uncoated particles. The loading direction is along the 1mm direction as shown by the arrow in Figure 33. In total 6 particles were tested and

loading was continued till the particles were completely crushed. The loading rate was maintained at 0.025 mm/sec as per the specifications in ASTM standard D695 – 02a [34]. The load vs displacement response for the test is presented in Figure 34.

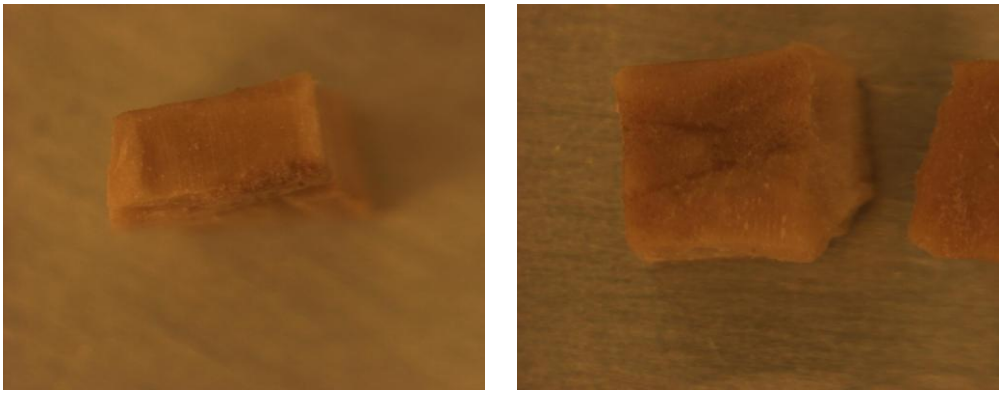

Figure 32. Two different views of uniformly cut cuboid particle

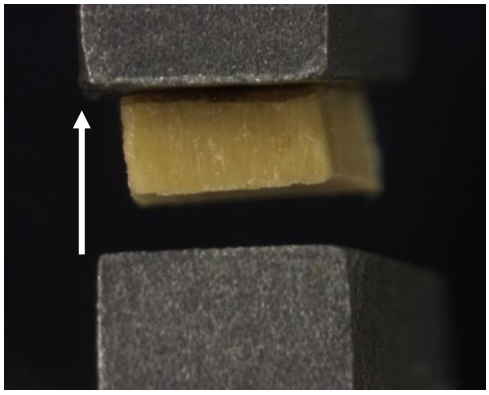

Figure 33. Uniformly cut cuboid particle before loading

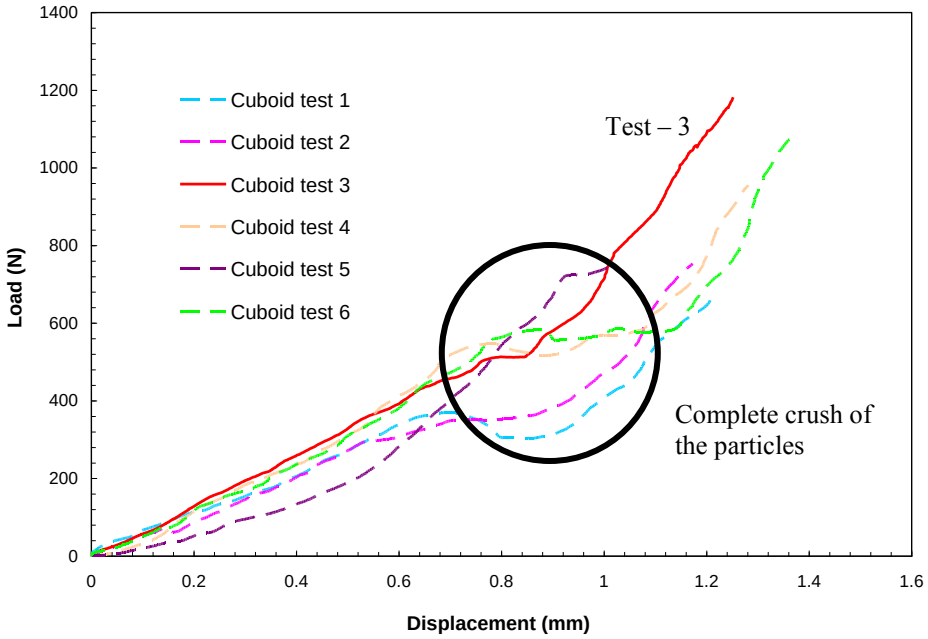

Figure 34. Load vs displacement response for uniformly cut walnut shell flakes

It is observed that on an average the particles crushed at 550 – 600 N at an axial displacement of ~ 0.8 mm of the cross-head. Of all the test data generated, Test 3 up to 0.8 mm displacement was selected to specify the non-linear constitutive relationship for the FEA model. As the particles completely crush beyond 0.8 mm displacement, the data beyond 0.8 mm cannot be used to model the particle response. The load displacement data was converted to the true stress vs strain data using the following expressions [35]. Here σ_{nom} is the nominal stress, F is the instantaneous force, A_0 is the original cross sectional area, ε_{nom} is the nominal strain, σ_{true} is the true stress, ε_{true} is the true strain and E is the elastic modulus of the material which here is 3700 MPa. The nominal stress vs nominal strain and true stress vs true strain plot is presented in Figure 35.

$$\sigma_{nom} = \frac{F}{A_0} \tag{3}$$

$$\varepsilon_{nom} = \frac{\Delta l}{l} \tag{4}$$

$$\sigma_{true} = \sigma_{nom}\left(1+\varepsilon_{nom}\right) \tag{5}$$

$$\varepsilon_{true} = \ln\left(1+\varepsilon_{nom}\right) \tag{6}$$

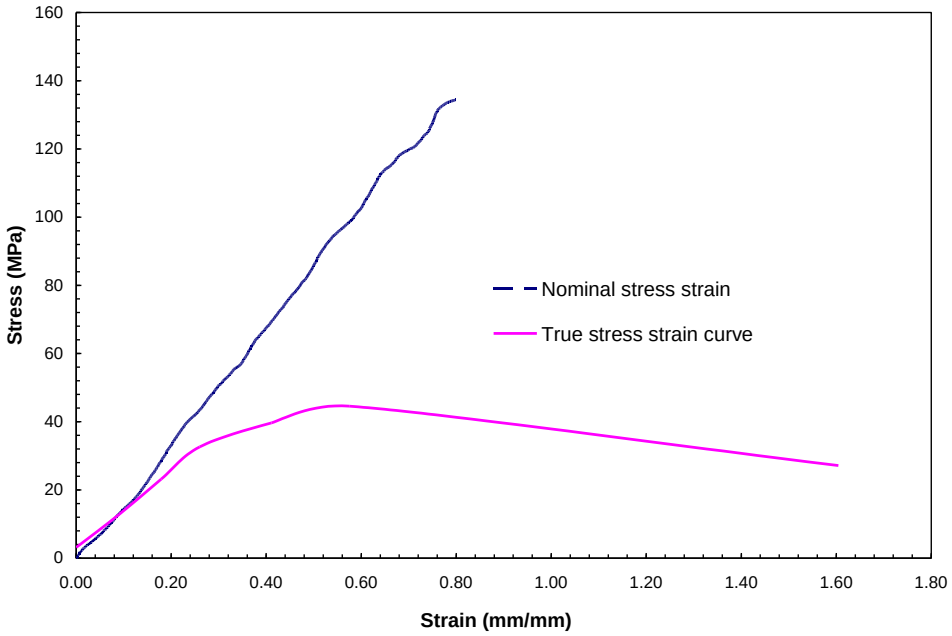

Figure 35. Nominal and true stress strain curve for Test 3 data

3.2 Temperature Capacity of Particles

Since the polymer coated proppants are subject to temperature range of 82 – 160 °C in the fissures [36], the thermal degradation potential is very realistic. In this study the coated and uncoated particles are subject to incremental heating over a

temperature range of 125 - 250 ºC in the environmental chamber of the E-3 ESEM to observe the initiation of damage to the walnut shell particles. The particles are placed in a crucible which is placed on a heating coil in the chamber. A continued cooling water supply is provided to prevent overheating of the coil. The chamber is then closed and operated under a vacuum. Signs of thermal degradation at about 175 – 200 ºC were identified as charring. Similarly Yuan HR [37] reported that the main pyrolysis took place in the walnut shells at 150 – 400 ºC. A similar exercise is also carried out with the neat epoxy polymer used for the coating. The epoxy did not show any degradation at this temperature range. The uncoated, coated and neat polymer images at different peak temperatures are presented in Figures 36-38.

Figure 36(a). OM image of uncoated walnut shells at 175 ºC

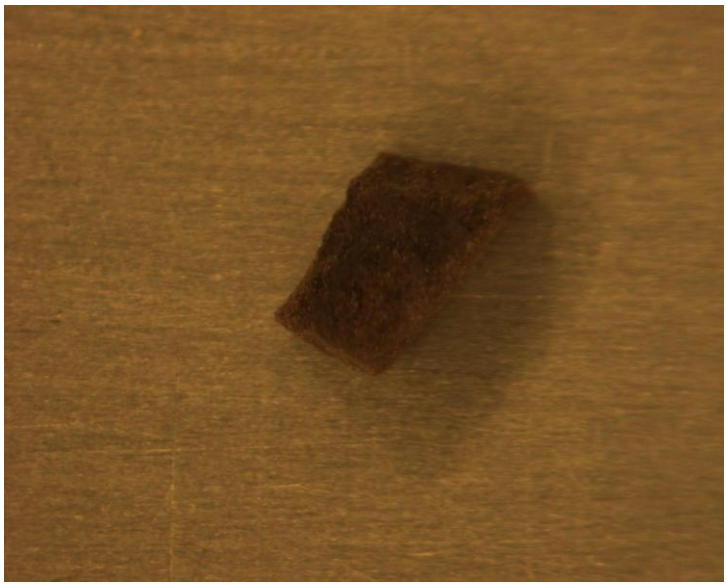

Figure 36(b). OM image of uncoated walnut shells at 200 °C

Figure 36(c). OM image of uncoated walnut shells at 250 ºC

Figure 37(a). OM image of coated walnut shells at 175 °C

Figure 37(b). OM image of coated walnut shells at 200 ºC

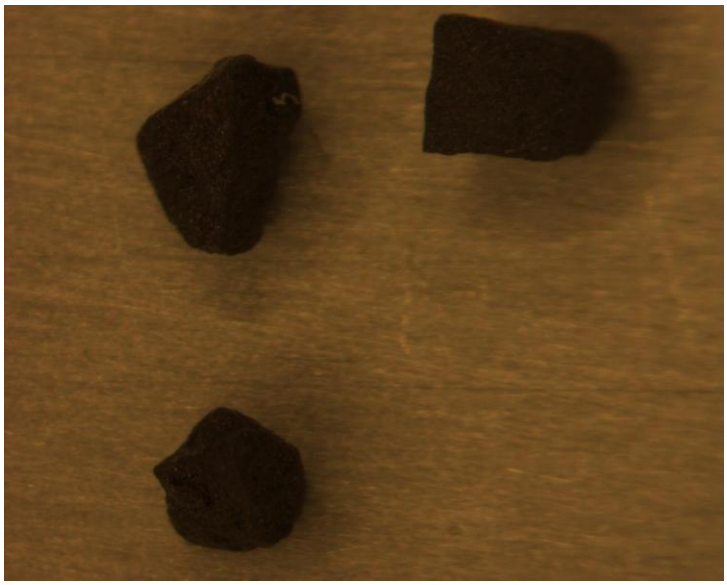

Figure 37(c). OM image of coated walnut shells at 250 °C

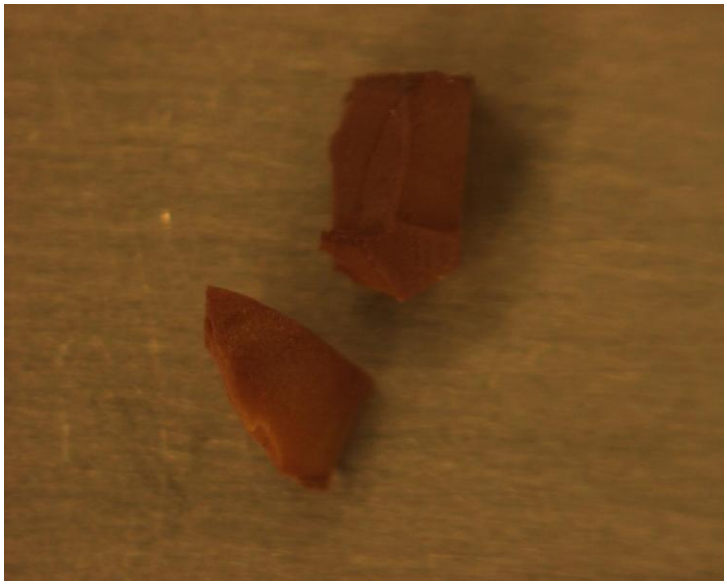

Figure 38(a). OM image of coating polymer at 225 ºC

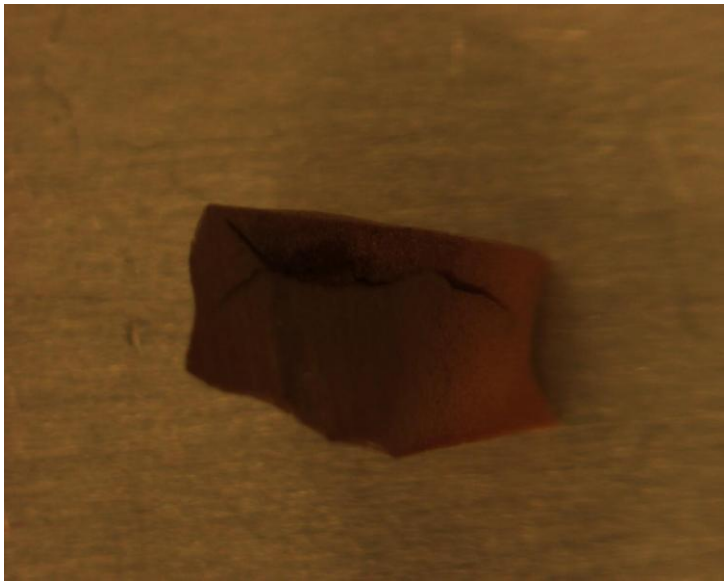

Figure 38(b). OM image of coating polymer at 250 °C

Herein it can only be concluded that charring of the particles at 80 – 160 ˚C has not occurred. In order to comment on the load carrying capacity coupled thermomechanical tests must be designed.

3.3 Flexure Testing

There is a need to develop a screening test to quickly establish the suitability of the selected specific polymer as a coating. A composite beam sample is proposed where a select volume fraction of coated particles are used with a polymer matrix to cast small 3-point bending beam samples. It is proposed that the effective property of this composite can provide a qualitative measure for comparing the effectiveness of a select specific polymer coat. In all the comparative beam samples the only parameter that is varied is the particle polymer coating. Through standardizing the test procedures and

specimen preparation procedures we propose an initial screening tool to qualitatively assess a given coated proppant system.

The testing specifications of ASTM-D790-02 [38] are used to ensure consistent dimensions and loading rates in each test. Force vs displacement plots are obtained as the primary output from which the effective elastic modulus of the specimens are calculated.

3.3.1 Specimen Preparation

A brief discussion on specimen preparation is presented below.

- Resin – DER 331, Curing agent – Ancamine – 1618 the optimum ratio for the two is 100:60 for DER 331 and Ancamine – 1618 this has been verified from the manufacturer of Ancamine – 1618.
- Coated particles – 10% by weight (resin + curing agent) used as fillers.
- Mixing and Degassing of resin and particles in above mentioned concentrations in Rotovapor (Water bath – 60 °C)
- Pour in mould and allow curing. The mould consists of two glass plates coated with mould release and separated by spacers and sealed to ensure no leakage of the liquid resin through the spacers. The spacer thickness is maintained at 3.00 mm to obtain 3 mm thick particles.
- Specimen is cured at room temperature for 7 days. Correspondence with the curing agent manufacturer indicated that a typical cure schedule is to cure at room temperature and then wait for 5-7 days for full property development. To accelerate the schedule we need to post cure by applying heat while remaining below 60C.

From the cured samples (Figure 39) specimen were cut according to the ASTM standards (test configuration is shown in Figure 40). It could be observed that we had two broadly distinct regions of concentration of walnut shell particles in the sample. The region at the bottom had a higher volume fraction and concentration of the particles. The top region of the sample had a lower concentration. We cut 3 samples each from both

these layers for samples with polymer coated particles and uncoated particles as reinforcements. The Figure 41 shows the images of two particle concentrations for coated and uncoated particles test specimen.

Uncoated particle reinforcement **Coated particle reinforcements**

Figure 39. Trial samples

L = 16.8 mm
W = 6.0 mm
T = 3.0 mm

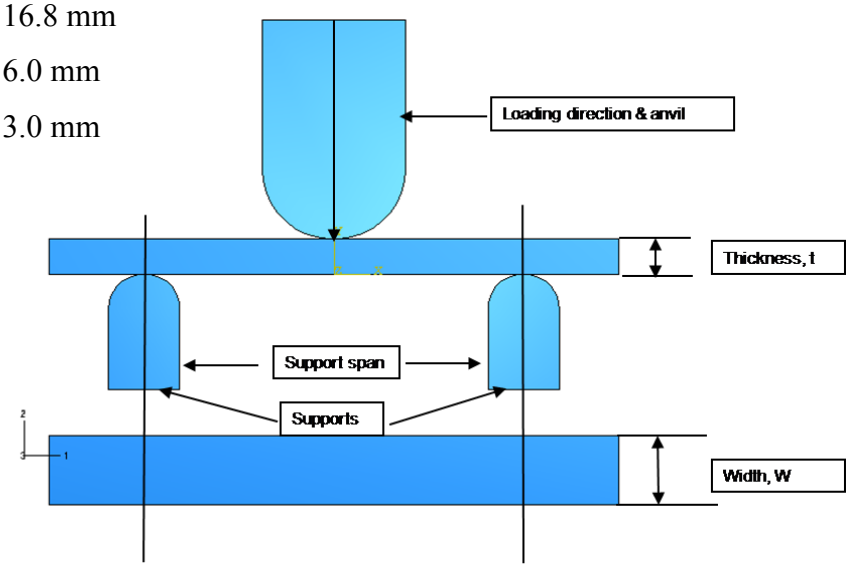

Figure 40. ASTM 3 point flexure test configuration

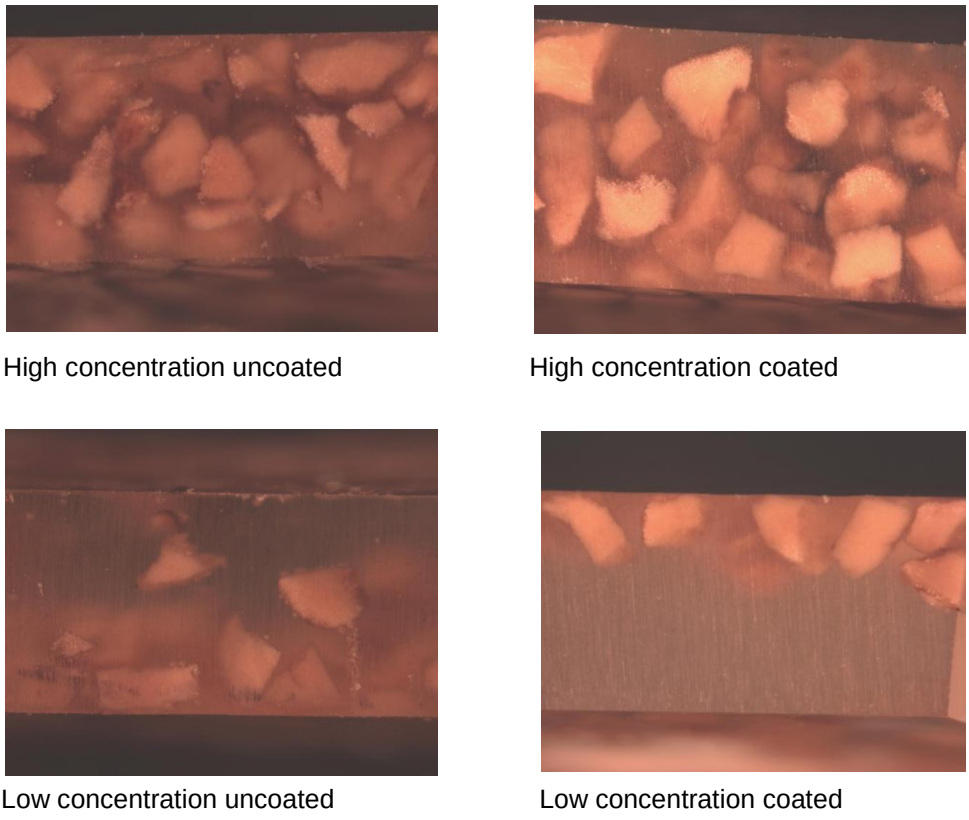

Figure 41. Concentration of coated and uncoated particles in samples from two regions

3.3.2 Test Procedure

The test bed and test setup are described below.

Horizontal Test bed (No. 18246 Tensile testing substage, Fullam Inc.) coupled with software **MTESTWindows™** (ADMET, Inc.) which interfaces with the user and regulates the test. 1000 lb Tensile load cell for load application. Loading is controlled through servo control. Direction of loading controlled through a toggle switch on the

control box. For 3 point bend test set the toggle switch to C. This setting ensures compressive loading on the sample. Specimen size is limited by test bed and bending fixture dimensions and based on the ASTM standards. The Figure 42 below displays the test setup and the loading direction.

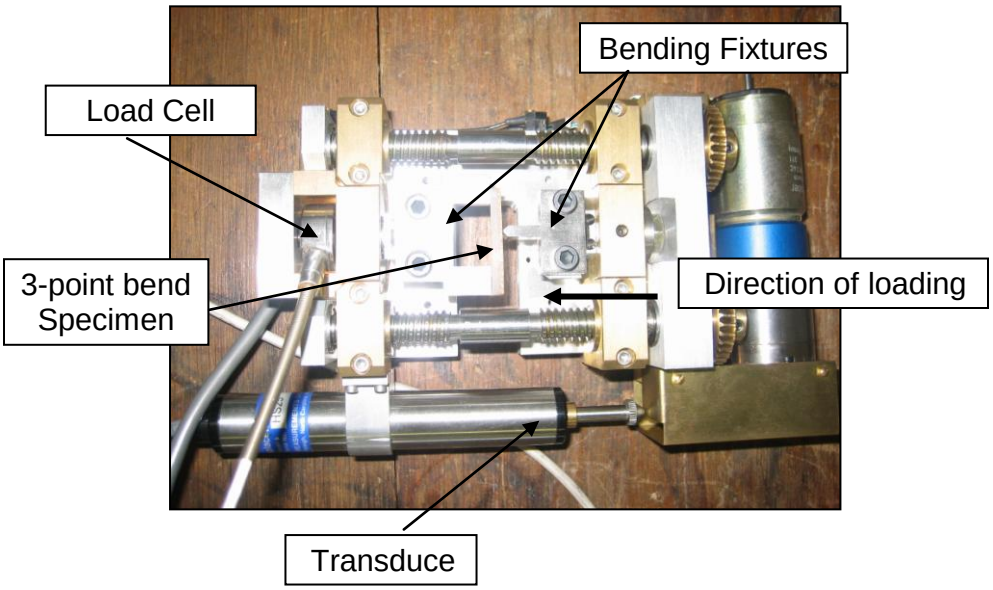

Figure 42. Test setup for 3-point bend tests

Specimen mounting and specimen sizes follow the ASTM – D790-02 standards. Set the toggle switch on the controller to C for compressive loading. Move the loading crosshead to contact the specimen. From the test setup window, define the geometry of the specimen by inputting the values of the specimen dimensions (L, W and t), specify required output to be calculated, in our case we request for the peak load and elastic modulus, select appropriate load cell (1000 lb Tensile), select the control for loading (displacement control/Force control), appropriate loading rate – 0.01 mm/sec with displacement control in our case. Start the test. Based on the above mentioned inputs

the controller provides the drive to the loading crosshead. The Transducer measures the displacement of the crosshead. The primary output is the Force-deflection curve. Based on this curve and the geometry of the specimen the output calculations for peak stress and elastic modulus are carried out using flexure equations as in ASTM – D790-02 and displayed below as equations (7 & 8).

$$\sigma_f = 3PL/2bd^2 \quad (7)$$

Where,

σ	=	Stress in the outer fibers at midpoint, MPa (psi),
P	=	Load at a given point on the load – deflection curve, N (lbf),
L	=	Support span, mm (in.),
b	=	Width of beam tested, mm (in.),
d	=	depth of beam tested, mm (in.).

$$E_B = L^3m/4bd^3 \quad (8)$$

Where,

E_B	=	modulus of elasticity in bending, MPa (psi),
L	=	suppor span, mm (in)
b	=	Width of beam tested, mm (in.),
d	=	depth of beam tested, mm (in.),
m	=	Slope of the tangent to the initial straight-line portion of the load-deflection curve, N/mm (lbf/in.) of deflection

Figure 43 shows an image of a typical output from the test bed software for uncoated low concentration specimen. It could be observed that the sample shows a non-linear behavior prior to failure. Failure occurs at a peak load of 110.6 N and the calculated elastic modulus is 1588 MPa.

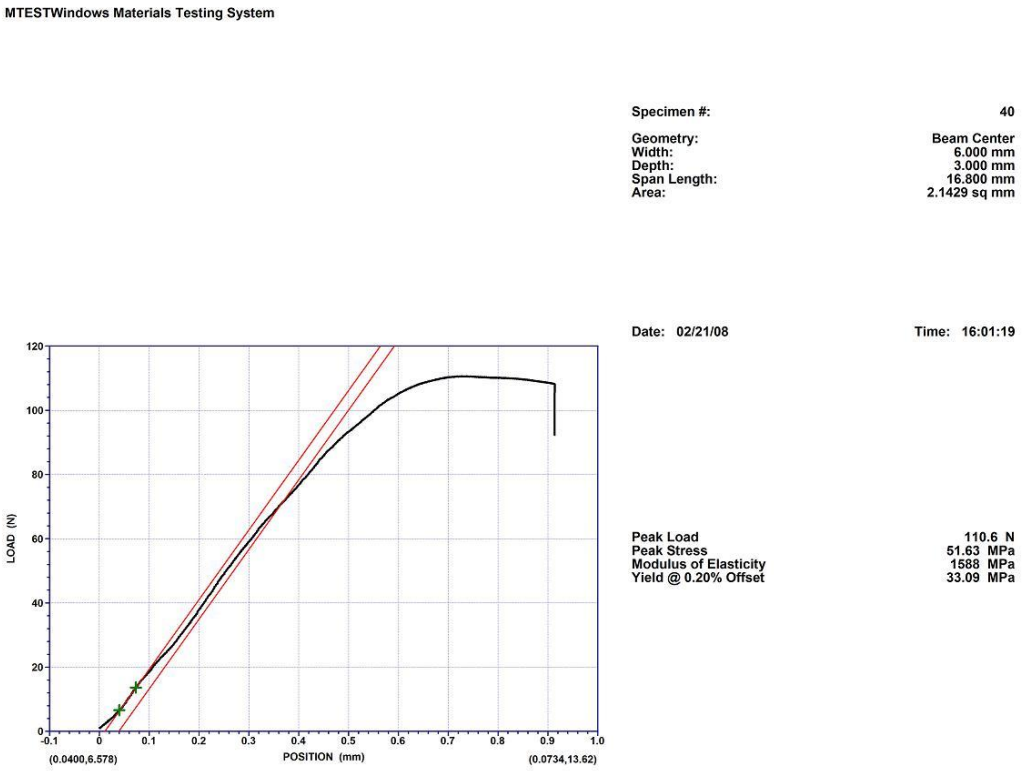

Figure 43. Image of a typical response from the 3-point flexure specimens

3.3.3 Results and Discussion

The elastic moduli of the composite specimen and the peak loads are summarized in Tables 1-2. The method of calculation has been discussed previously. Table – 1

below shows the elastic modulus for each of the specimen. Table – 2 shows the peak loads for each of the specimen.

Table 1. Elastic modulus in bending for the composite specimens

	E_{uncoat_c} (MPa)	E_{coated_c} (MPa)
Low concentration	1588	1482
	1607	1460
	1686	1481
High concentration	1877	1757
	1867	1619
	1668	1325

Table 2. Peak load in bending for the composite specimens

	F_{uncoat_c} (N)	F_{coated_c} (N)
Low concentration	110.6	75.68
	80.16	96.70
	129.0	93.36
High concentration	85.85	74.53
	81.07	48.60
	88.65	72.08

It is observed that the uncoated particles give a higher elastic modulus than the coated particles. This may be because the resin infiltrates the uncoated particles and yields an even stiffer particle. Thus it was felt that rather than comparing the uncoated and coated system we need to compare between two different polymer coating systems.

To conclude, consistent distribution of particles must be attained for proper comparison. So far only a graded distribution has been obtained. Possible improvements can be made by shaking the mould after the resin injection and the use of a less viscous polymer.

.

4 COMPUTATIONAL MODELS RESULTS AND DISCUSSION

The response of the walnut shell particles under compression are simulated using finite element analysis. Initially the Hertz model for contact between a rigid plate and a sphere is discussed. A coated particle system is introduced next adhering to the spherical idealization. The effect of particle shape on the response is introduced by considering ellipsoid models. The major axis to the minor axis radius ratio is modified to obtain a variable elliptical profile. Two and three dimensional irregularly shaped particles based on images obtained during experimentation are simulated. The irregular shaped particles are modeled to simulate the flat top, round top and cone top particle geometries as studied in the previous section of experimental studies. Both elastic and plastic responses are incorporated. The coating is introduced on the three dimensional non-uniformly shaped particle models and impact of coating on particle response is studied.

4.1 Hertz Contact Response

The Hertz Contact Theory provides the solution for two spheres in contact subjected to the normal compressive load [39]. When one of the spheres is assumed to have an infinite radius then the contact problem between a platen and a sphere as shown in Figure 44 [40] is defined. This is an acceptable first model for a spherical particle (proppant) compressed between rock faces.

The analytical solution assuming linear elastic material and small displacements is presented as below,

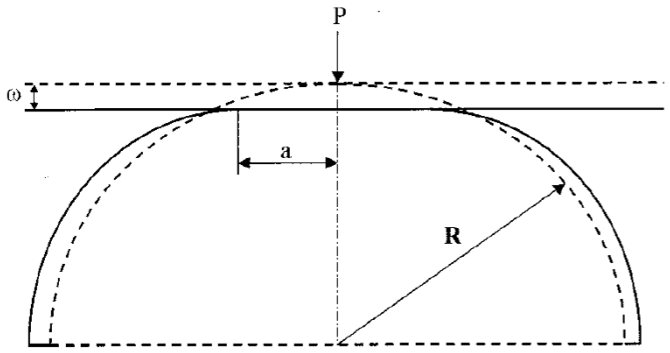

Figure 44. A deformable sphere pressed by a rigid flat [40]

$$p(r) = p\left[1-\left(\frac{r}{a}\right)^2\right]^{1/2} \tag{9}$$

$$p = \frac{2Ea}{\pi(1-\nu^2)R} \tag{10}$$

$$\omega = \frac{a^2}{R} \tag{11}$$

$$F = \frac{4}{3}E^* R^{1/2}\omega^{3/2} \tag{12}$$

Where,

P(r)	Hertzian pressure distribution over contact surface
P	Maximum pressure occuring at contact centre
a	Contact patch radius
E	Young's modulus of the sphere
ν	Poisson's ratio of the solid sphere
ω	Displacement of the sphere tip
F	Contact Force
R	Radius of the sphere

4.2 Spherical FEA Models – Hertz Contact Simulation

The compression of a spherical particle with a rigid plate is simulated through a commercial FEA package ABAQUS® - 6.4.5 CAE. Previous efforts for simulation of Hertz contact involve modeling the problem as an axis symmetric problem with load transferred from the rigid plate to the sphere through contact interaction [40-41]. A similar approach has been followed in the current FEA model.

The model uses small displacement theory and linear elastic constitutive material behavior. Axis symmetric 8 node rectangular biquadratic elements with reduced integration (CAX8R) are used to model the sphere. Total number of elements is 1632 nodes are 5053 with 2 active degrees of freedom (2 displacements) at each node. The platen is modeled as a rigid surface. A graded mesh with larger element density near the contact point is created (Figure 45). Contact interaction is defined between the rigid surface and the spherical surface to simulate the incremental loading and contact between the two surfaces. The platen is defined as the master surface and the spherical surface is defined as the slave. In ABAQUS the slave surface nodes are constrained to follow the master surface nodes. Thus a given displacement of the master surface produces an equal displacement of the slave surface node in contact with the master surface [35]. The diameter of the sphere is 0.9 mm is in accordance with the proppant dimensions which range from 0.1 to 2 mm. The elastic modulus assigned to the sphere is 1170 MPa based on the value of elastic modulus of walnut shell as mentioned in [42]. The rigid platen is assigned a modulus of 1e9 MPa. Axis symmetric boundary conditions are implemented as shown in Figure 45. The vertical face is constrained from horizontal motion and the horizontal face is constrained in the vertical direction. A load of 15 N, equivalent to ~ 6000 psi is applied through the rigid plate onto the sphere.

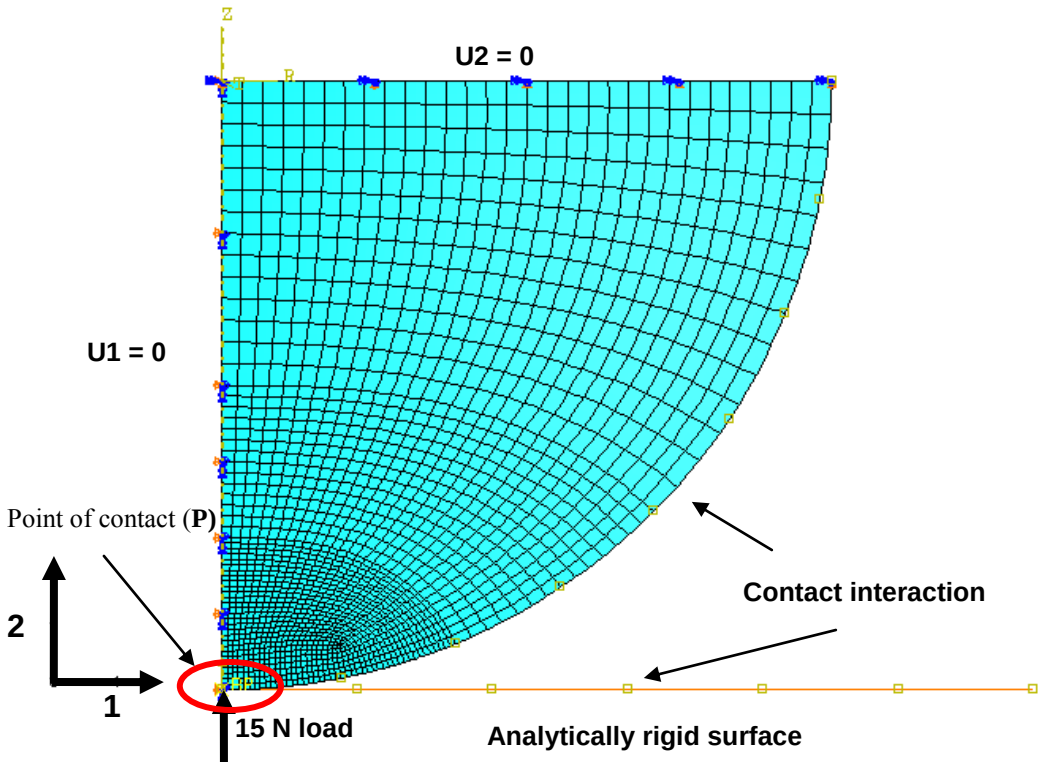

Figure 45. Mesh and boundary conditions

Results and Discussion

Displacement, Von Mises stress and the stresses in radial direction 1 and vertical 2 as per the reference co-ordinate system are presented as contour plots in Figure 46. Note that that the maximum stresses in 1-1 and 2-2 directions occur at the point of contact (here we call it as **P** and is highlighted in Figure 45) and are compressive in nature (Figure 46 (c, d)). The maximum Von Mises stress is observed to occur at a point below the surface (b). It is observed in some cases for the failure to initiate from within the solids and it can be attributed to the maximum Von Mises stress. The maximum vertical displacement is observed at the point of contact (a). Note that the sphere is

flattened in the region where the platen gets in contact with the sphere surface. This flattened surface is known as the contact patch, and the radius of this patch is known as the contact patch radius. As the sphere gets flattened a larger area contacts the rigid platen and resists further deformation.

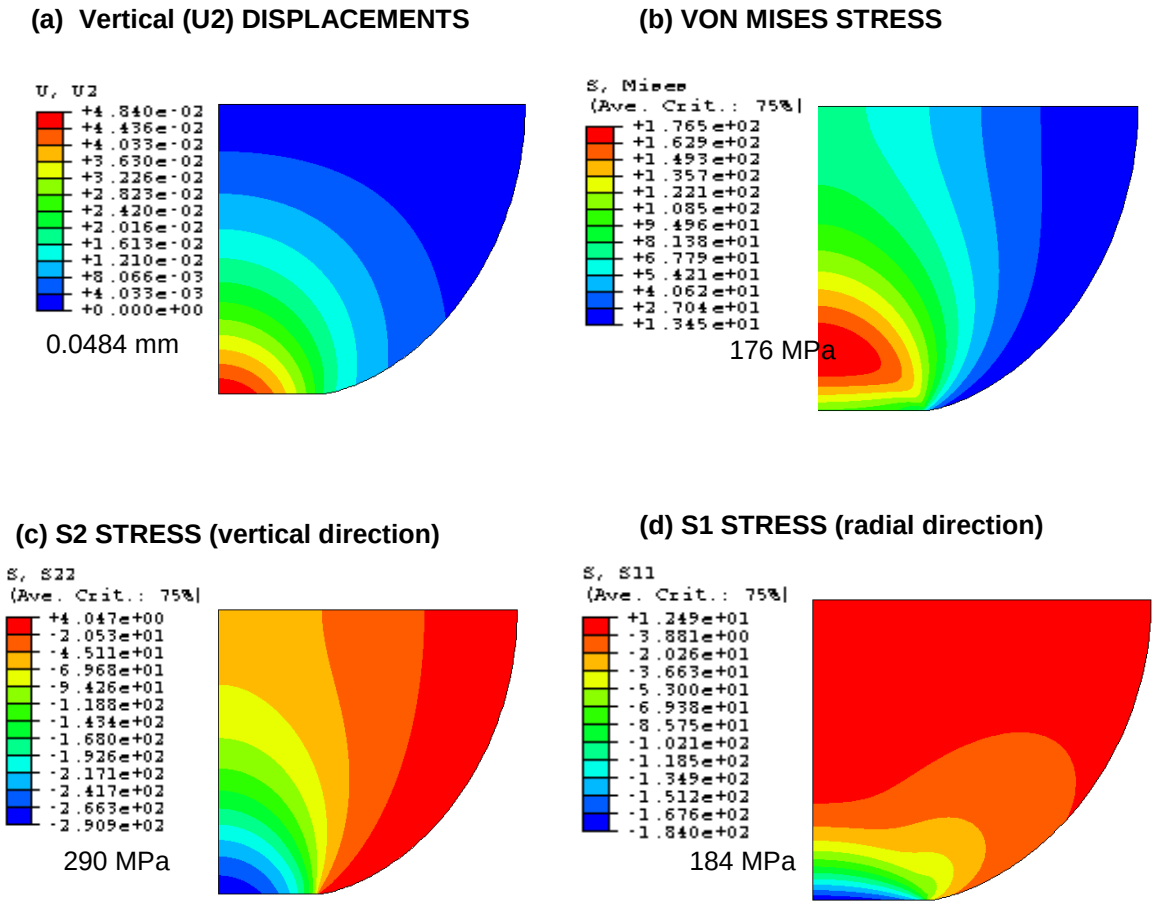

Figure 46. Contour plots for Hertz FEA model

The FEA and the Hertz results are compared on the node at the point P the point of contact in Figure 47.

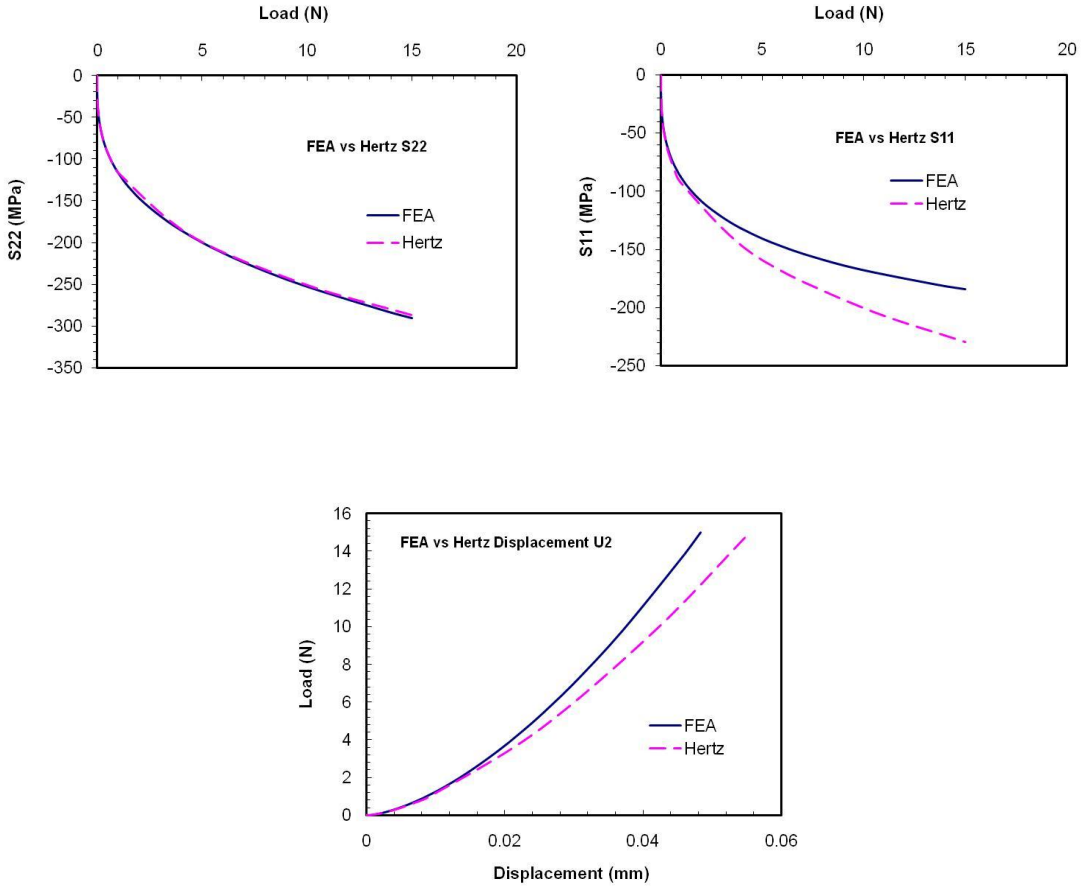

Figure 47. Comparison of FEA and Hertz solution on the node at the first point of contact on the sphere with load variation

The results of displacement U2 and stress in radial direction S11 match well in the range of lower forces ~ 2N whereas they diverge at the higher loads. The stress S22 is observed to match well at all loads.

The variation of the stresses S11, S22 and Von Mises in the particle on a straight line as a function of longitudinal (loading) axis is presented in Figure 48. Note that the S11 and S22 stresses are highest at the surface where the initial contact occurs while the maximum Von Mises stress occurs at a point below the surface. The S11 stress changes from compression to tension with increasing depth into the particle. This characteristic

is used to establish testing procedures to determine the tensile strength of brittle materials like concrete, asphalt, rock and ceramics [43].

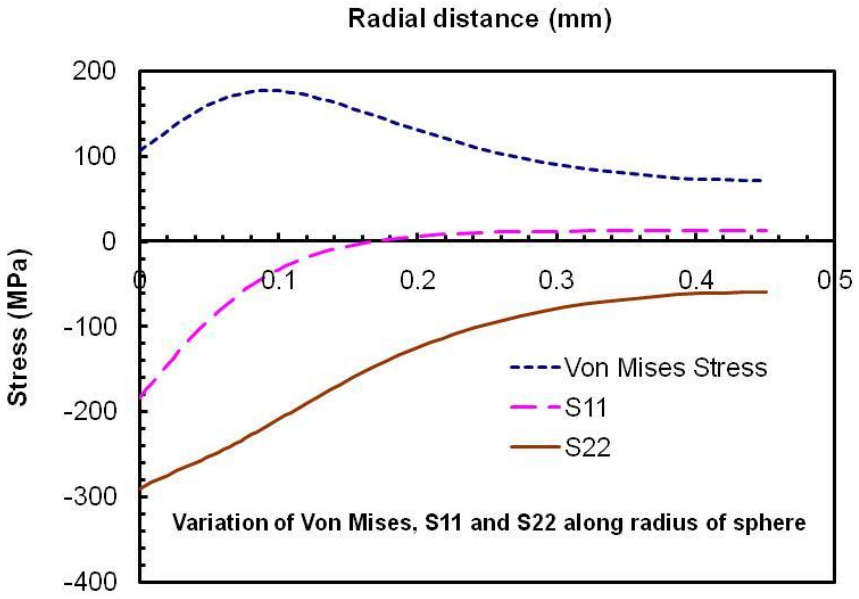

Figure 48. Variation of Von Mises, S11 and S22 on the radius of sphere from external surface to centre along loading direction (2-2)

The Hertz results and the FEA results match well at the lower range of applied forces ~ 2N. It is to be noted that at the higher range of applied loads the Hertz assumptions are violated, specifically the assumption of a high ratio of radius of circle to contact patch radius. At larger displacements as the area of contact increases the higher patch circle radius implies that a lower ratio of radius of circle to patch radius. Ideally this ratio should be in the range of 20 or above, whereas in this model it is 3 for a load of 15 N.

4.2.1 Young's Modulus Estimate From Test Data

Load vs displacement particle response data was delivered for particles in 5 groups [44]. Groups 1 to 4 were for coated particles where each group within had a different resin coat. Group 5 was for the uncoated particles. In each group 5 particles were tested. To begin with the data for group 5 was plotted in the range of 0-5% strain, 0-20% strain and 0-40% strain. The data showed a high degree of scatter and hence eventually two particles data with the lowest stiffness were chosen for further study.

The following procedure for the data analysis was adopted.

- The results were calculated for nuts with diameter D = 0.0355 in and D = 0.036 in
- The data focus on strain ranges: 0 – 5%, 0 – 20%, and 0 – 40%
- Trend line obtained for the data of nuts D = 0.0355 in and D = 0.036 in
- Slope of force Vs (displacement)3/2 curve as the estimate of E

From the plot of force Vs (displacement)$^{3/2}$ the value of elastic modulus based on the Hertz theory is obtained. These equations (13 and 14) are presented below. Here we are assuming that the particles are all spherical and undergo linear response. Poisson's ratio is assumed as 0.29.

$$P = \frac{\sqrt{2}}{3} R^{1/2} E^{*} \delta^{3/2} \tag{13}$$

Where,

P	=	Force applied
R	=	Radius of the nut
E^{*}	=	Effective modulus
δ	=	Crosshead displacement

$$E = E^{*}\left(1 - v^{2}\right) \tag{14}$$

Where,

E = Young's modulus of the granule

v = Poisson's ratio of the granule

The load vs displacement curve for all the group 5 nuts at 0-5% strain range is shown in Figure 49 to demonstrate the scatter observed. A plot for load vs displacement for particles with D=0.9017 mm and D=0.9144 mm at 40 % strain is presented in Figure 50. The force Vs (displacement)$^{3/2}$ plot for the two nuts with the data for the two nuts plotted as a single set is shown in Figure 51. This enables us to obtain a single representative curve fit for the data of the two nuts. The slope of the curve fit in figure 8 gives the representative elastic modulus of the two particles with D=0.9017 and D=0.9144 and is calculated as 3792 MPa.

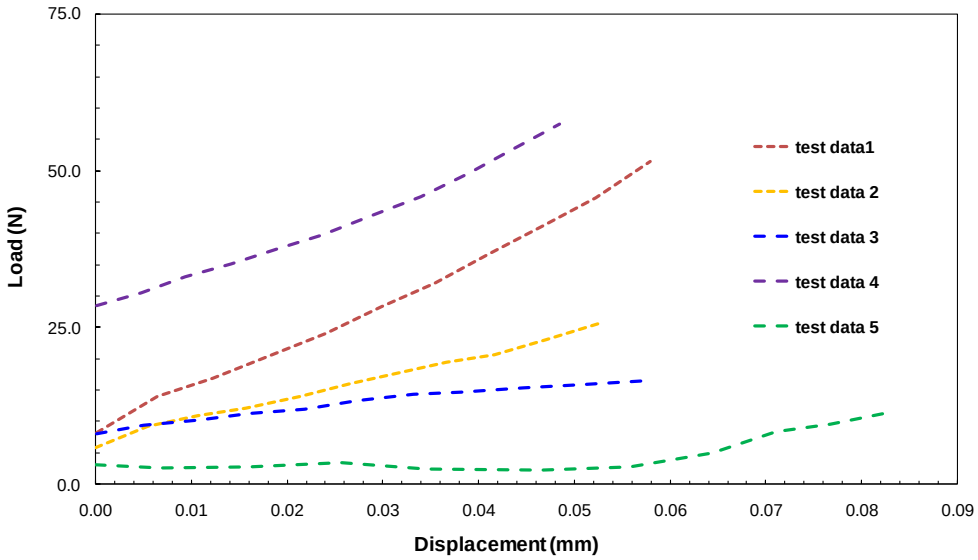

Figure 49. Force vs displacement for uncoated particles 0-5% strain range

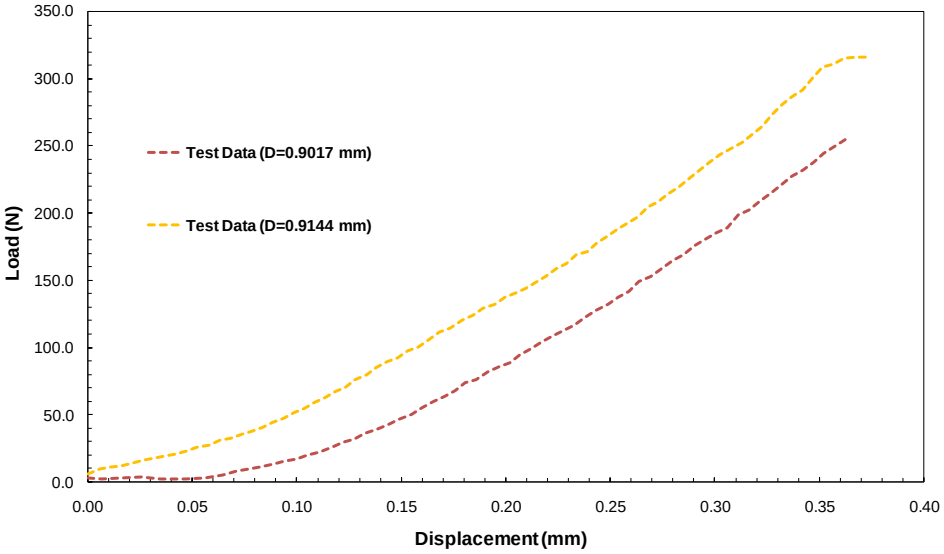

Figure 50. Force vs displacement 0-40% strain range

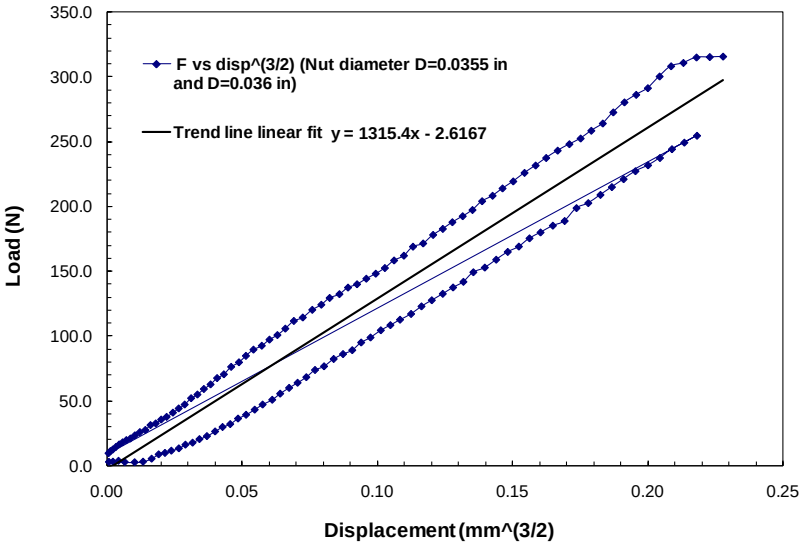

Figure 51. Force vs (displacement)$^{3/2}$ for 0-40% strain range

4.2.2 FEA Analysis Uncoated Particle – Non Linear Geometry

The geometric model for this analysis is the same as used in section 4.1. Similarly CAX8R elements (Axissymmetric quadratic 8 node elements with reduced integration and 2 displacement degrees of freedom at each node) are used. The full model has 975 elements and 3073 nodes. The test data clearly indicated that large displacements are taking place compared to the particle dimensions (~ 40% strain) hence non-linear geometry option as discussed in Appendix C is introduced.

The material and loads applied on the model are present below,

E = 3792 MPa (calculated value section 4.2.1) for uncoated particle

V = 0.29 (assumed value)

F = 308.55 N (value producing 40% strain during tests)

*NLGEOM, ON (Large displacement analysis)

Elastic material and non-linear geometry options are chosen.

The Force vs displacement response of this model is compared with the BJ Services test results [44] in Figure 52.

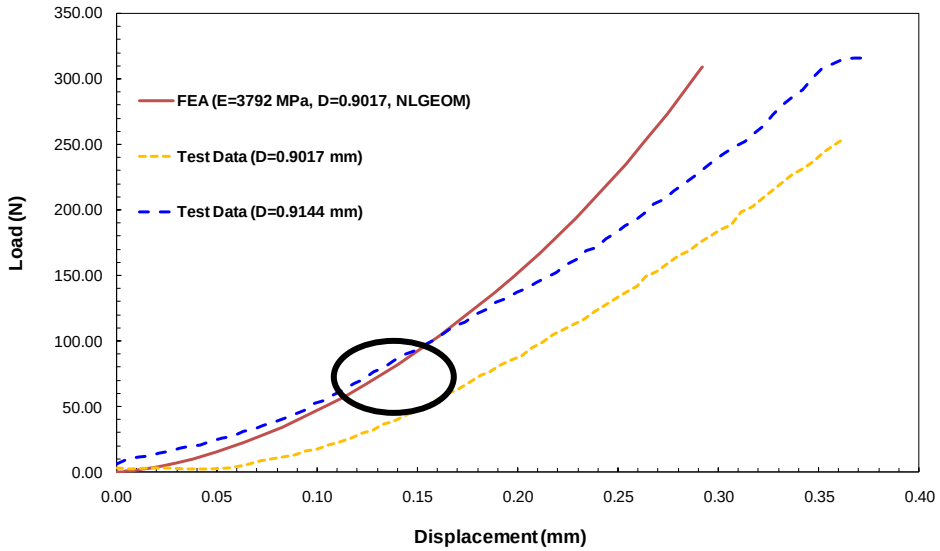

Figure 52. Force vs displacement comparison of FEA and test data

It is observed that the FEA response matches with the test result only in the range of small displacements and loads, after the load of ~100 N the FEA result starts to diverge (highlighted in Figure 52).

4.2.4 Radial Inhomogeneous Material Properties

An important goal of this research is to characterize the influence of a polymer coating on the particle response which introduces radial material inhomogeneity in the particle. Essentially three material layers emerge which include the outer most layer of polymer coat, a layer with a resin infiltration and the core of walnut shell. The layers and their properties are depicted in Figure 53.

Following factors are considered while developing this model

- Volume fraction of cavities infiltrated by the polymer – 0.25 (Assumption)
- Depth of polymer infiltration – 10% of particle dimension (Assumption)
- The effective property of infiltration space calculated by rule of mixture
  $E_{infiltration} = E_{walnut}\, C + E_{resin}\, (1\text{-}C)$ …….. (C – Volume fraction of polymer)
- $E_{infiltration}$, calculated from above, E_{walnut} from single particle test data for raw walnuts calculated previously

The properties of the raw walnut layer are as presented in section 4.2.1. The properties of the pure polymer were obtained from the website of Plenco, plastics manufacturing company [45]. Thus based on the assumed volume fraction of cavities the effective property of the polymer infiltrated layer is estimated using the rule of mixtures. The following elastic moduli of the individual material layers are adapted in the FEA model.

Raw Walnut = 6200 MPa

Pure polymer = 13000 MPa

Infiltration layer = 7900 MPa

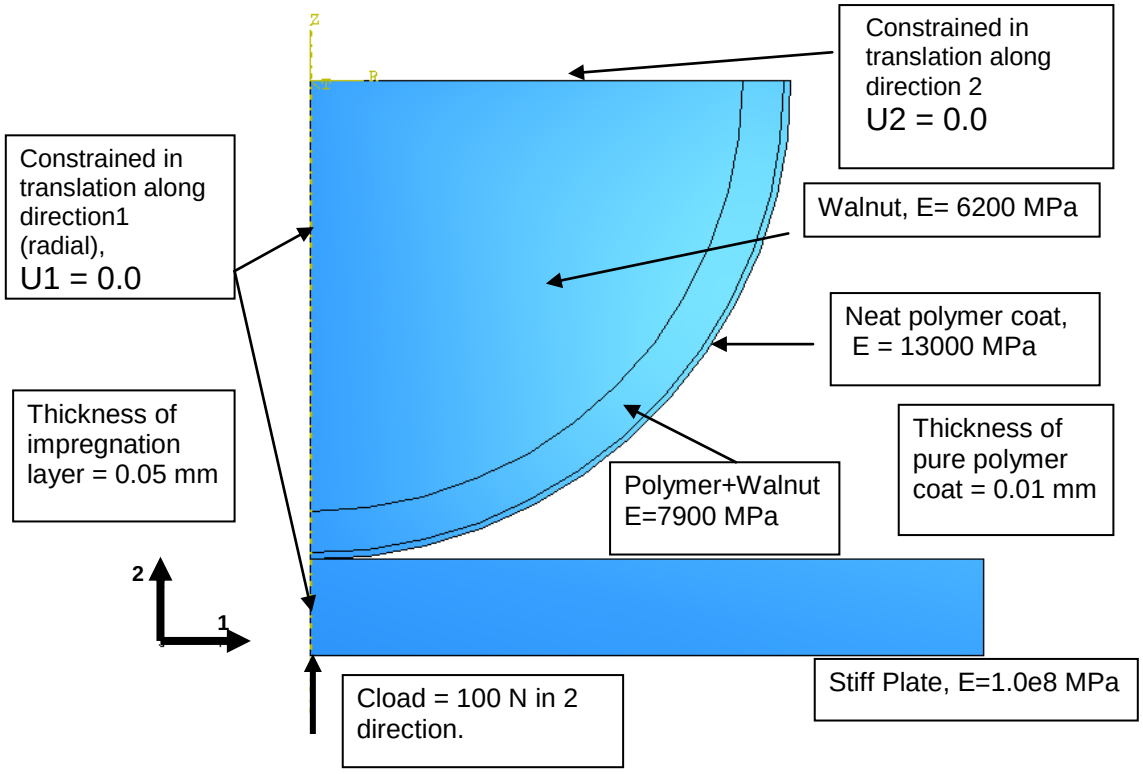

Figure 53. FEA model for the coated particle with the polymer coat modeled separately

The value of 6200 MPa is estimated from the test data of uncoated particles provided by BJ services [44].

The details of the present model are as followed and displayed in Figure 53.

Load = 100 N

Diameter of sphere = 1mm total

Infiltration distance = 0.05 mm

Linear elastic material behavior with geometric nonlinearity

Axis-symmetric 4 node quadrilateral elements CAX4R (ABAQUS®, CAE) are used for modeling. 75 elements model the pure resin region, 300 elements model the region of polymer impregnation and 2006 elements model the walnut core. Total nodes

in the model are 2470. The CAX4R elements possess 2 displacement degrees of freedom at each node.

The displacement, Von Mises stress, and the stresses in radial direction 1 and vertical direction 2, S11 and S22 are displayed in the contour plots in Figure 54.

The position of maximum stress and displacement remain as was the case of basic Hertz model (section 4.2.1). The comparison of the response of the inhomogenous FEA model with the single particle test on coated particle is shown in Figure 55.

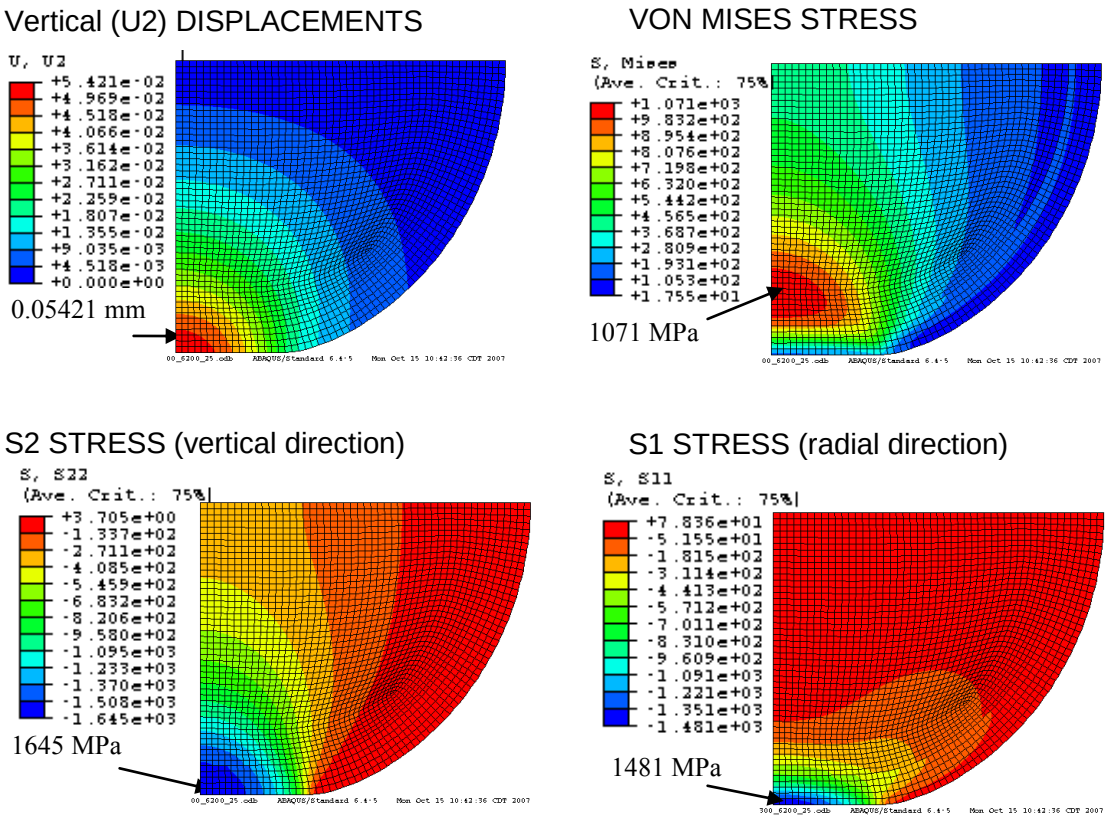

Figure 54. Contour plots for FEA model with separately modeled material layers

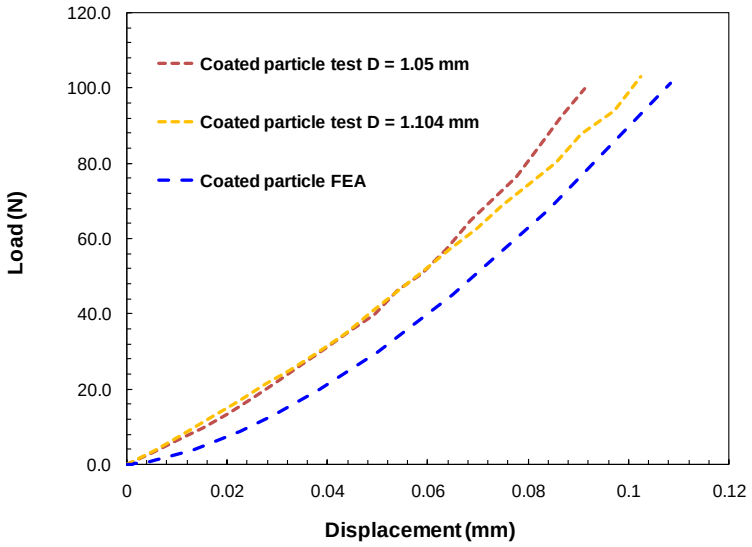

Figure 55. Force vs displacement comparison of coated FEA model with BJ test data

From the comparison of the response of the 3-layer model with the coated particle tests [44] we can back calculate the effective elastic modulus of the entire sphere as if it were a homogenous solid. Which is found to be E = 7759 MPa. From a similar exercise on the single particle, test data of the coated particles the effective elastic modulus of the particle for diameter D = 1.05 mm was calculated as 8450 MPa. Thus the inhomogeneous spherical FEA model is not able to simulate the compression response of a coated particle.

The fact that there are multitudes of different irregular shapes and variation in cellular micro structure leads to the conclusion that these effects must be considered.

4.3 Non-spherical Particles

In the previous FEA models we considered the particles to be perfectly spherical. But as can be observed in the optical microscopy images in Figure 56 and from the single particle tests conducted under optical microscope particles vary greatly in shape and are not spheres.

In order to account for the shape, iterations are carried out with an ellipsoid geometry. The major axis radius of the elliptical section is varied keeping the minor axis radius constant resulting in modification of the section from a circle to an ellipse. The 3D ellipsoid is modeled as an axis-symmetric section using CAX4R axis-symmetric elements. This is followed by modeling particles based on the optical images (i.e. irregular geometry) both elastic and inelastic material property definitions are incorporated. Finally coating is introduced on these irregular shape models to study their compression response.

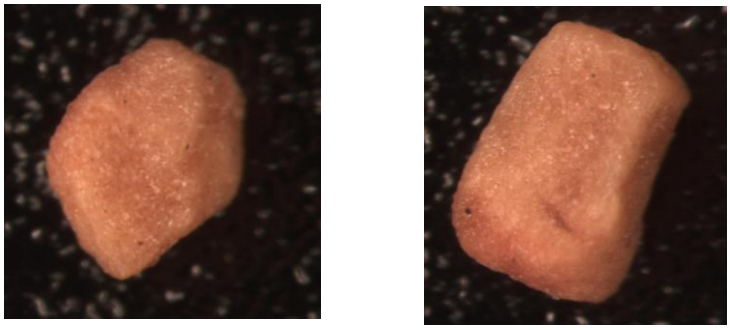

Figure 56. Images of coated particle under optical microscope

4.3.1 Ellipsoid Profile – Axisymmetric Model

The basic model for the elliptical profile with the assigned material properties and co-ordinate system is displayed in Figure 57. In the parametric studies, boundary conditions and applied loads and material properties remain identical, however the ratio of the radii (b/a) is varied to closely observe the effect of the geometry variation. The ratio is varied from 0.5 to 1 (for sphere).

Linear quadrilateral elements (CAX4R) with, 4 nodes and reduced integration with 2 displacement degrees of freedom at each node in ABAQUS 6.4.5 CAE package are selected. The number of elements depend on the (b/a) ratio and range from 402 elements to 761 elements. Again in this case also nonlinear geometry analysis option is incorporated with linear elastic constitutive material model.

The load vs. displacement response of the studies with varying (b/a) ratio is represented in Figure 58. It can be observed that the response tends to stiffen with variation of ratio from 1 to 0.5. This is attributed to the increase in initial surface area of contact with the geometry variation from sphere to ellipse thus adding added resistance to deformation. The results signify the effect of profile on the particle response validating our premise that the scatter in compression test data may indeed be due to a scatter in the particle profiles.

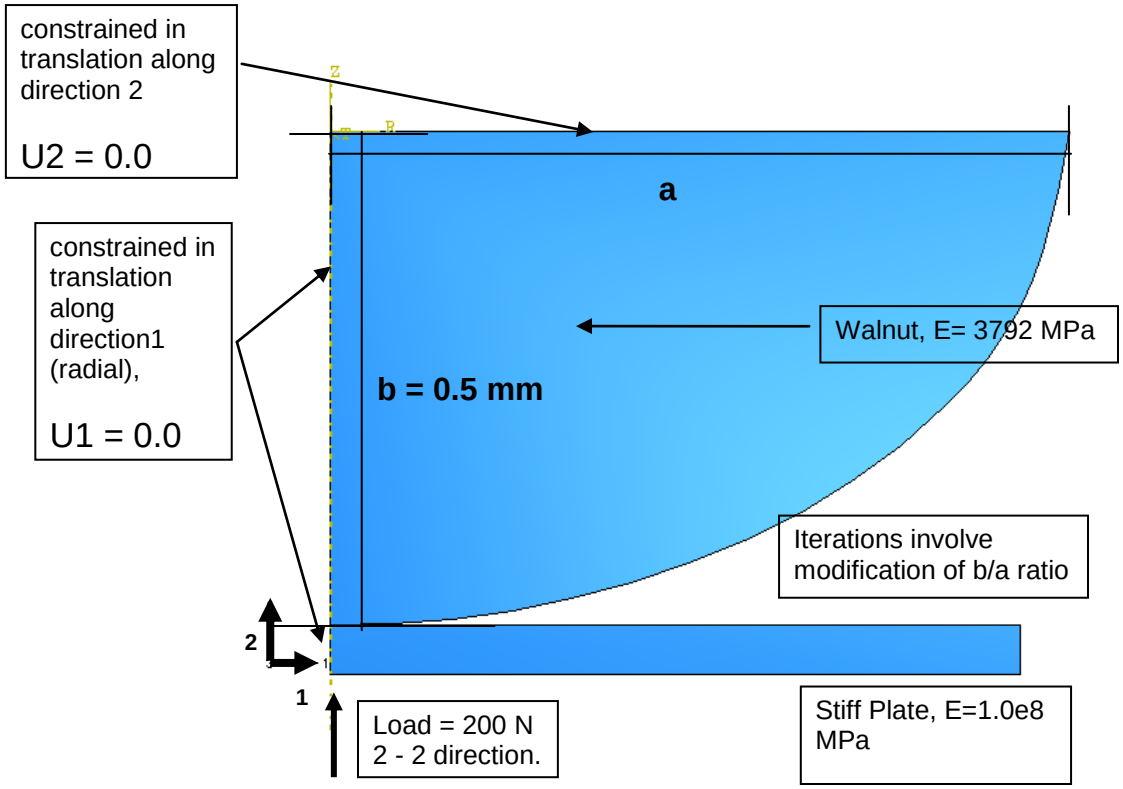

Figure 57. Materials and boundary conditions for ellipsoid model iterations

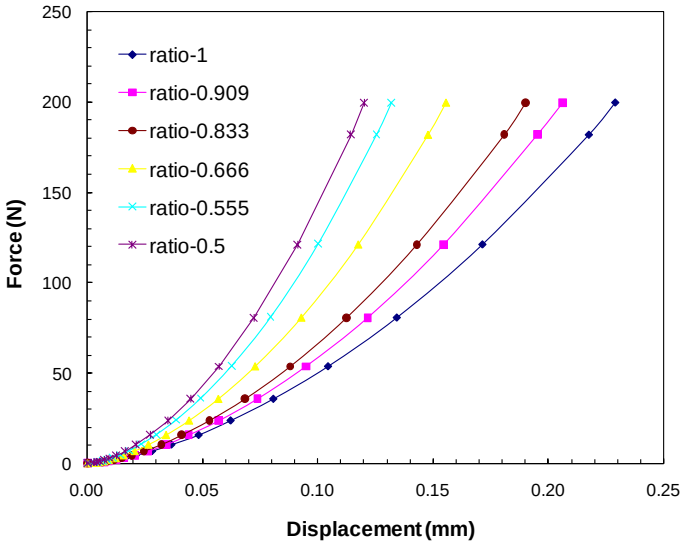

Figure 58. Force vs displacement comparison for ellipsoid iterations

4.3.2 2D and 3D Irregular Shape Particle Models

Since the OM and ESEM images confirmed that these particles are far from any idealized shape, realistic shapes guided by the images are selected to be represented by 3D tetrahedral C3D4 elements with 3 displacement degrees of freedom at each node. Static analysis with nonlinear geometry and linear material option is selected to study the displacement, strain and stresses generated under compression. The elastic moduli for the uncoated walnut and the platens were assigned as 3700 MPa and 100 GPa respectively. The platens are modeled as rigid surfaces. Contact interaction is defined between the platens and the walnut shell particle models to transmit the incremental compressive load to the particle. The platen is defined as the master surface while the particle surface is the slave. In ABAQUS the contact definition implies that the master node constrains the slave node to undergo an equal displacement in the direction of the master surface displacement [35].

The three 3D FEA models are displayed in Figures 59 - 61, FT1 is based on the flat top particle and CT1 is based on the cone top particle type while model RT1 is based on the round top type. Differences in the profile are highlighted through the two different views. The dimensions of the models based on the test particles are ~ 1.5 mm X 1.2 mm X 1 mm. A fine mesh is maintained in the region of initial contact with the platens and graded outwards to economize computational resources. The contact region is highlighted in the Figures 59 - 61. The horizontal lines represent the platens and the arrow indicates the loading direction. The details of the three models are presented in Table 3. 100 N load is applied on the particles and results observed at this load.

Table 3. Details of 3D FEA models

Model	Element type	Total elements	Nodal DOF*	Total nodes
FT1	C3D4	21521	U1, U2, U3	9941
RT1	C3D4	32591	U1, U2, U3	9415
CT1	C3D4	23723	U1, U2, U3	10419

*DOF: Degrees of freedom at each node

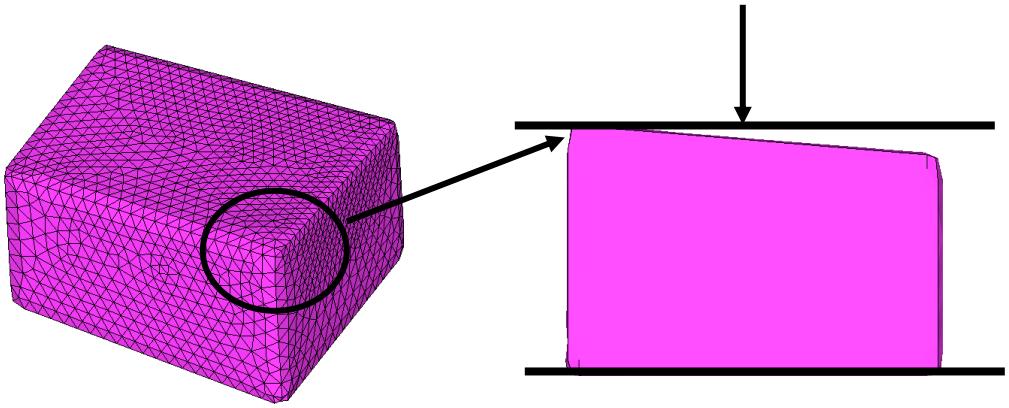

Figure 59. 3D model FT1 (flat top representation)

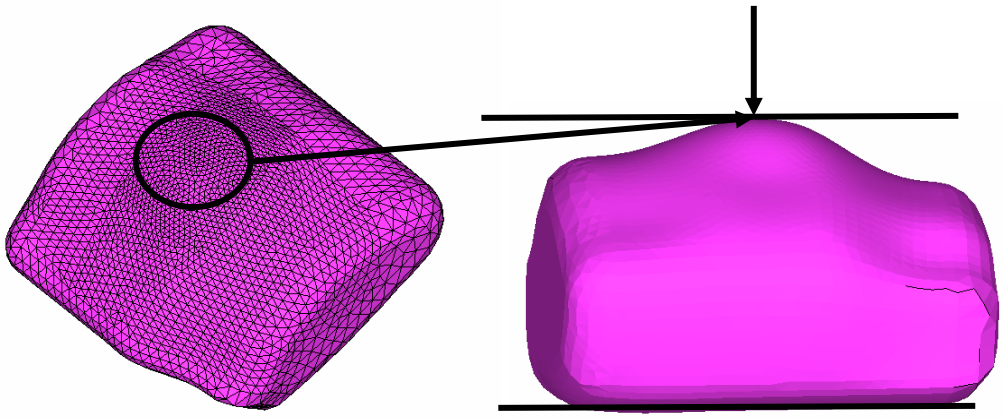

Figure 60. 3D model RT1 (round top representation)

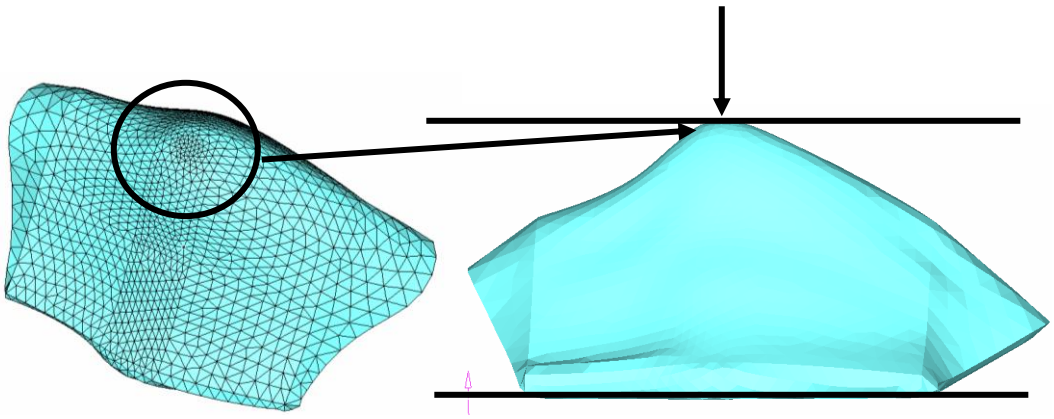

Figure 61. 3D model CT1 (cone top representation)

The vertical platen displacements measured at the load application point on the rigid platen surface at 100 N load are 0.0731, 0.09 mm and 0.106 mm for models FT1, RT1 and CT1 respectively as is highlighted in Figure 62. The maximum platen displacement is observed in the cone top representation and the least in the flat top representation. This is in accordance with the experimental results of single particle compression tests with geometrical classification of the particles, though it is to be noted that the differences are minor compared to the experimental results. It is also to be noted that the maximum displacements predicted are less compared to the experimental results and the elastic material model gives a highly stiff response. It can also be said that even at a load of 100 N the small value of maximum displacement does not enable the full impact of shape variation on the particle response to be captured in the elastic FEA model. The comparison of the 3D elastic FEA results with the single particle compression test on uncoated particles is presented in the figure on page 77.

The maximum Von Mises stress is observed at an element in the interior of the model along the loading direction and the values are 556 MPa, 794 MPa and 1192 MPa for the FT1, RT1 and CT1 models respectively. These values are large and it can be assumed that the particles at this load will definitely undergo plastic deformation.

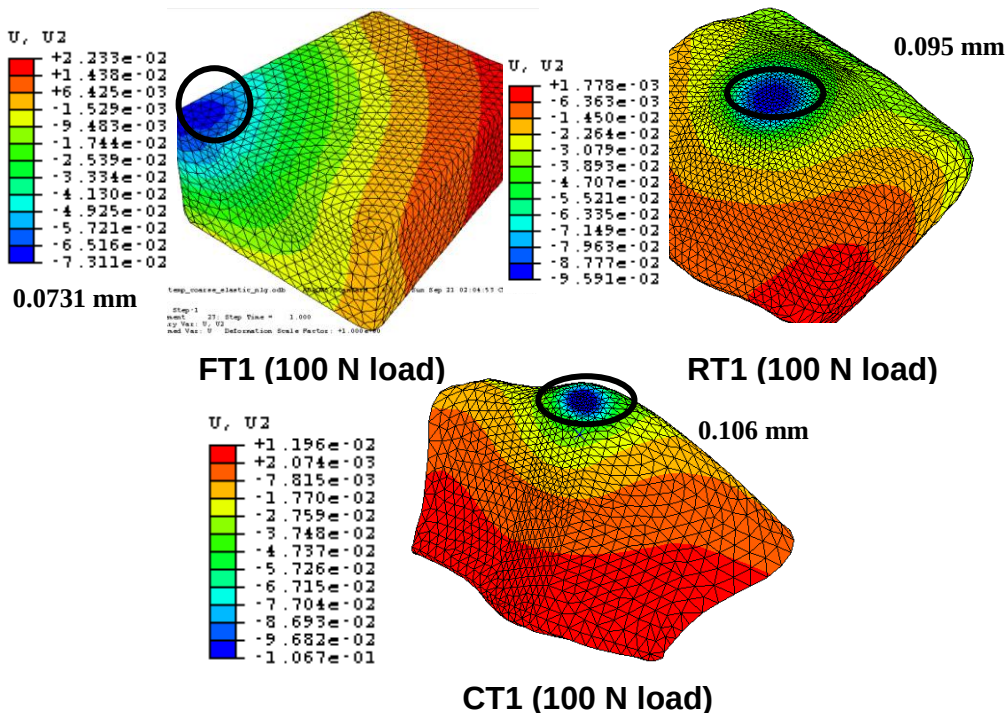

Figure 62. Contour plot for maximum vertical displacement at 100 N load for 3D models FT1, RT1 and CT1

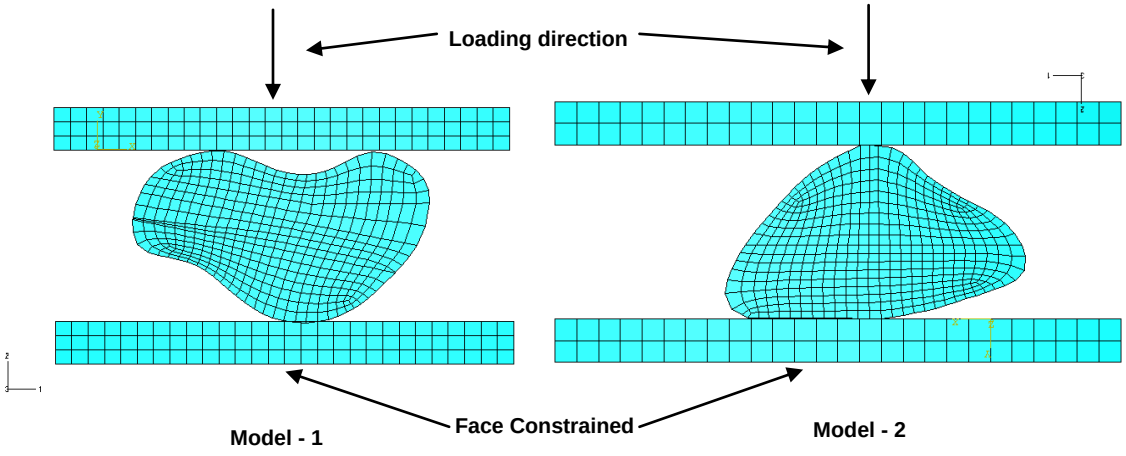

Figure 63. 2D plane strain FEA models for different particle cross-sections

2D Representation

Plane strain assumption which translates to two dimensional representations was studied with the models of Figure 63. Advantage of a 2D model is simplicity of modeling and economy of computational resources, with the disadvantage of the loss of details in the third dimension. Model -1 comprises of 460 nodes and 464 CPE4R (4 node linear quadrilateral 2D solid plane strain element with reduced integration and 2 active displacement degrees of freedom). Model -2 comprises of 475 nodes and 440 CPE4R elements. The models are based on the images of the test particles. The dimensions of each of the models are ~ 1.4 mm X 1 mm X 0.8 mm. The material properties and loads on the models remain the same as in the case of 3D models. The analysis is defined as nonlinear geometry with linear elastic material model. The contour plots for vertical displacement for the two models are displayed in Figure 64. Model -1 has a maximum displacement of 0.06967 mm at 100 N loading while model – 2 has 0.06496 mm. The comparison plot for the response of 2D elastic FEA model with the single particle compression tests on the randomly selected uncoated particles is presented in Figure 65. It is observed that the 2D elastic FEA model gives a much stiffer response compared to the single particle compression test response. Also the difference in the response of the two 2D models is very less; hence the 2D elastic models are also not able to capture the effects of shape variation effectively.

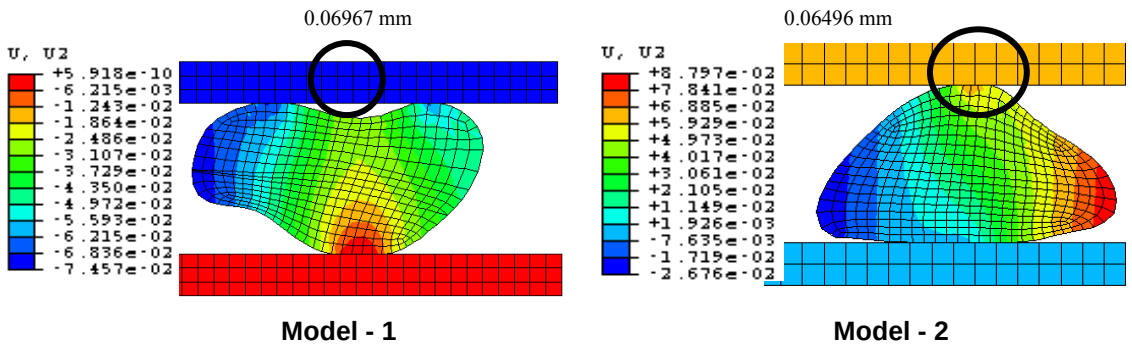

Figure 64. Contour plot for vertical displacement 2D plane strain elements

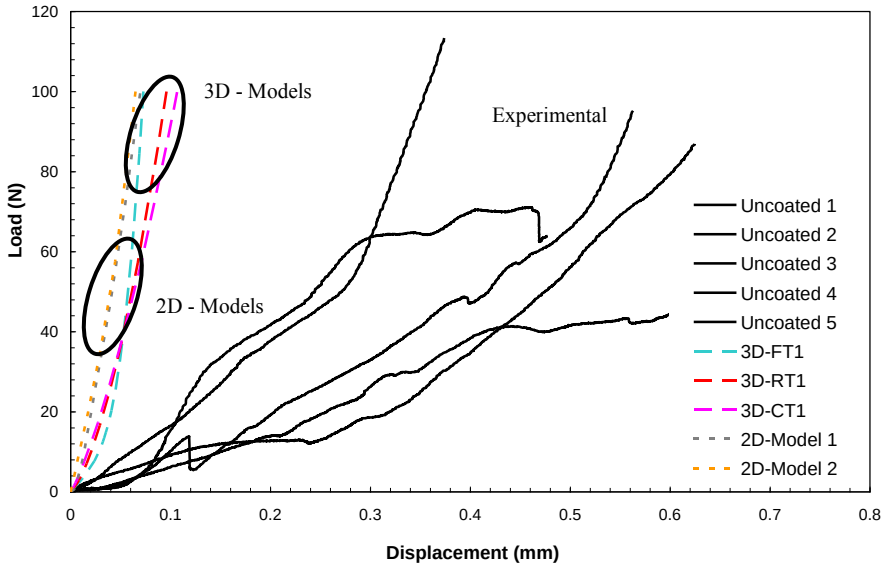

Figure 65. Comparison of load vs displacement response of the elastic 2D and 3D FEA models with the single particle compression tests on uncoated particles

It is observed that both the 3D and 2D models with elastic material and nonlinear geometry are considerably stiffer in comparison to the experiments and thus requires further assessment and definition of nonlinear behavior. Note that the 2D and 3D response have not been compared with each other but are compared with the experimental results only. A comparison between 2D and 3D is possible only when both of these have the same section dimensions and shape which is not the case with the current analysis. The two classes of FEA models can be compared with the experimental results since a wide range of shape variation among the test particles occurs routinely.

4.3.3 Inelastic Material Response

By referring to the experiments in section 3.1.4 we determined the true stress vs strain curve for the non-linear material response of walnut shell. The nonlinear response is assumed to be elastic – plastic with isotropic hardening. In ABAQUS this response is modeled as classical metal plasticity (Appendix D), the governing equation (15) for this response is presented below. Here K and n are constants dependent on material and any prior treatment (strain hardening, heat treatments etc) carried out on it [46]. The stress strain data from the true stress vs true strain curve for the cuboid walnut particles are used as input into ABAQUS to model the elastic-plastic isotropic hardening response of the uncoated non-uniformly shaped particles.

$$\sigma_{true} = K\varepsilon_{true}^{n} \tag{15}$$

The nominal stress vs nominal strain and true stress vs true strain plot is presented in Figure 35 in section 3.1.4. In the load vs displacement plots of the walnut shell cuboid compression (Figure 34 section 3.1.4) it is observed that up to the point of failure the plots show linear behavior. It is assumed that the particles undergo non-recoverable deformation at a very low stress and the linear behavior observed is a hardening response. Similar conclusions have been drawn for the plastic stress vs strain response of plant tissues by Niklas [47]. In our FEA models we trigger the onset of plasticity at a very early stage at a low stress of ~ 5 MPa. 3D models FT1, RT1 and CT1 are solved using the non-linear material data. Again the analysis is defined as geometrically nonlinear to account for the large displacements.

The vertical displacement of the platens measured at the load application point on the platens are 0.329 mm, 0.477 mm and 0.6823 mm respectively for FT1, RT1 and CT1 models at 100 N load. The contour plots for the maximum displacement are presented in Figure 66 (a, b & c). Note at the significant differences in the maximum

displacements for the flat top, round top and cone top models. The flat top provides the stiffest response followed by round top and cone top; this is in accordance with the observations from the single particle tests on geometrically classified particles. It can be argued that with the larger displacements of the platens a greater surface area of the particle contacts the platen; the area contacting the platens is dependent on the surface profile with the maximum area being with flat top particles and least with the cone top particles. A greater surface area in contact would apply a greater resistance to the platen displacement and hence a stiffer response of the particle. The elastic FEA model did not undergo significant deformation for the surface profile to exert any influence on the compression response and could be a probable reason for the very small differences in the displacements for the three elastic models. The comparison of load vs displacement response of the FEA models with the single particle tests on randomly selected uncoated particles is presented in Figure 67.

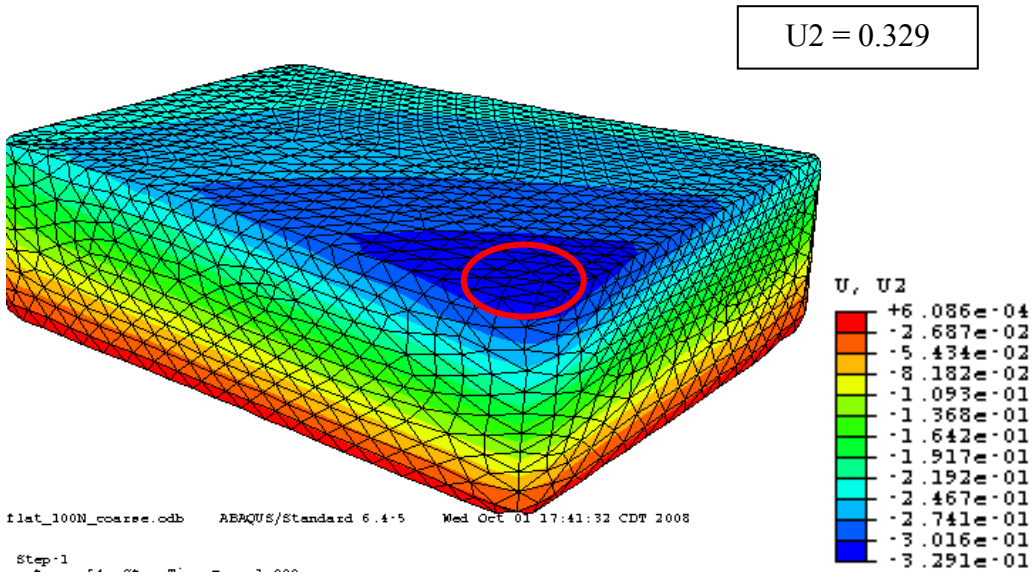

Figure 66(a). Vertical displacement contour for 3D plastic model at 100 N - FT1 model

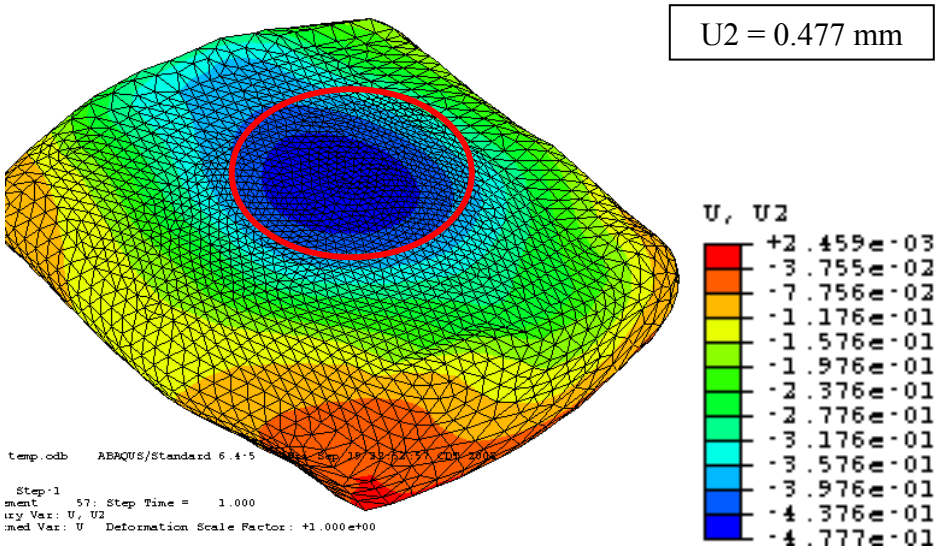

Figure 66(b). Vertical displacement contour for 3D plastic model at 100 N - RT1 model

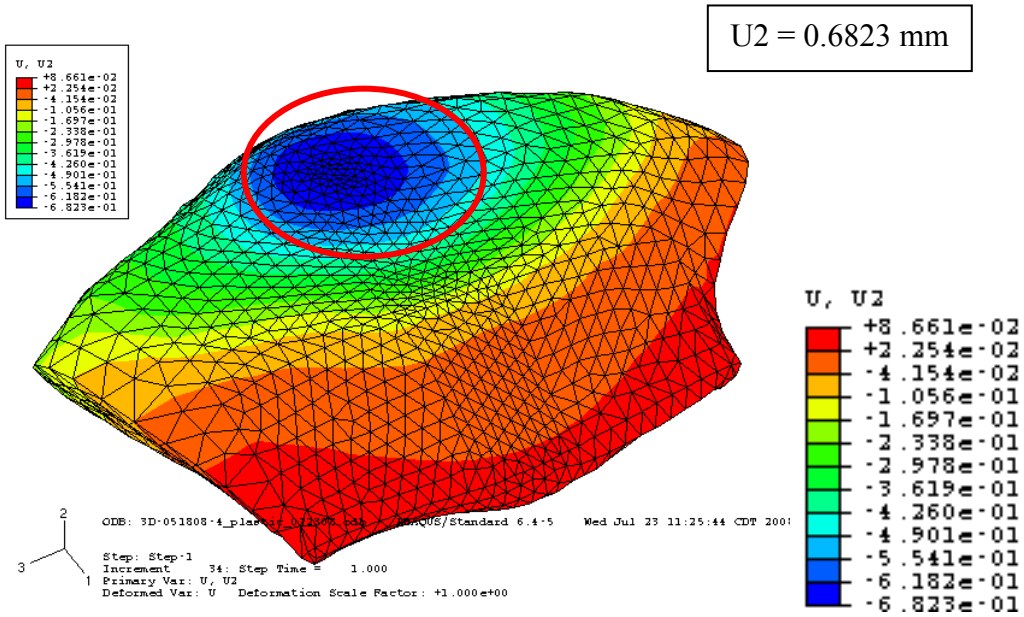

Figure 66(c). Vertical displacement contour for 3D plastic model at 100 N - CT1 model

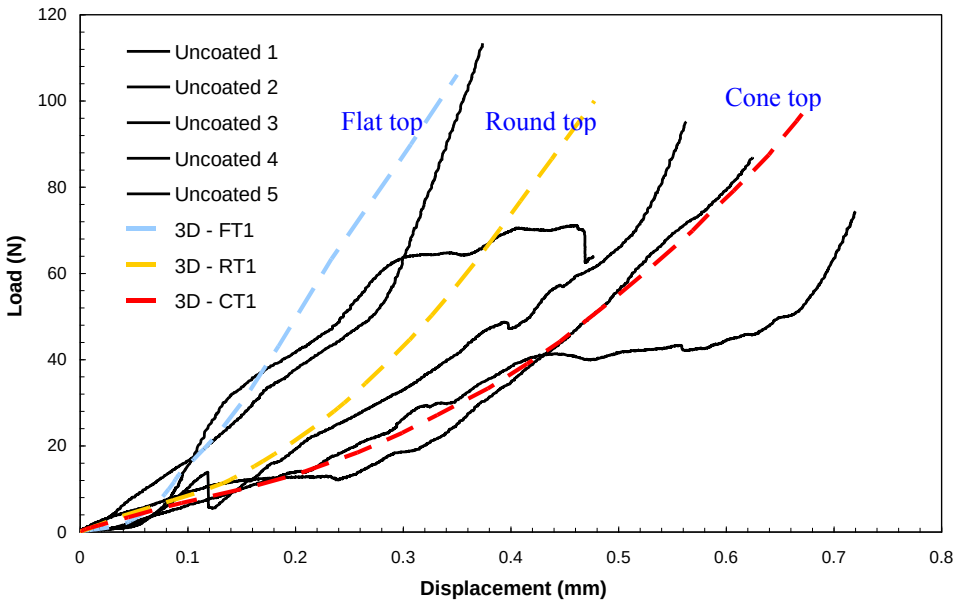

Figure 67. Comparison of load vs displacement response between 3D plastic FEA models FT1, RT1 and CT1 with single particle compression tests on uncoated particles

From the contour plots for displacements and the plot in Figure 67, it can be concluded that the inelastic material definition is able to simulate the compression response much more effectively compared to the elastic material definition. The significance of shape on the particle response is also highlighted through the implementation of nonlinear material definition.

4.3.4 Influence of Polymer Coat

Coated particles are simulated by introducing a layer of polymer coat on the irregular shaped 3D models (FT1, RT1 and CT1) with inelastic material properties. We assume a polymer coating thickness of ~ 10 μm and no infiltration. The FEA model FT1 with the polymer coat is shown in Figure 68.

The walnut shell material property is same as in section 3.1.4 and 4.3.3. The polymer is assumed to be a phenolic resin. The elastic modulus and the tensile strength of the polymer are obtained from literature [48]. The polymer coat is also assumed to possess nonlinear (plastic isotropic hardening) behavior. The hardening slope of polymer is assumed to be equivalent to the walnut shell cuboid test-3 response and is not based on any experimental or literary evidence. The true stress vs true strain response is used to model the nonlinear behavior. The nominal stress vs nominal strain and true stress vs true strain curves for the walnut shell and polymer coating are shown in Figure 69.

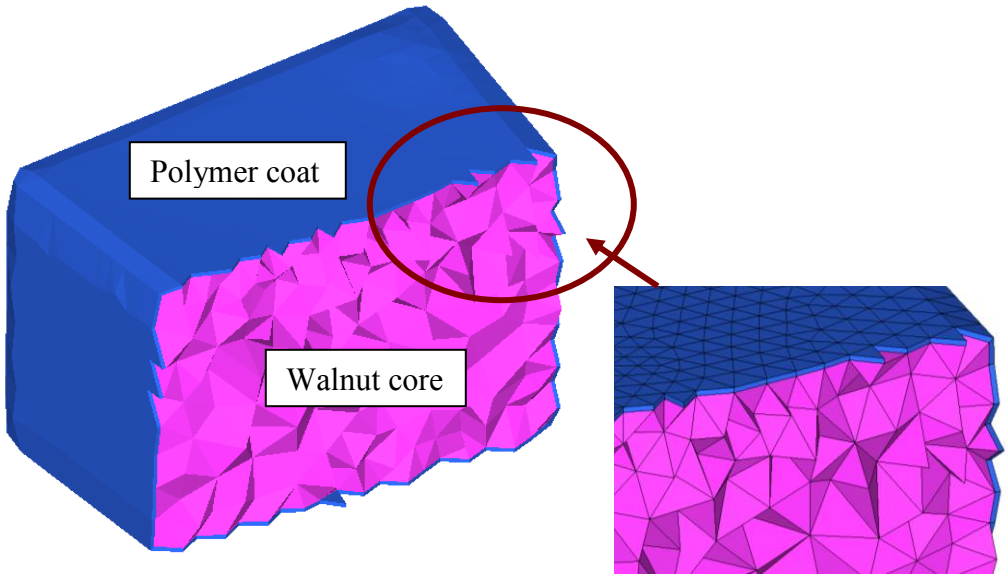

Figure 68. 3D FEA model with polymer coating (FT1 model)

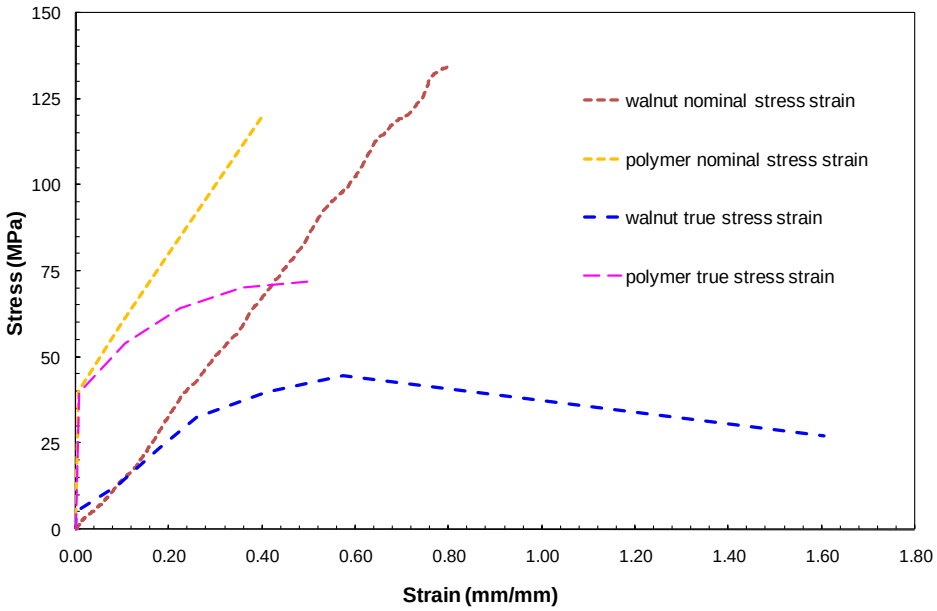

Figure 69. Nominal stress vs nominal strain and true stress vs true strain curves for walnut shell and coating polymer

The boundary conditions remain same as with the elastic models with irregular shape. The analysis is nonlinear geometry with inelastic material properties. The comparison of the load vs displacement curves of the three coated FEA models (CFT1 (coated flat top), CRT1 (coated round top) and CCT1 (coated cone top)) with the single particle compression tests on coated particles are presented in Figure 70. The displacements are measured at the load application point on the rigid platens. It is observed that the response from CRT1 and CCT1 models at lower loads ~ 25 N diverges away from the experimental results. The CFT1 model is able to give a close approximation of the experimental results.

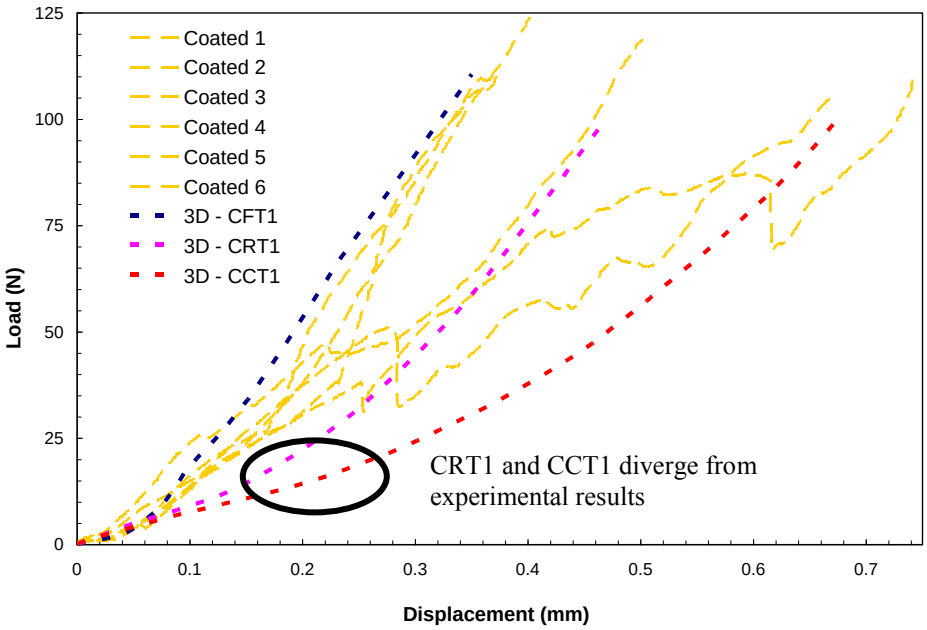

Figure 70. Comparison of load vs displacement response from the coated FEA models CFT1, CRT1 and CCT1 with the single particle tests on coated particles

To study the effectiveness of the resin coat in improving the stiffness of the particles displacements in the walnut core of the coated particles were measured at a point just underneath the first contact point on the coating and on the coat walnut interface. The comparison of the response of walnut shell particles with and without coating is presented in Figure 71. It is observed that addition of resin coat introduces stiffening in the response of the walnut shell, but the increase is marginal. The values of maximum displacements at 100 N are compared in Table 4.

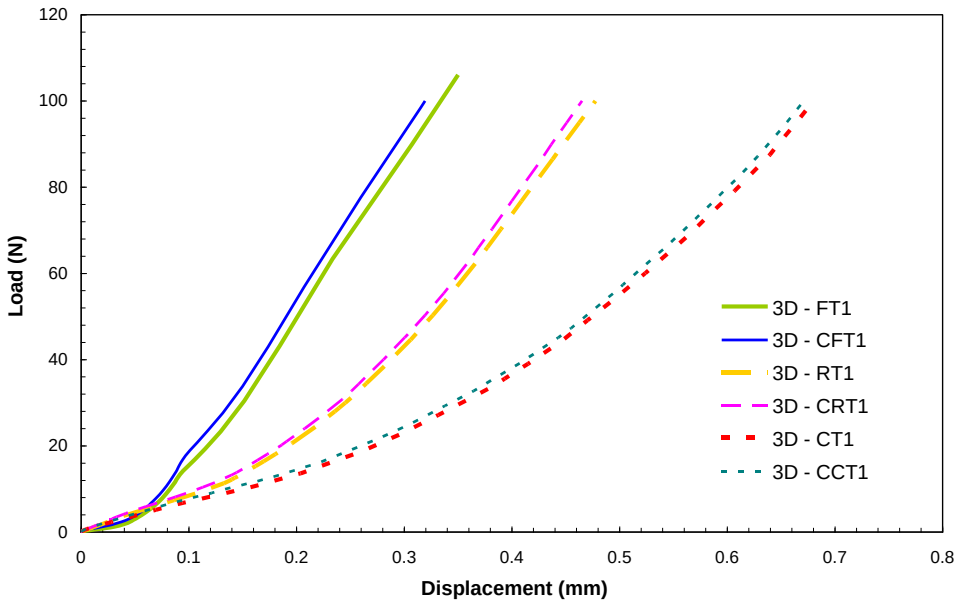

Figure 71. Comparison of load vs displacement response of walnut particle when coated and uncoated

Table 4. Comparison of maximum displacements (mm) in coated and uncoated walnut shell particles at 100N load

	Flat top	**Round top**	**Cone top**
Uncoated particle	0.329	0.477	0.6823
Coated particle	0.315	0.462	0.67

The contour plots comparing the Von Mises, vertical displacement, LE11, LE22 and LE33 for the walnut region of the coated flat top particle and the uncoated plastically deformed flat top particle (CFT1 and FT1) are presented in Figures 72-76.

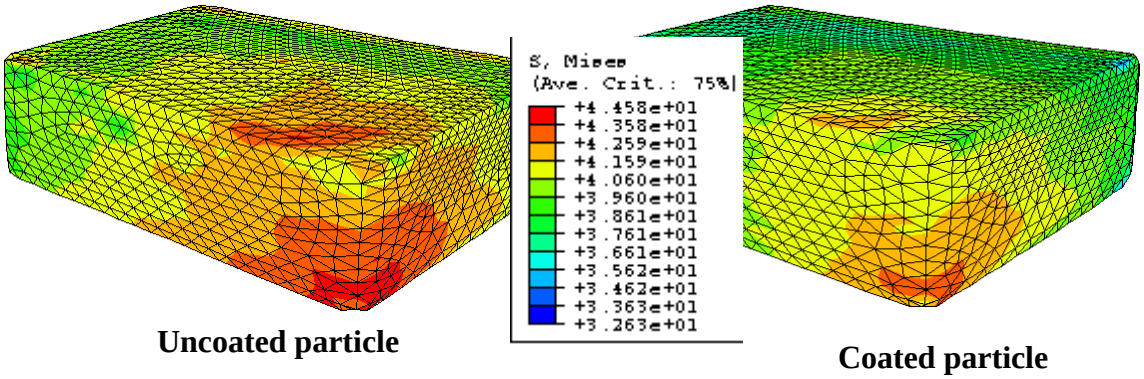

Figure 72. Comparison of Von Mises stress distribution in walnut region of coated and uncoated flat top particle at 100 N load

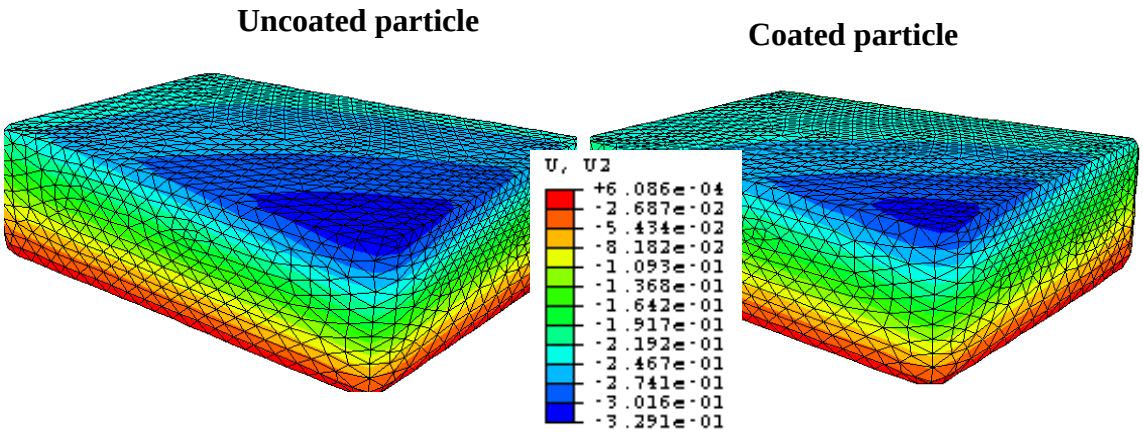

Figure 73. Comparison of displacement contour on the walnut region of coated and uncoated flat top particle at 100 N load

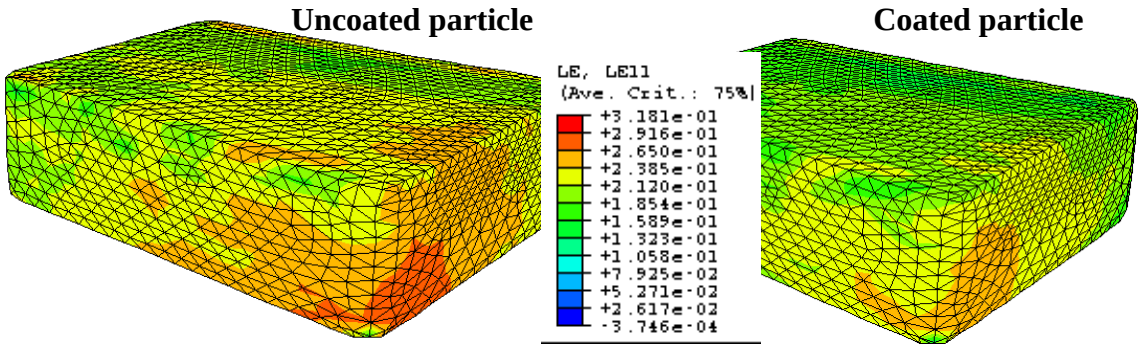

Figure 74. Comparison of true strain in (1-1) direction contour on the walnut region of coated and uncoated flat top particle at 100 N load

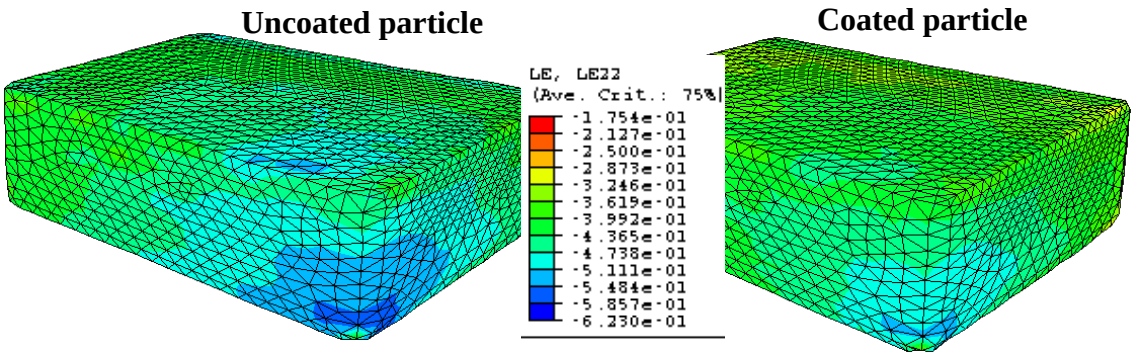

Figure 75. Comparison of true strain in (2-2) direction contour on the walnut region of coated and uncoated flat top particle at 100 N load

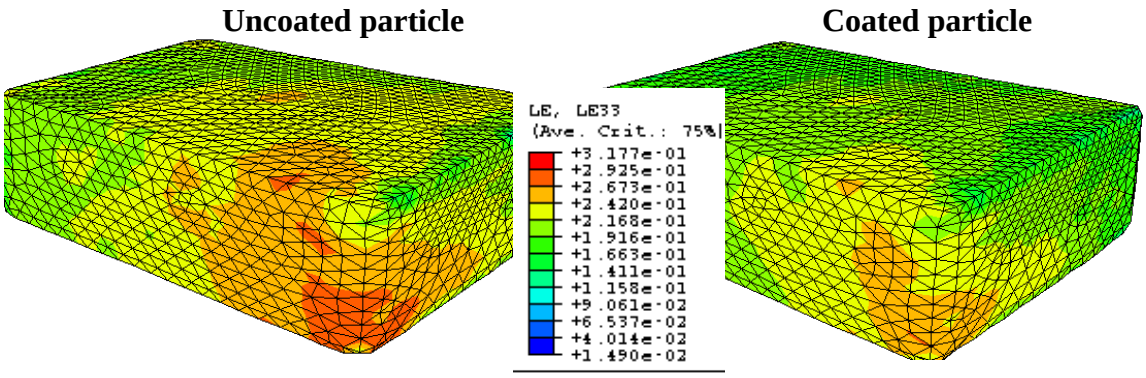

Figure 76. Comparison of true strain in (3-3) direction contour on the walnut region of coated and uncoated flat top particle at 100 N load

It is observed from the Figure 72 that the coated walnut shell particle is subjected to a lower value of Von Mises stress distribution at the same load when compared to the uncoated particle. In both cases, the particle is plastically deformed but the extent of plastic deformation is less in case of the coated particle. Even though the location of the maximum displacement is the same the coated particle as a whole experienced less displacement then the uncoated. The same observations are repeated for the strain in 1-1, 2-2 and 3-3 directions. The addition of coating ensures lesser strain distribution in the coated particle. At the applied load of 100 N the uncoated particle undergoes maximum strains and Von Mises stress over a larger area.

Similarly figures 77-81 show the contour plots showing the comparison of Von Mises stress, vertical displacement, LE11, LE22 and LE33 for the walnut region of the coated round top and the uncoated round top particles (CRT1 and RT1).

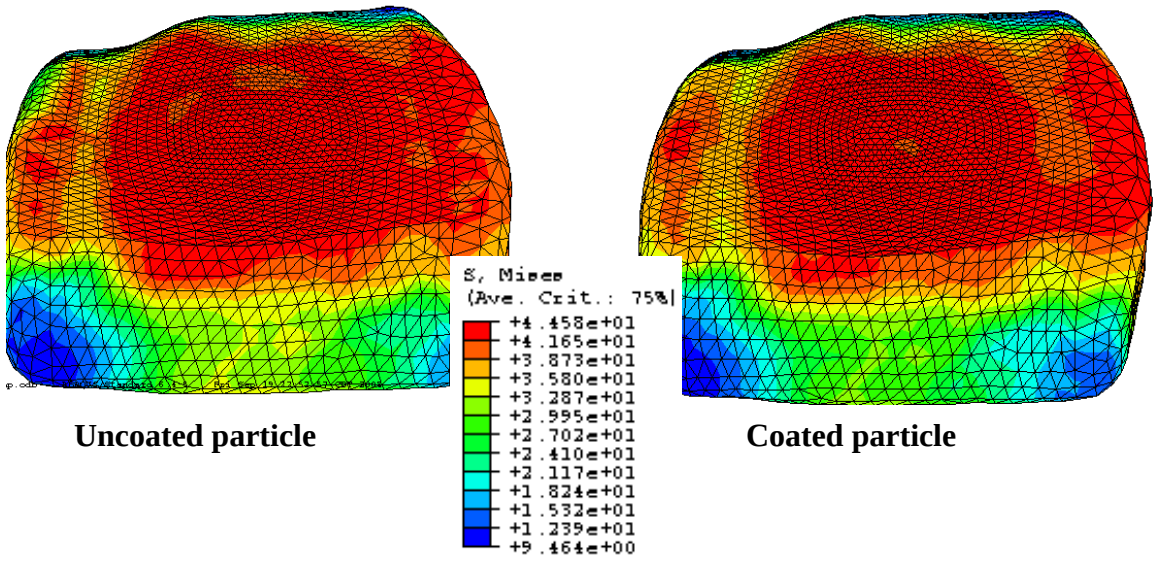

Figure 77. Comparison of Von Mises stress distribution in walnut region of coated and uncoated round top particle at 100 N load

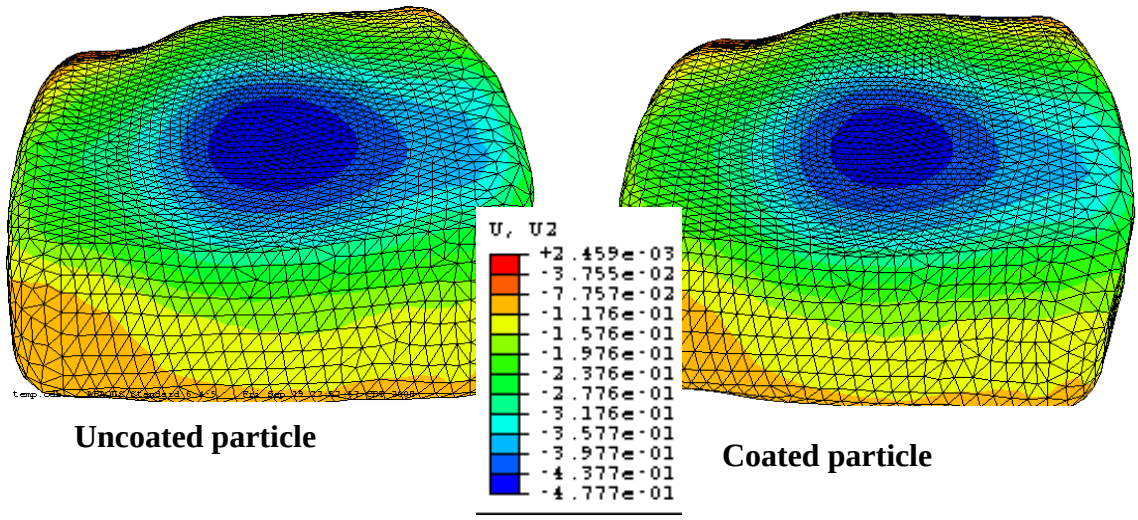

Figure 78. Comparison of displacement contour on the walnut region of coated and uncoated round top particle at 100 N load

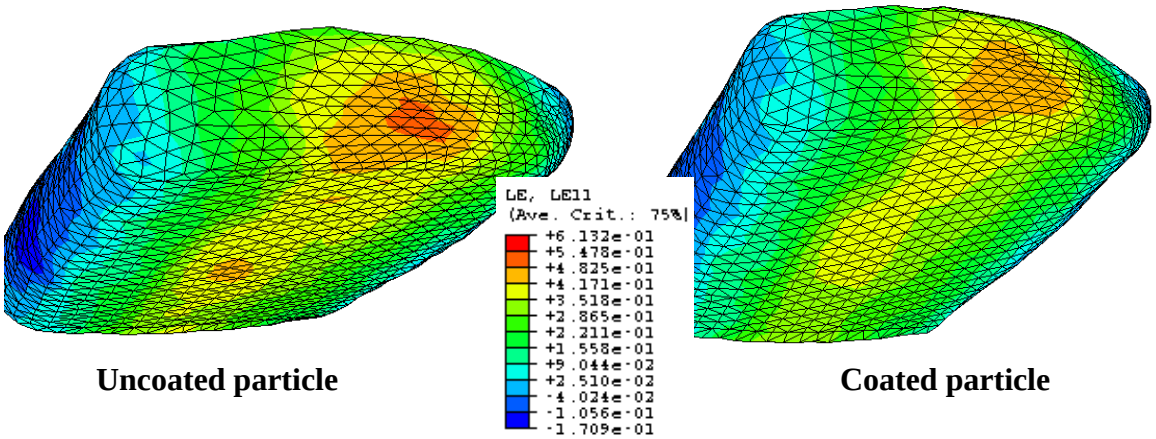

Figure 79. Comparison of true strain in (1-1) direction contour on the walnut region of coated and uncoated round top particle at 100 N load

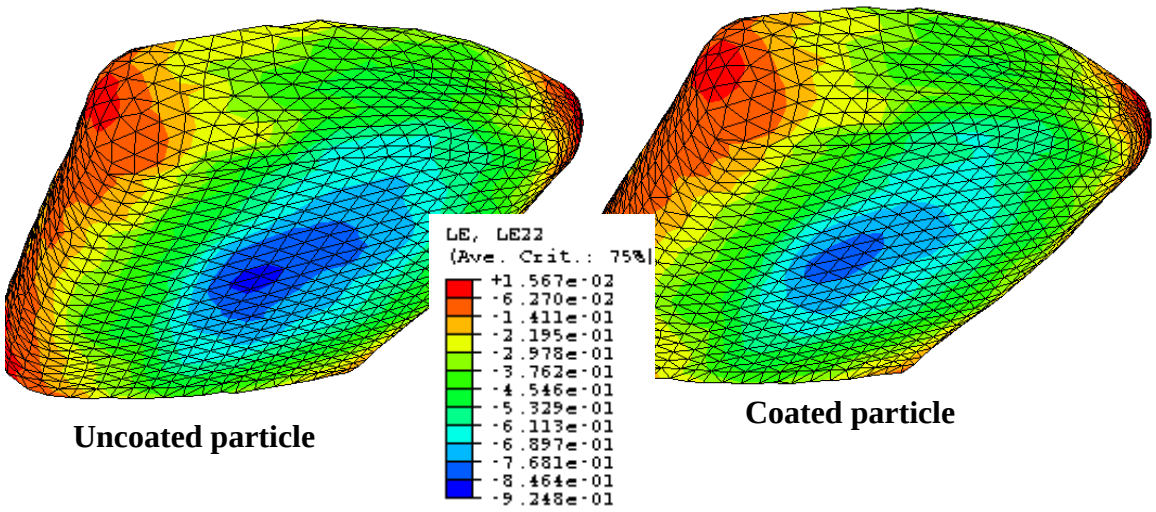

Figure 80. Comparison of true strain in (2-2) direction contour on the walnut region of coated and uncoated round top particle at 100 N load

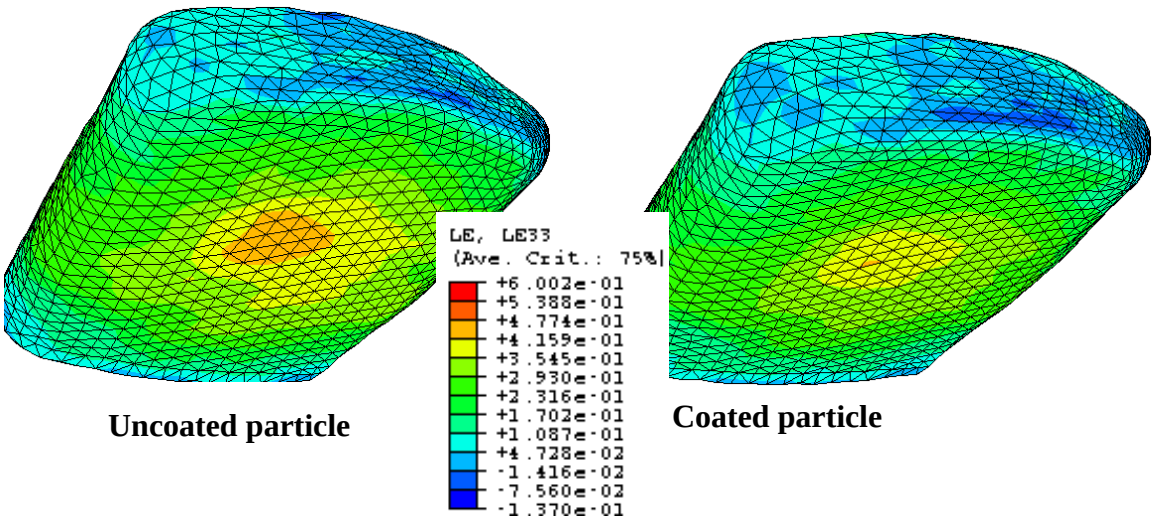

Figure 81. Comparison of true strain in (3-3) direction contour on the walnut region of coated and uncoated round top particle at 100 N load

Once again, it can be concluded that the spread of maximum stress in the uncoated particle is larger in comparison to the coated particle. Thus at the same load of 100 N, the coated particle is subjected to a lower overall stress and strain compared to the uncoated particle.

Similarly Figures 82-86 show the comparison of Von Mises stress, vertical displacement and LE22, LE11 and LE33 strain for the walnut region of the coated cone top and uncoated cone top models.

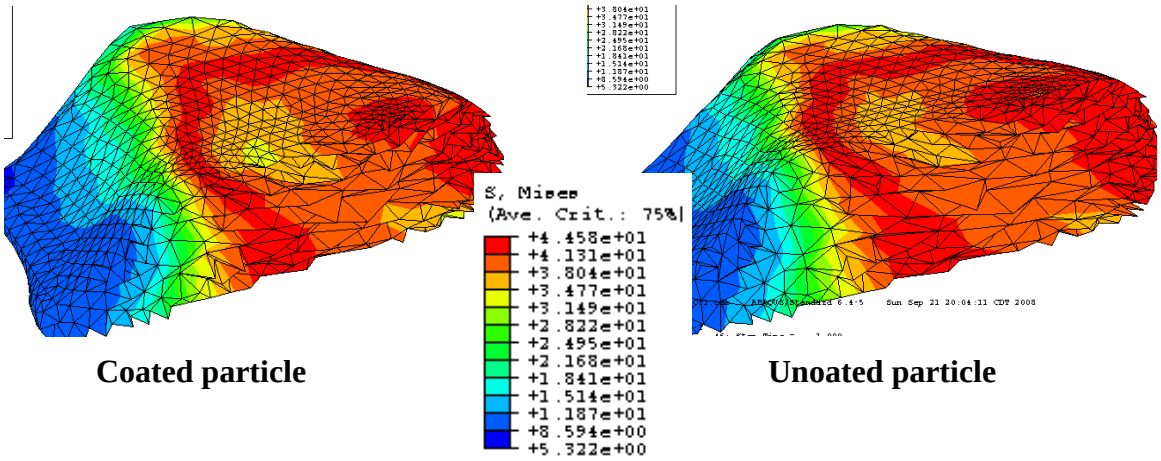

Figure 82. Comparison of Von Mises stress distribution in walnut region of coated and uncoated cone top particle at 100 N load

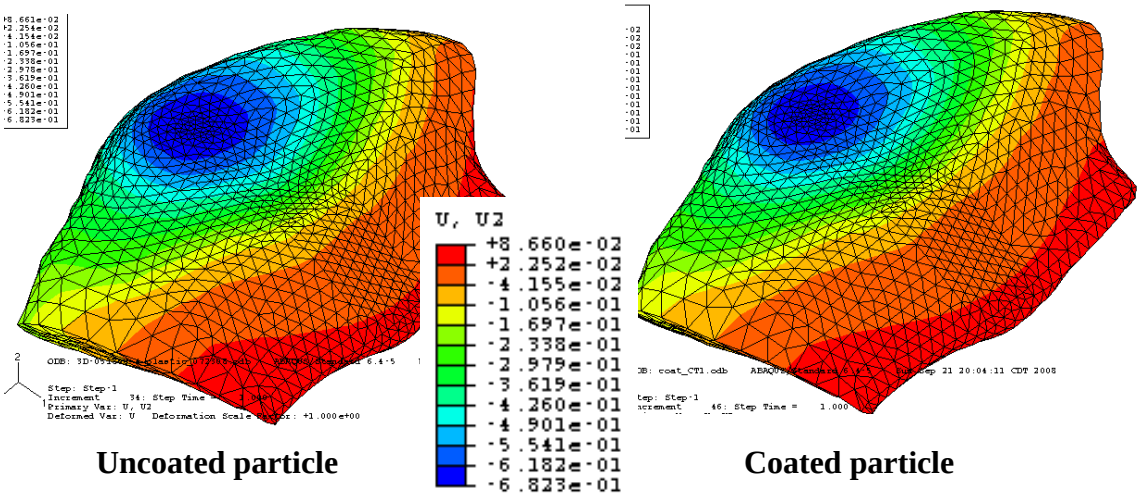

Figure 83. Comparison of displacement contour on the walnut region of coated and uncoated cone top particle at 100 N load

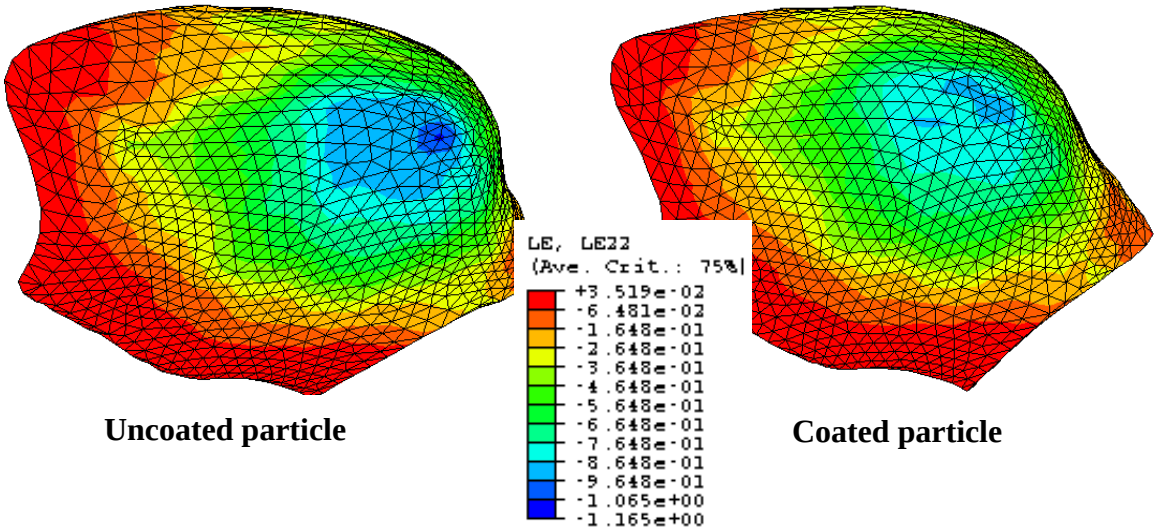

Figure 84. Comparison of true strain in (2-2) direction contour on the walnut region of coated and uncoated round top particle at 100 N load

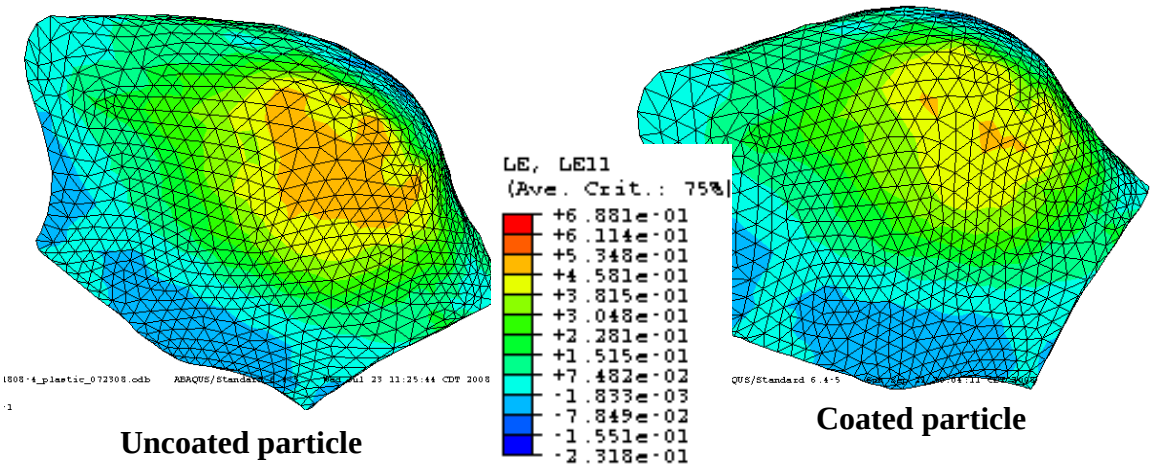

Figure 85. Comparison of true strain in (1-1) direction contour on the walnut region of coated and uncoated round top particle at 100 N load

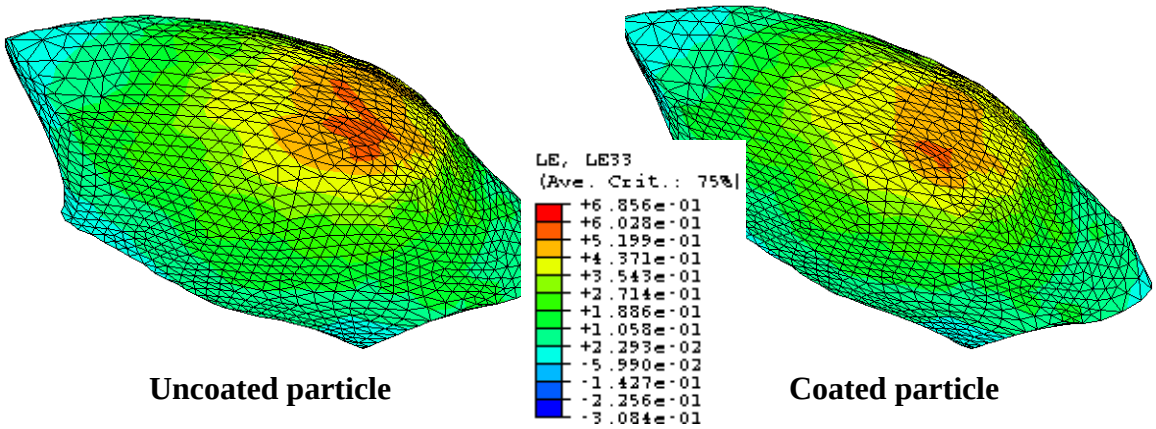

Figure 86. Comparison of true strain in (3-3) direction contour on the walnut region of coated and uncoated round top particle at 100 N load

In summary, although the polymer coat induces only a marginal improvement in the load vs displacement response of the walnut particle it improves its ability to carry the higher loads. However, the coating is assumed to be applied uniformly on the surface which is not the case in practice, the effects of non-uniform polymer coat needs to be studied. The correct polymer properties need to be determined and implemented into the model.

5 CONCLUSION AND FUTURE RESEARCH

5.1 Conclusion

Walnut shells offer realistic potential to be adopted as proppants. Polymer coated walnut shells have displayed significant improvement in resisting high closure stresses at the down-hole conditions in industrial laboratory tests. In this study, the focus was on evaluating the response of coated and uncoated ground walnut shell particles. Experimental and computational techniques have been employed to this end.

The study of the walnut shell cellular microstructure has been carried out to estimate its material properties based on its cellular structure as well as to detect the presence of polymer coat and further infiltration. The study of microstructure clearly identified that it varied along the shell thickness. The outermost layer of the walnut shell is covered with a layer of suberin which provides barrier properties. On the innermost layer the cell structure is porous and soft, while the rest of the shell is composed of sclereids with small lumina. The porosity in the particles based on ESEM and LM imaging is approximated to 10%. This value is corroborated by the calculation of relative density of the particles as 0.86 indicating 14% porosity. The chief constituents of the cell wall are cellulose, hemicellulose and lignin. Thickness of polymer coat on the coated particles is observed to range from 5 μm to 15 μm. Presence of polymer infiltration is not detected. A two layer composite particle has been assumed with the coat thickness ranging from ~ 5 μm to 15 μm and the core of walnut shell.

Three main testing procedures; single particle compression, heating tests on coated and uncoated walnut shell particles and 3-point flexure have been developed. Single particle compression test were conducted with random geometry particles. A large scatter in the data was observed. To reduce this statistical scatter, particles were divided into four distinct geometrical shape categories: flat top, round top, cone top, and high aspect ratio. The flat top particle gave the stiffest response while the cone top gave the least stiff response highlighting the significance of geometrical shape. Comparison

of the flat top uncoated and coated particle response indicated that coating induced a minor improvement in load vs displacement response. Cyclic compression loads were imposed on flat top particles which revealed a significant permanent deformation even at low load levels. Single particle tests on uniformly cut cuboid particles from walnut shell flakes were conducted to determine the nonlinear material properties of the walnut shells. The non-linear response is assumed to be elastic-plastic with isotropic hardening. Based on the compression tests plasticity is assumed to be triggered at a low stress of ~ 5 MPa. In-situ ESEM observations on both the coated and uncoated particles showed signs of charring at about 175 – 200 ºC. It was concluded that at the downhole temperature conditions the particle will be able to sustain the thermal loads. To comment on its ability to sustain compression loading at downhole temperatures would require development of coupled thermomechanical tests.

Computational models have been developed to simulate the single particle compression tests. The Hertz contact problem was solved as a problem of a contact between a sphere and a rigid plate. In this analysis the particles were idealized to be spherical. From the single particle tests it was realized that particles undergo large deformations and hence geometric nonlinearity was incorporated into the analysis. The influence of particle shape was studied by modeling 3D and 2D irregular shaped particles based on the actual images of test particles. These models simulated the compression of flat top, round top and cone top particles. The elastic material representation with nonlinear geometry was not able to simulate the compression response observed during testing. The inelastic material representation was able to bring about significant improvement in simulating the compression response. A single uniform layer of coating was introduced on the 3D models with inelastic material definition. Coating was observed to induce a marginal improvement in load vs displacement response of the particles while increasing its ability to withstand a larger load.

5.2 Future Research

In the current research the compression response of the walnut shell particles has been studied by assuming a homogenized material property of the walnut shell. Research can be carried out to simulate the influence of the microstructure, specifically the effect of cell shape and the effect of relatively weak bonding between two cells on the particle response. While simulating the nonlinear uncoated particles the damage initiation in the particles has not been considered which can be incorporated.

A comparative study of a number of nutshells like walnut, pistachio, pecan etc can be carried out to determine the most suitability of these nutshells to be used for hydraulic fracturing applications as proppants. Combining the experimental and computational analysis techniques a screening methodology can be developed to analyze the suitability of a given proppant material and coating. Such a screening technique can provide a virtual parametric test capability by simulating the single particle compression, multiple particle interaction and particle flow capability. This screening technique can be developed as an alternative for the current industrial practice of carrying out long term conductivity tests on a newly developed proppant material.

REFERENCES

1. Waveland Group. Propfrac. http://www.wavelandgroup.com/popfrac.htm. Accessed August 2008.

2. Mader, D. (1989). *Hydraulic Proppant Fracturing and Gravel Packing*. Elsevier Science Publishing Company Inc., New York.

3. Rickards, A.R., Brannon, H.D., Wood, W.D. and Stephenson, C.J. (2006). High Strength Ultra Lightweight Proppant Lends New Dimensions to Hydraulic Fracturing Applications, *SPE Production & Operations*, **21**(2):212-221.

4. READE.COM. Walnut Shell Media. http://www.reade.com/index.php?option=com_content&task=view&id=816&Itemid=10 . Accessed July 2007.

5. Kim, J.W., Sohn, M.H., Kim, D.S., Sohn, S.M. and Kwon, Y.S. (2001). Production of Granular Activated Carbon from Waste Walnut Shell and its Adsorption Characteristics for Cu^{2+} Ion, *Journal of Hazardous Materials,* **85**(3):301-315.

6. Shaoping, X., Shucai, G., Shan, J. and Tau, W. (1996). Carbon Molecular Sieves From Walnut Shell, *Fuel Science & Technology International*, **14**(10):1447-1459.

7. Sinclair, A.R. (1991). New Resin Coated Proppants, In: *proc. of the Annual South Western Petroleum short Course*, thirty eighth annual meeting. 85-97.

8. Swanson, S.R. and Cutler, R.A. (1983). Fracture Analysis of Ceramic Proppants, *Journal of Energy Resources Technology*, **105**(2):128-133.

9. Darin, S.R. and Huitt, J.L. (1960). Effect of a Partial Monolayer of Propping Agent on Fracture Flow Capacity, T*ransactions of the American Institute of Mining and Metallurgical Engineers,* **219**(3): 31-37.

10. Veatch Jr., R.W. (1993). Overview of Current Hydraulic Featuring Design and Treatment Technology – Part 2, In: *Distinguished Author Series of the Society of Petroleum Engineers of AIME.*

11. Brannon, H.D. (2004). Maximizing Fracture Conductivity with Proppant Partial Monolayers: Theoretical Curiosity or Highly Productive Reality, In: *Proc. of Society of Petroleum Engineers (U.S.), Technical Conference and Exhibition,* Houston, TX, pp. 3569-3591.

12. Gibson, L.J. and Ashby, M.F. (1997). *Cellular Solids: Structure and Properties*, 2nd Edition, Cambridge University Press, New York.

13. Demirbas, A. (2005). Estimating of Structural Composition of Wood and Non-Wood Biomass Samples, *Energy Sources*, **27**:761-767.

14. Bodig, J. and Jayne, B.A. (1982). *Mechanics of Wood and Wood Composites*, Van Nostrand Reinhold Company Inc., New York.

15. Bergander, A. and Salmen, L. (2002). Cell Wall Properties and Their Effects on the Mechanical Properties of Fibers, *Journal of Materials Science*, **37**:151-156.

16. Huang, C.L., Lindstrom, H., Nakada, R. and Ralston, J. (2003). Cell Wall Structure and Wood Properties Determined by Acoustics – A Selective Review, *Holz als Roh- und Werkstoff,* **61**: 321-335.

17. Gindl, W., Gupta, H.S., Schoberl, T., Lichtenegger, H.C. and Fratzl, P. (2004). Mechanical Properties of Spruce Wood Cell Walls by Nanoindentation, *Applied Physics A, Materials Science & Processing,* **79**:2069-2073.

18. Wang, C.H. (1996). Structures and Properties of Nutshells, In: *Proc. of the first Australasian Congress on Applied Mechanics; ACAM-96,* Melbourne, Australia, 21-23 February, pp. 443-448.

19. Wang, C.H. and Mai, Y.W. (1994). Deformation and Fracture of Macadamia Nuts, Part 2: Microstructure and Fracture Mechanics Analysis of Nutshell, *International Journal of Fracture,* **69**: 67-85.

20. Kulkarni, R., Brewer, J., Ochoa, O.O. and Harris, M. (2003). Anisotropy in Hickory Shells: Reinforcement Architecture and Material Properties, In: *Proc. of 18th Annual Technical Conference of the American Society of Composites,* Gainesville, FL, October.

21. Katherine, E. (1965). *Plant Anatomy*. John Wiley & Sons Inc., New York.

22. Universitat Hamburg. Department Biologie. http://www.biologie.uni-hamburg.de/b-online/library/webb/BOT410/410Labs/LabsHTML-99/SimpleTissues/simptisx99rev.html. Accessed May 2008.

23. Beekman, W.J., Meesters, G.M.H., Becker, T., Gaertner, A., Gebert, M. and Scarlett, B. (2003). Failure Mechanism Determination for Industrial Granules Using a Repeated Compression Test, *Powder Technology,* **130**: 367-376.

24. Cheong, Y.S., Adams, M.J., Hounslow, M.J. and Salman, A.D. (2005). Mechanical Behaviour of Dry Binderless Polystyrene Granules, *Chemical Engineering Research & Design,* **83**(A11): 1276-1282.

25. Johnson, K.L. (1985). *Contact Mechanics,* Cambridge University Press, Cambridge, UK.

26. Antonyuk, S., Tomas, J., Heinrich, S. and Morl, L. (2005). Breakage Behaviour of Spherical Granulates by Compression, *Chemical Engineering Science*, **60**: 4031-4044.

27. Spatz, H.-CH., Kohler, L. and Niklas, K.J. (1999). Mechanical Behaviour of Plant Tissues: Composite Materials or Structures?, *The Journal of Experimental Biology*, **202**: 3269-3272.

28. Kohler, L. and Spatz, H.-CH. (2002). Micromechanics of Plant Tissues Beyond the Linear-elastic Range, *Planta*, **215**: 33-40.

29. AZoM.com. Particle Size – US Sieve Series and Tyler Mesh Size Equivalents. http://www.azom.com/details.asp?ArticleID=1417. Accessed August 2008.

30. Brannon, H.D., Stephenson, C.J. and Maharidge, R., Feb 2008, Personal Communication, BJ Services Inc., Tomball, TX.

31. GIMP – GNU Image Manipulation Program. http://www.gimp.org. Accessed July 2007.

32. Brannon, H.D., Stephenson, C.J. and Maharidge, R., Nov 2007, Personal Communication, BJ Services Inc., Tomball, TX.

33. Scrivener, K.L. (2004). Backscattered Electron Imaging of Cementitious Microstructures: Understanding and Quantification, *Cement & Concrete Composites*, **26**: 935-945.

34. Standard Test Method for Compressive Properties of Rigid Plastics. *Annual Book of ASTM Standards*. Volume 08.02. ASTM D 695 – 02a.

35. ABAQUS, User's Manual, Version, 6.5. (2005). Hibbitt, Karlsson and Sorensen Inc.

36. Boer den, J.J. (1999). The Use of High Temperature Electronics in Downhole Applications, In: *Proc. of the HITEN Conference,* Berlin, Germany, 4-7 July, 149-152.

37. Yuan, H.R. and Liu, R.H. (2007). Study of Pyrolysis Kinetics of Walnut Shell, *Journal of Thermal Analysis and Calorimetry*, **89**(3): 983-986.

38. Standard Test Method for Flexural Properties of Unreinforced and Reinforced Plastics and Electrical Insulating Materials. *Annual Book of ASTM Standards*. Volume 08.01. ASTM D 790 – 02.

39. Timoshenko, S.P. and Goodier, J.N. (1970). *Theory of Elasticity*, 3rd Edition, McGraw-Hill, New York.

40. Kogut, L. and Etsion, I. (2002). Elastic-Plastic Contact Analysis of a Sphere and a Rigud Flat, *Journal of Applied Mechanics*, **69**: 657-662.

41. Vu-Quoc, L., Zhang, X. and Lesburg, L. (2000). A normal Force-Displacement Model for Contacting Spheres Accounting for Plastic Deformation: Force-Driven Formulation, *Journal of Applied Mechanics*, **67**: 363-371.

42. Dennis Dawson Co., Walnut Soft Abrasive Grit. http://www.dennisdawson.com/walnut.htm. Accessed February 2007.

43. Sadd, M.H. (2005). *Elasticity: Theory, Applications and Numerics*, Elsevier Butterworth Heinemann, Amsterdam.

44. Brannon, H.D., Stephenson, C.J. and Maharidge, R., Aug 2007, Personal Communication, BJ Services Inc., Tomball, TX.

45. Plenco Plastics Engineering Company, Data Reports. http://www.plenco.com/data/data.htm. Accessed October 2007.

46. Callister, W.D. (2000). *Material Science and Engineering: An Introduction*, 5th Edition, John Wiley & Sons, Inc, New York.

47. Niklas, K.J. (1992). *Plant Biomechanics: An Engineering Approach to Plant Form and Function*, University of Chicago Press, Chicago.

48. Choi, M.H. and Chung, I.J. (2003). Mechanical and Thermal Properties of Phenolic Resin-Layered Silicate Nanocomposites Synthesized by Melt Intercalation, *Journal of Applied Polymer Science*, **90**: 2316-2321.

49. University of Cambridge., DoITPoMS Teaching and Learning Packages. http://www.msm.cam.ac.uk/doitpoms/tlplib/deformation/derivation_youngs_modulus.php. Accessed October 2008.

50. Christensen, R. M. (1990). A Critical Evaluation for a Class of Micro-mechanics Models, *J. Mech. Phys. Solids*, **38**(3): 379-404.

APPENDIX A

Gibson and Ashby [12] have treated the wood cellular structure as equivalent to a honeycomb structure which is an array of two dimensional hexagonal cells. The wood elastic properties in the transverse direction are taken to be equivalent to the in plane elastic properties of a honeycomb. The schematic of a hexagonal cell is shown in Figure 87. The axial elastic properties of wood are equivalent to the out of plane elastic properties of a honeycomb. The derivation of the in plane and out of plane elastic modulus of a honeycomb is discussed below.

Transverse (In Plane) Elastic Modulus:

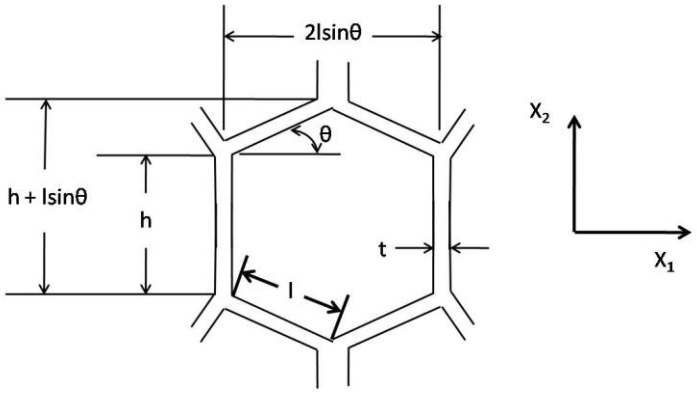

Figure 87. Schematic of an undeformed honeycomb cell

The thickness of each cell wall is t. The ratio of the honeycomb cell wall thickness to the cell ligament length (t/l) is assumed to be small. With transverse loading (X_1 or X_2 direction) the deformation takes place due to bending of the cell wall at angle θ to X_1 direction. As an example a stress σ_1 in X_1 direction (Figure 88) causes

the wall of length - l (ones which are at an angle θ to the loading direction) to bend. The displacements of the two halves of the diagonal wall are in opposite directions and symmetric about the centre. Each half is then assumed to be a cantilever beam of length l/2. The beams are fixed at the vertical faces and loaded at the centre with the load Psinθ [49]. The resulting bending moment M is calculated as below. Here the cell wall is treated as a beam with thickness t, depth b with Young's modulus as $E_{wall.}$ P is the load acting due to the stress σ_1 in X_1 direction. The stress acts on the projected area (h + lsinθ)b, which is the projected area consisting of the two halves of the vertical ligaments (each of height h/2) connected to the ligament at angle θ and the vertical projection of the ligament of length l at angle θ to X_1 (lsinθ). The depth of the section is b in the X_3 direction. A schematic showing the loading on the ligament due to the stress σ_1 is shown in Figure 88. The system consists of three ligaments the two halves of vertical ligaments each of length h/2 and the ligament of length l at angle θ to X_1. The honeycomb is formed by repeating arrangement of these three ligaments. A single honeycomb cell is formed by symmetrical positioning of these three ligaments. Figure (a) shows the load P acting on the ligament and the resulting moments. Figure (b) shows the deformed configuration of the ligament due the load P.

$$M = \frac{Pl\sin\theta}{2}$$

$$P = \sigma_1\left(h + l\sin\theta\right)b$$

Based on the standard beam bending theory the wall deflection is given as

$$\delta = \frac{Pl^3\sin\theta}{12\ E_{wall}I}$$

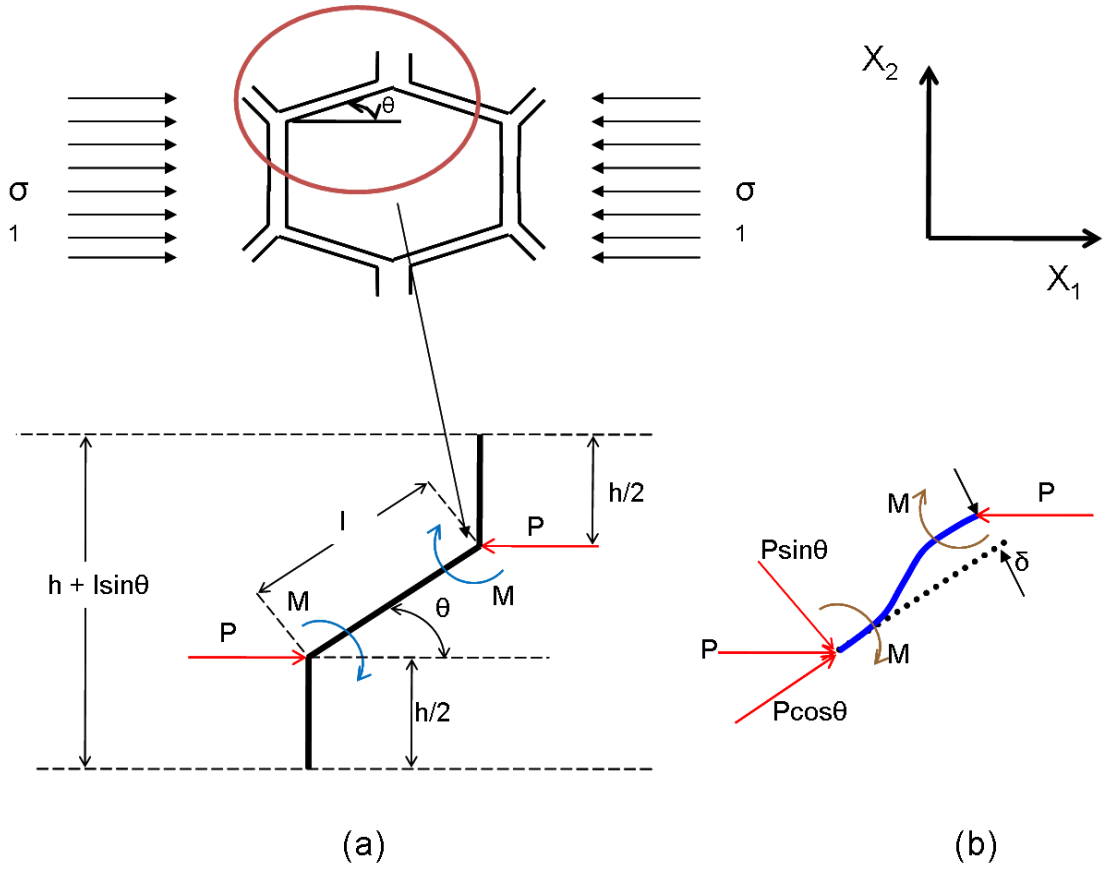

Figure 88. Loads acting on ligament of length l which is at an angle θ to X_1 direction

Here I is the second moment of inertia of the cell wall ($I = bt^3/12$) for a wall of thickness t and depth d. A component δsinθ is parallel to X_1, leads to a strain of

$$\varepsilon_1 = \frac{\delta \sin\theta}{l\cos\theta} = \frac{\sigma_1 (h + l\sin\theta) b l^2 \sin^2\theta}{12 E_{wall} I \cos\theta}$$

The elastic modulus parallel to X_1 is $E_{transverse} = \sigma_1/\varepsilon_1$. This is the transverse elastic modulus of the honeycomb.

$$\frac{E_{transverse}}{E_{wall}} = \left(\frac{t}{l}\right)^3 \frac{\cos\theta}{(h/l + \sin\theta)\sin^2\theta},$$

Now according to [12] the relation between density ratio of a cellular solid material and the cell wall is specified as

$$\frac{\rho_{material}}{\rho_{wall}} = C_1 \frac{t}{l}$$

Replacing the thickness to length ratio with the density ratio we get the expression relating the in-plane elastic modulus of the honeycomb to the density ratio. The constant is dependent on the details of cell shape. This relation for wood is depicted below.

$$E_{transverse} = 0.54 E_{wall} \left(\frac{\rho_{material}}{\rho_{wall}} \right)^3$$

Axial Elastic Modulus (Out of Plane):

The elastic modulus in the direction X_3 (out of plane represented by $X_1 - X_2$) represents the modulus of the section scaled with the area of the section which bears the load (Area of the ligaments on the section). This is essentially based on rule of mixtures. If E_{axial}, E_{wall} and E_{pore} represent the out of plane elastic modulus of the honeycomb, cell wall and porosity respectively and A_{axial}, A_{wall} and A_{pore} represent the areas of the honeycomb section, ligaments and pore space respectively then according to rule of mixtures.

$$E_{axial} A_{axial} = E_{wall} A_{wall} + E_{pore} A_{pore}$$

Now the porosity does not contribute towards the axial elastic stiffness. Thus the above expression is reduced to

$$E_{axial} A_{axial} = E_{wall} A_{wall}$$

Thus the axial elastic modulus is represented as below, based on the geometry of the cross section. This expression gives the expression for the axial elastic modulus of wood presented in section 2.2.

$$\frac{E_{axial}}{E_{wall}} = \left\{ \frac{h/l + 2}{2\left(h/l + \sin\theta\right)\cos\theta} \right\} \frac{t}{l} = \frac{\rho_{material}}{\rho_{wall}} \approx \frac{t}{l}$$

$$E_{axial} = E_{wall} \left(\frac{\rho_{material}}{\rho_{wall}} \right)$$

APPENDIX B

The three phase solution has been developed by Christensen [50]. In this model we consider an equivalent homogeneous media as in Figure 89. We also consider that the infinite region is subjected to homogenous deformation conditions at large distances from the origin. The outer layer of the material (infinite medium) has its properties as the unknown effective properties of μ (shear modulus) and k (bulk modulus). The above configuration is considered equivalent to a completely homogeneous material by requiring that both the phases store the same strain energy, under conditions of identical average strain.

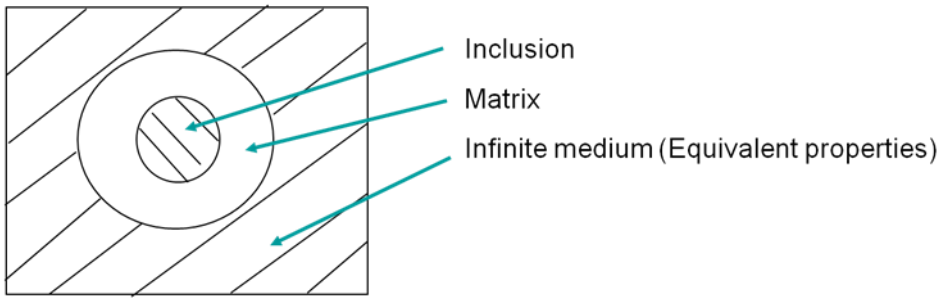

Figure 89. 3-Phase model

The proper solution of this three phase problem along with proper averaging techniques yields the complete solution for the effective properties of μ and k of the composite medium of an isotropic matrix phase into which is embedded the isotropic inclusion phase.

The following is the solution for determining the effective shear and bulk modulus for composite with spherical inclusions. The solution of the quadratic equation presented below gives us the effective shear modulus.

$$A(\mu/\mu_m)^2 + 2B(\mu/\mu_m) + C = 0 \quad (16)$$

Where,

$$A = 8((\mu_i/\mu_m) - 1)(4 - 5\nu_m)\eta 1c^{10/3} - 2[63((\mu_i/\mu_m) - 1)\eta 2 + 2(\eta 1)(\eta 3)]c^{7/3}$$
$$+ 252((\mu_i/\mu_m) - 1)\eta 2\, c^{5/3} - 50((\mu_i/\mu_m) - 1)(7 - 12\nu_m + 8\nu_m^2)\eta 2c$$
$$+ 4(7 - 10\nu_m)(\eta 2)(\eta 3)$$

$$B = -2((\mu_i/\mu_m) - 1)(1 - 5\nu_m)\eta 1c^{10/3} + 2[63((\mu_i/\mu_m) - 1)\eta 2 + 2(\eta 1)(\eta 3)]c^{7/3}$$
$$- 252((\mu_i/\mu_m) - 1)\eta 2\, c^{5/3} + 75((\mu_i/\mu_m) - 1)(3 - \nu_m)\eta 2c\nu_m$$
$$+ (3/2)(15\nu_m - 7)(\eta 2)(\eta 3)$$

$$C = 4((\mu_i/\mu_m) - 1)(5\nu_m - 7)\eta 1c^{10/3} - 2[63((\mu_i/\mu_m) - 1)\eta 2 + 2(\eta 1)(\eta 3)]c^{7/3}$$
$$+ 252((\mu_i/\mu_m) - 1)\eta 2\, c^{5/3} + 25((\mu_i/\mu_m) - 1)(\nu_m^2 - 7)\eta 2c$$
$$- 4(7 + 5\nu_m)(\eta 2)(\eta 3)$$

$$\eta 1 = ((\mu i/\mu m) - 1)(7 - 10\nu m)(7 + 5\nu i) + 105(\nu i - \nu m)$$
$$\eta 2 = ((\mu i/\mu m) - 1)(7 + 5\nu i) + 35(1 - \nu i)$$
$$\eta 3 = ((\mu i/\mu m) - 1)(8 - 10\nu m) + 15(1 - \nu m)$$

The effective bulk modulus is calculated using the following equation.

$$k = km + \frac{c(ki - km)}{1 + (1 - c)\dfrac{(ki - km)}{(km + (4/3)\mu m)}} \tag{17}$$

Where,

μ	Effective shear modulus
μ_m	Shear modulus of the matrix material
μ_i	Shear modulus of the Inclusion material
νm	Poisson's ratio of the matrix material
ν_i	Poisson's ratio of the inclusion material
k	Effective bulk modulus
k_m	Bulk modulus of matrix material
k_i	Bulk modulus of inclusion material

APPENDIX C

Non-linear geometry condition is related to the change in the stiffness response of a model following its deformation in an analysis. This occurs when magnitudes of displacement are large enough to affect the structural response. The three main causes of Geometric nonlinearity as discussed in the ABAQUS/ Standard User's Manual [35] are:

- Large deflections or rotations.
- Snap through.
- Initial stresses or load stiffening.

An example of Geometric nonlinearity is that of a fishing rod undergoing large deflections, buckling of a column or the snap through of a large panel. In general as per ABAQUS/ Standar User's Manual [35] whenever the strains exceed a value of ~ 5% non-linear geometry needs to be incorporated into the analysis. The Figure 90 below shows an example of effect of large deflection on a cantilever beam.

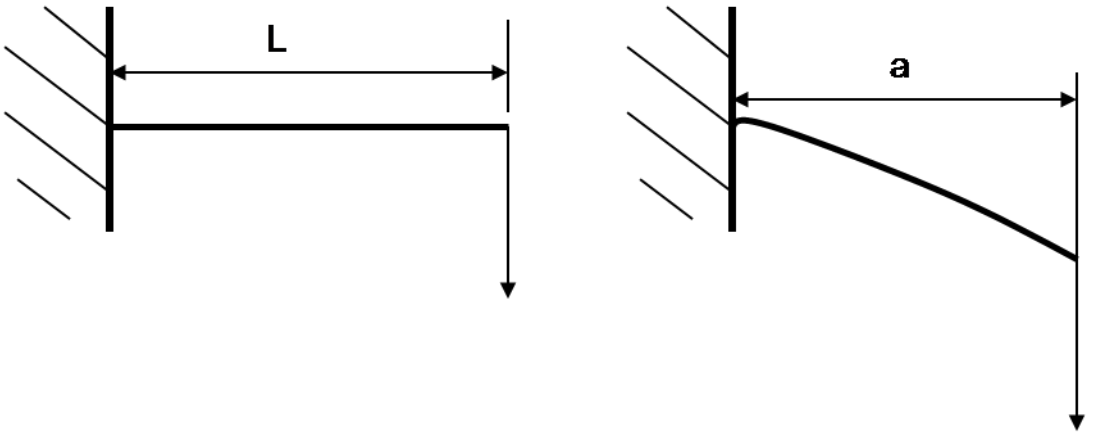

Figure 90. Large deflection in a cantilever beam

In this case the tip of the cantilever beam undergoes a considerable axial deflection in addition to its transverse deflection. Thus the effective moment arm of the force is reduced (a < L) and hence the beam tends to give a stiffer response to additional deflection. This non-linear response because of change in model geometry under loading is an example of Geometric nonlinearity.

Geometric nonlinearity can be incorporated in an ABAQUS analysis by including the NLGEOM parameter with the *STEP option. This option takes into account the higher-order terms in the strain-displacement relations shown below. With this option incorporated the loading is incremental and the element stiffness matrix is updated at all the iterations. All the elements in ABAQUS have the ability to use a non-linear formulation. The element output is true stress and logarithmic strain.

$$\varepsilon_X = \frac{\partial u_X}{\partial X} + \frac{1}{2}\left[\left(\frac{\partial u_X}{\partial X}\right)^2 + \left(\frac{\partial u_Y}{\partial Y}\right)^2 + \left(\frac{\partial u_Z}{\partial Z}\right)^2\right] \tag{18}$$

$$\varepsilon_Y = \frac{\partial u_Y}{\partial Y} + \frac{1}{2}\left[\left(\frac{\partial u_X}{\partial X}\right)^2 + \left(\frac{\partial u_Y}{\partial Y}\right)^2 + \left(\frac{\partial u_Z}{\partial Z}\right)^2\right] \tag{19}$$

$$2\varepsilon_{XY} = \frac{\partial u_X}{\partial X} + \frac{\partial u_Y}{\partial Y} + \left[\frac{\partial u_X}{\partial X}\frac{\partial u_X}{\partial Y} + \frac{\partial u_Y}{\partial X}\frac{\partial u_Y}{\partial Y} + \frac{\partial u_Z}{\partial X}\frac{\partial u_Z}{\partial Y}\right] \tag{20}$$

APPENDIX D

Material nonlinearity arises when the stress/ strain response follows a non-linear curve. In this case the stress response is dependent on strain and does not follow a linear relationship. Nonlinear material properties can be both elastic and plastic. As discussed in ABAQUS/ Standar User's Manual [35] the non-linear elastic properties include hyperelasticity, viscoelasticity, hypoelasticity etc. The inelastic properties include classical metal plasticity, rate dependent yield, anisotropic yield and creep, porous metal plasticity, cast iron plasticity, extended Drucker-Prager plasticity and creep, clay plasticity, crushable foam plasticity, concrete etc.

The classical metal plasticity is used to describe the yield and inelastic flow of metals at low temperatures where the creep effects are not important and loading is monotonic. The Mises or Hill yield surfaces associated with plastic flow are used in ABAQUS. Two definitions for work hardening are available, perfect plasticity and isotropic hardening both of these are described in Figure 91 (a and b).

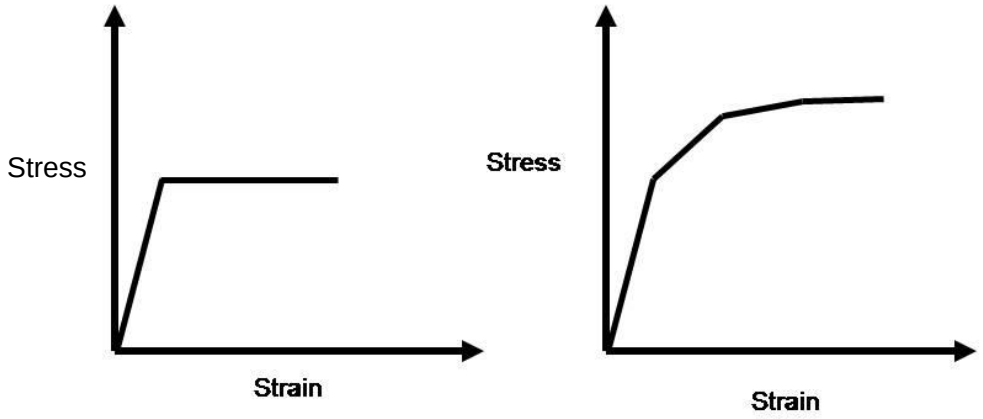

(a) Elastic Perfectly Plastic (b) Elastic Plastic Hardening

Figure 91. Stress strain relationship for elastic perfectly plastic and plastic with hardening

Perfect plasticity implies that the yield stress is invariant with strain. With isotropic hardening the size of the yield surface changes uniformly in all directions, hence the yield stress increases or decreases in all directions uniformly as plastic straining takes place. Isotropic yielding is defined using the Mises yield surface. Classical metal plasticity can be incorporated in ABAQUS using the *PLASTIC card with the *MATERIAL option. The data for hardening behavior is incorporated as a true stress, and plastic strain data in a tabular format or by defining the yield stress in a user subroutine UHARD.

ABAQUS interpolates linearly between the input data points to obtain the material response and assumes that beyond the final data point the response is constant. Thus with an elastic perfectly plastic definition, stress in any element cannot exceed the yield stress and straining at a constant stress value takes place beyond this point. PEEQ (equivalent plastic strain) which is a scalar variable is used to represent a material's inelastic deformation. A PEEQ value greater than zero indicates material has yielded. PEEQ is defined by the following equation [35].

$$\bar{\varepsilon}^{pl} = \bar{\varepsilon}^{pl}\Big|_0 + \int_0^t \sqrt{\frac{2}{3}\dot{\varepsilon}^{pl} : \dot{\varepsilon}^{pl}}\, dt \tag{21}$$

Here $\bar{\varepsilon}^{pl}\Big|_0$ is the initial equivalent plastic strain defined by the *INITIAL CONDITIONS option.

VITA

Name: Mandar Chaitanya Kulkarni

Address: Department of Mechanical Engineering, 3123 TAMU, College Station, TX 77843, USA

Email Address: mandar.kulkarni@tamu.edu

Education: B.E, Mechanical Engineering, Sardar Patel University, India, 2004

M.S, Mechanical Engineering, Texas A&M University, College Station, Texas, 2008